

An Abstract of the Thesis of

Yue-shu Xu for the degree of Doctor of Philosophy in Physics presented on May 8, 1992.

Title: A Study of the Decay $^{184}\text{Au} \rightarrow ^{184}\text{Pt}$ by Means of Gamma and Electron Spectroscopy and Low Temperature Nuclear Orientation

Redacted for Privacy

Abstract approved: _____

Kenneth S. Krane

The decay of ^{184}Au to ^{184}Pt has been studied with mass separated sources from the UNISOR facility. Multiscaled spectra of γ rays, x rays and conversion electrons were obtained along with γ - γ -t, and e^- - γ -t coincidence data. The decay scheme of ^{184}Au to ^{184}Pt has been updated. In total about 180 γ transitions have been assigned and 52 levels have been established in ^{184}Pt . Low-energy coexisting bands are identified based on the E0 transitions between states of the same spin in the two coexisting bands. A unique feature of the ^{184}Pt level scheme is the second set of coexisting bands, built respectively on the 2^+ states at 649 keV and 1173 keV. They are identified as the γ -vibrational bands of the two coexisting rotational bands. The conversion coefficients of $\Delta I = 0$ transitions between states of coexisting bands are deduced. In combination with nuclear orientation data, relative E0 strengths are calculated. Results are interpreted in comparison with the theoretical calculation, which predicts that the mixing of coexisting bands gives rise to enhanced E0 transition.

**A Study of the Decay $^{184}\text{Au} \rightarrow ^{184}\text{Pt}$ by Means of Gamma
and Electron Spectroscopy and Low Temperature Nuclear Orientation**

by
Yue-shu Xu

A THESIS
submitted to
Oregon State University

in partial fulfillment of
the requirements for the
degree of

Doctor of Philosophy

Completed May 8, 1992
Commencement June 1992

Approved:

Redacted for Privacy

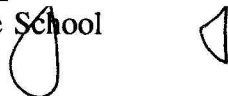
Professor of Physics in charge of major

Redacted for Privacy

Chairman of the Department of Physics

Redacted for Privacy

Dean of Graduate School



Date thesis is presented _____ May 8, 1992

Typed for Yue-shu Xu by _____ Yue-shu Xu

Acknowledgements

I am deeply indebted to many people for their assistance in the completion of this thesis, and would like to take this opportunity to express my gratitude.

First I would like to thank my thesis advisor, Dr. Kenneth S. Krane for his continuing support, guidance and encouragement throughout this project. His great interest in and intuitive approach to physics has been appreciated. The association and friendship developed with him during this many years will be deeply cherished. I would also like to extend my sincere appreciation of the close collaboration with the Georgia Tech group headed by Dr. John L. Wood and the Louisiana State University group headed by Dr. Edward. F. Zganjar. Dr. Wood's tremendous contribution in the spectroscopy data analysis and his invaluable advice in tackling complex problems are especially acknowledged.

I wish to thank Dr. H. Kennon Carter for his direction of UNISOR and his involvement in this project. His help and friendship made our stay in Oak Ridge more enjoyable. I am grateful to M. Jarrio, B. Zimmerman, D. Rupnik, T. Lam, C. Girit, P. Mantica, Jr., J. Kormicki and J. Breitenbach, who have shared with me so many night shifts and made my working at HHIRF facility a very memorable experience.

I would like to express my sincere thanks to Dr. Mark A. Gummin for the endless hours of working together, for his friendship and for the many discussions ranging from the tao of physics to the philosophy of life. The many frustrations associated with the graduate life have been greatly lightened by his companionship and unfailing help.

The financial assistance from the Department of Physics at OSU and U. S. DOE is greatly appreciated. I also thank the advisors at the Office of International Education of OSU for welcoming me to OSU.

Finally I would like to thank my wife, Xiuli, without whose support and patience none of this would have been possible, and my daughter, Paige, whose birth has added new perspective to the project.

Table of Contents

Chapter 1. Introduction	1
Chapter 2. Theoretical Background	5
2.1 Single Particle Models	5
2.1.1 Extreme independent single particle model	5
2.1.2 Single particle model with deformed potential	6
2.2 Collective Models	8
2.2.1 Collective degrees of freedom: basis of collective models	8
2.2.2 The rotation-vibration model (RVM)	13
2.2.3 The general collective model (GCM)	14
2.3 The Unified Models: Particle-core Coupling	16
2.3.1 Weak coupling limit	16
2.3.2 Strong coupling limit	17
2.4 Shape Coexistence - Theoretical Description	19
Chapter 3. Experimental Details - Spectroscopy	21
3.1 The Production of Radioactive Nuclei	21
3.2 Data Acquisition	27
3.2.1 Radiation detection	27
3.2.2 Singles data collection	27
3.2.3 Coincidence data collection	29
3.3 Calibrations	30
Chapter 4. Data Analysis and Results - Spectroscopy	31
4.1 Singles Data Analysis	31
4.2 Multiscaling Data Analysis - Determination of Half-lives	32

4.3 Coincidence Data Analysis - Determination of Internal Conversion Coefficients	45
4.4 Construction of Decay Scheme	53
4.5 Discussion - Ground State Structure of ^{184}Au	53
 Chapter 5. Theory of the Method - Nuclear Orientation	 67
5.1 A Simplified Picture	67
5.2 General Formalism of Nuclear Orientation	68
5.3 The Extraction of Information on Nuclear Structure	73
 Chapter 6. The Apparatus and Experimental Details - Nuclear Orientation	 77
6.1 Introduction: UNISOR Nuclear Orientation Facility (UNISOR/NOF)	77
6.2 The UNISOR ^3He - ^4He Dilution Refrigerator	79
6.2.1 Principle of dilution refrigerator	80
6.2.2 The ^3He - ^4He dilution refrigerator on UNISOR/NOF . .	83
6.3 Nuclear Orientation Thermometry	85
6.4 Sample Preparation	87
6.5 Data Acquisition System	88
6.6 Experimental Procedures of Nuclear Orientation of ^{184}Au	90
 Chapter 7. Data Analysis and Results - Nuclear Orientation	 93
7.1 UNISOR/NOF OLNO Data Analysis	93
7.2 Data Analysis of Nuclear Orientation of ^{184}Au	95
 Chapter 8. Discussions - E0 Transition and Band Mixing	 108
 References	 116

Appendices	120
Appendix A Event Handler Program for Collection of Coincidence	
Data	120
Appendix B The CHIL Codes Used to Scan Tapes to Build	
Coincidence Matrices	123

List of Figures

Fig. 2-1 Energy spectrum of the harmonic quadrupole oscillator.	12
Fig. 2-2 Typical band structure of a pure rotational nucleus.	12
Fig. 2-3 Typical band structure for a deformed even-even nucleus [Gre87]. . .	15
Fig. 2-4 PES reveals γ -softness and shape coexistence for $^{186-196}\text{Pt}$ [Gre87]. . .	15
Fig. 3-1 A schematic diagram of the FEBIAD-B2 ion source [Kir81].	22
Fig. 3-2 A schematic layout of UNISOR facility at ORNL	24
Fig. 3-3 Collection chamber of UNISOR isotope separator	25
Fig. 3-4 Tape transport system on the right beam line [Gum92].	26
Fig. 3-5 The block diagram of the electronic set-up used in a typical UNISOR spectroscopy experiment.	28
Fig. 4-1 Gamma-ray singles spectrum of ^{184}Pt	41
Fig. 4-2 The conversion electron spectrum of ^{184}Pt	42
Fig. 4-3 Typical SAM fitting curve for a portion of gamma-ray spectrum. . .	43
Fig. 4-4 Decay curves of strong gamma transitions in ^{184}Pt	47
Fig. 4-5 Decay curves of strong conversion electrons in ^{184}Pt	48
Fig. 4-6 Portions of gamma-ray and electron spectrum gated on 163-keV (left) and 273-keV (right) γ -rays.	54
Fig. 4-7 Portions of gamma- and electron-spectrum gated on 362-keV (left) and 486-keV (right) γ -rays.	55
Fig. 4-8 Portions of gamma- and electron-spectrum gated on 844-keV (left) and 352-keV (right) γ -rays.	56
Fig. 4-9 Decay scheme of ^{184}Pt from Nuclear Data Sheet [NDS89].	57
Fig. 4-10 Proposed decay scheme of $^{184}\text{Au} \rightarrow ^{184}\text{Pt}$ (coincidences denoted by ●).	58
Fig. 5-1 The illustration of the effect of nuclear orientation for a dipole transition [Gel83].	67
Fig. 6-1 A schematic layout of UNISOR/NOF.	78

Fig. 6-2 The phase diagram of $^3\text{He}/^4\text{He}$ mixture [Oxf88].	80
Fig. 6-3 Simplified schematic diagram of continuously operating refrigerator.	82
Fig. 6-4 Schematic diagram of UNISOR dilution refrigerator.	84
Fig. 6-5 Temperature sensitivity curves for three commonly used thermometers [Mar88].	86
Fig. 6-6 UNISOR/NOF data acquisition system.	89
Fig. 7-1 Temperature curve: count-rates for the 136-keV ^{57}Co thermometer line at 0°	97
Fig. 7-2 Beam rate curve: count-rates for 163-keV ^{184}Pt line at 0°	98
Fig. 7-3 Beam profile: count-rate(0°)/count-rate(180°) for 163-keV ^{184}Pt line.	99
Fig. 8-1 Low-lying levels in ^{184}Pt	109
Fig. 8-2 Portions of gamma (top) and electron (bottom) spectra in coincidence with the 163-keV ($2_1^+ \rightarrow 0_1^+$) transition.	110
Fig. 8-3 Portions of the gamma (top) and electron (bottom) spectra in coincidence with the 486-keV ($2_2^+ \rightarrow 2_1^+$) transition.	111
Fig. 8-4 Portions of the gamma (top) and electron (bottom) spectra in coincidence with the 777-keV ($3_1^+ \rightarrow 2_1^+$) transition.	112

List of Tables

Table 4-1 Energies and relative intensities of gamma rays placed in the decay of ^{184}Au to ^{184}Pt	33
Table 4-2 A compilation of half-lives of strong gamma transitions in ^{184}Pt	44
Table 4-3 A compilation of half-lives of strong conversion electrons in ^{184}Pt	46
Table 4-4 Important gamma-gamma relationships placed in $^{184}\text{Au} \rightarrow ^{184}\text{Pt}$	50
Table 4-5 Intensity balance for levels in $^{184}\text{Au} \rightarrow ^{184}\text{Pt}$ ($I_{\gamma}, 163\text{-keV} = 100$).	65
Table 4-6 Comparison of relative intensities	66
Table 7-1 Compilation of a_2 and a_4 coefficients for the strong tansitions in the decay of $^{184}\text{Au} \rightarrow ^{184}\text{Pt}$	100
Table 7-2 Mixing ratios of low-lying $\Delta I=0$ transitions in ^{184}Pt	107
Table 8-1 Low-lying $\Delta I = 0$ Transitions in ^{184}Pt	114

A Study of the Decay $^{184}\text{Au} \rightarrow ^{184}\text{Pt}$ by Means of Gamma and Electron Spectroscopy and Low Temperature Nuclear Orientation

Chapter 1. Introduction

There has been an increased interest in recent years in the studies of nuclei far from the valley of β stability due to the development of new experimental facilities. To some extent, those studies have transformed our understanding on the shapes and structure of nuclei. One of the new pictures that have emerged in nuclear structure is shape coexistence. Contrary to the idea that one nucleus has only one permanent shape (either spherical, or well-deformed), many nuclei have been found to possess two distinct shapes in the low-lying structure. Since the discovery of the coexistence of complete bands of energy levels built on different deformations in Hg isotopes [Ham76], shape coexistence has been established as a widely-occurring low-energy degree of freedom of the nucleus, and the study of this new phenomenon has been providing new tests of the models which have been developed to describe nuclear structure. Among the many nuclei that have been studied for shape coexistence, the nuclei in the region where $78 \leq Z \leq 83$ and $98 \leq N \leq 120$ are of particular importance since it is the most extensive region known to exhibit coexisting shapes. ^{184}Pt , the nucleus of present study, belongs to this mass region.

The coexistence between different structures in $^{182-188}\text{Hg}$ has been thoroughly investigated and experimentally well established [Ham85]. The ground state deformations of those isotopes are found to be oblate, while the excited bands are believed to possess prolate shapes. In even-even Pt isotopes, shape coexistence has been observed in $^{176-178}\text{Pt}$ [Dra86] and $^{182-186}\text{Pt}$ [Fin72]. However, even-even Pt isotopes are even more intriguing since experimental data suggested that Pt isotopes change ground state structure from prolate shape to oblate shape in going from the light to heavy isotopes. Kumar and Baranger[Kum68] predicted that the transition should occur between $A = 186$ and $A = 192$.

Various models have been applied to describe shape coexistence. The General

Collective Model, which states that shape coexistence occurs when there is a double minimum in the potential energy surface, has been used to describe shape coexistence in Hg and Pt isotopes [Rag80, Fra80]. Bengtsson et al.[Ben87] also calculated the potential energy surfaces for a large number of nuclei in the Pt-Hg mass region and predicted the deformations of ground states and of secondary minima in the potential. Another approach, which is based on the concepts that deformation is caused by valence nucleons interacting through the proton-neutron force [Sha53] and shape coexistence occurs when intruder orbitals lie at very low energies [Woo82], has been successfully applied in describing the shape coexistence in Hg and Pt isotopes [Zga88].

There is also an emerging picture of wide-spread occurrence of strong electric monopole (E0) transitions associated [Zga88] with shape coexistence. It has been suggested [Hey88] that the E0 strength can serve as a fingerprint of strong mixing between states with different shapes. To establish the association of large E0 transition strength with band-mixing requires a more systematic survey of E0 transitions over a range of isotopes that are found to possess two different shapes and more vigorous theoretical investigations. We have undertaken a detailed study of shape coexistence and E0 transitions in ^{184}Pt as the first attempt in trying to understand this association.

^{184}Pt has been studied by Finger et al.[Fin72] and Cailliau et al.[Cai74], who identified the gross features of the coexisting bands. It has been determined by potential energy surface calculations [Ben87] that the ground state band has a deformation of $\beta = 0.22$, corresponding to a prolate shape, and the excited secondary minimum occurs at deformation of $\beta = -0.16$ with an oblate shape. The calculation also predicted the band head energy of the excited band to be around 500 keV, which roughly agrees with the experimental value (492 keV). Both previous experimental studies yielded decay schemes of $^{184}\text{Au} \rightarrow {}^{184}\text{Pt}$, but they are far incomplete, and many energy levels and transitions were not placed in the decay scheme. As indicated by the following equation, the relative E0 strength (e.g. $I_e(\text{E0})/I_e(\text{E2})$) can be obtained only by combining internal conversion coefficients from spectroscopy study with E2/M1 mixing ratios from anisotropy measurements in nuclear orientation:

$$\alpha(E0+M1+E2) = \frac{\delta^2 \alpha(M1) + (1+\delta^2)\alpha(E2)}{1+\delta^2} \quad (1)$$

where $q^2 = I_e(E0)/I_e(E2)$, $\delta = I_\gamma(E2)/I_\gamma(M1)$, $\alpha(M1) = I_e(M1)/I_\gamma(M1)$, $\alpha(E2) = I_e(E2)/I_\gamma(E2)$, I represents the transition intensity, and α is the internal conversion coefficient.

The experimental technique developed and extensively utilized at UNISOR can be applied to accurately determine α_K values of even weak transitions or of transitions of complex multipolarities, but a quantitative analysis can not be done unless the E2/M1 multipole mixing ratio of the transition is known. On the other hand, the full analysis of nuclear orientation data is not possible without a detailed decay scheme. In the present study of the decay $^{184}\text{Au} \rightarrow ^{184}\text{Pt}$, the spectroscopy and nuclear orientation experiments were run in tandem. The spectroscopy data (γ - γ coincidence, e- γ coincidence and internal conversion electron spectroscopy) can be analysed to elucidate the decay scheme, which is necessary for the analysis of nuclear orientation data, and the results from nuclear orientation data analysis in turn can help assign as well as confirm some level spins and transition multipolarities.

Even-even Hg isotopes are actually the ideal cases for the study of shape coexistence, and would provide a much better test of the use of E0 amplitudes and E2/M1 mixing ratios. Unfortunately, orienting the Tl isotopes (parents of Hg isotopes) is not practical at present, due to the small magnetic dipole moments and magnetic hyperfine fields. The ^{184}Au decay has a half-life of 53 s, and its magnetic moment is predicted to be reasonably large. It is also the shortest-lived isotope proposed for the UNISOR Nuclear Orientation Facility. If orienting such a short-lived activity on-line is successful, it will provide a convincing demonstration of the potential of the facility.

In summary, the following is a list of the primary goals of this study:

- 1) Study γ and internal conversion electron spectroscopy data (including γ - γ , e- γ coincidences as well as γ and electron multiscaling data) and update the decay scheme of $^{184}\text{Au} \rightarrow ^{184}\text{Pt}$.
- 2) Identify and establish low-spin, low-energy coexisting bands in ^{184}Pt .

3) Determine the E2/M1 mixing ratios in interband transitions (between states with same spin) from nuclear orientation data, and combine them with electron conversion coefficients to extract relative strength of E0 transitions.

4) Interpret the result of both data analyses to clarify the association of E0 transitions with mixing of two bands with different deformations.

Chapter 2 discusses the theoretical background for this study. Chapter 3 discusses the experimental facilities and apparatus set-up for the spectroscopy experiment. Chapter 4 deals with the spectroscopy data analysis, and presents the discussion and interpretation of the results of spectroscopy data analysis. Chapters 5 to 7 discuss low-temperature nuclear orientation of ^{184}Au , and chapter 8 combines the discussion of nuclear orientation data with the results from the spectroscopy experiment.

Chapter 2. Theoretical Background

The ultimate goal of the study of nuclear structure is to describe the properties of complex nuclei in terms of interactions between two nucleons. Since the nature of the nuclear force (between two nucleons) is not well understood, and a complex nucleus is a many-body system for which the Hamiltonian has no simple solution, simplifying assumptions are always made based on empirical data. Different models have been developed either to account for a certain nuclear property or to interpret the properties of nuclei over a specific mass region. Studies of nuclei in the last two decades have improved our understanding of nuclear structure tremendously and also put new and stringent demands on the development of new theoretical models. Thus the development of models that can explain a variety of nuclear properties and can track changes over long sequences of nuclei has become important. In this chapter, along with the introduction of early nuclear models, newly developed models relevant to this study will be presented.

2.1 Single Particle Models

2.1.1 Extreme independent single particle model

The success of atomic theory based on the shell model in describing the atomic structure prompted early nuclear physicists to take the similar approach to attack the problem in nuclear structure. Much experimental evidence supports the possible existence of nuclear shell structure (e.g. the sudden and discontinuous behavior of nucleon separation energies suggests the idea of "magic numbers"). The nuclear shell model was first developed by Mayer, Jensen, Haxel and Suess [May57], and was based on the assumption that in a nucleus of mass A , the A^{th} nucleon moves in a potential formed by all of the other nucleons. Since the force between nucleons is not well understood, the exact form of the nuclear potential can not be derived. Originally two potentials, the infinite well and the harmonic oscillator, were used to solve the

three-dimensional Schrödinger equation, and only three existing "magic numbers" were predicted. Later the model was improved by adopting a more realistic form of potential (Woods-Saxon) and by including a spin-orbit term. The improved model successfully produces all nuclear "magic numbers" and predicts the existence of islands of isomerism. It is very successful in accounting for ground-state spin-parity assignments of almost all odd- A nuclei, and is also, to some degree, successful in accounting for magnetic moments and electric quadrupole moments.

2.1.2 Single particle model with deformed potential

The extreme independent single particle model is based on the assumption that the nuclear potential is spherical, which, we know, is not true for nuclei away from closed shells (e.g. $150 \leq A \leq 190$ and $A > 230$). Experimental evidence indicates that many nuclei possess permanent deformation. For these nuclei the potential that approximates the actual nuclear shape should be used in calculating energy levels. Nilsson [Nil55] extended the shell model to include permanent deformation by using an axially symmetric harmonic oscillator potential with spin-orbit correlation and other correction terms. The single particle Hamiltonian can be expressed as:

$$H = \frac{\mathbf{p}^2}{2m} + \frac{1}{2}m[\omega_{\perp}^2(x^2+y^2)+\omega_z^2z^2] + Cl \cdot s + Dl^2. \quad (2)$$

The second term represents the axially symmetric harmonic oscillator potential, and the effect of the last term is to flatten the potential shape and make it into a more box-like well. C and D are constants, and they can be determined by matching the single particle states of zero deformation with the experimental results for spherical nuclei. ω_{\perp} and ω_z are functions of deformation parameter δ :

$$\omega_{\perp}^2 = \omega_0^2(1 + \frac{2}{3}\delta); \quad \omega_z^2 = \omega_0^2(1 - \frac{4}{3}\delta). \quad (3)$$

Requiring the volume of the nucleus to be conserved under deformation leads to: $\omega_x\omega_y\omega_z = \text{constant}$, and the dependence of ω_0 on δ as:

$$\omega_0(\delta) = \omega_0(0) \left(1 - \frac{4}{3}\delta^2 - \frac{16}{27}\delta^3\right)^{-1/6}. \quad (4)$$

The Nilsson Hamiltonian can be rewritten as follows:

$$H = H_0 + H_\delta + Cl \cdot s + Dl^2, \quad (5)$$

where

$$H_0 = \frac{1}{2} \hbar \omega_0 (-\nabla^2 + r^2) \quad (6)$$

and

$$H_\delta = -\delta \hbar \omega_0 \frac{4}{3} \left(\frac{\pi}{5}\right)^{1/2} r^2 Y_{20}(\theta). \quad (7)$$

Choosing the eigenstates of H_0 and l^2 , $|N\Lambda\Sigma\rangle$, as basis states, we can diagonalize the total Hamiltonian in this representation to obtain the single particle states for deformed potential. This can be done only numerically. The eigenstates of the total Hamiltonian $|\Omega\alpha\rangle$ are linear combination of basis states:

$$|\Omega\alpha\rangle = \sum_{l,\Lambda}^{l=\Sigma+\Lambda} A_{l\Lambda} |N\Lambda\Sigma\rangle \quad (8)$$

Among those quantum numbers, only $\Omega = \Lambda + \Sigma$ is a good quantum number. As it turned out, in the limit of large deformation, Λ , Σ and n_z (the oscillator quanta in the z direction) all approximately become good quantum numbers. These three are called the "asymptotic" quantum numbers of the state $|\Omega\alpha\rangle$. Even in cases far away from the asymptotic limits, it has become customary to label Nilsson states with $[Nn_z\Lambda\Omega]$, or $\Omega[Nn_z\Lambda]$. The Nilsson model has had tremendous success in accounting for the nuclear properties for odd- A nuclei in the deformed region.

2.2 Collective Models

The nuclear shell models have enjoyed tremendous successes in accounting for ground state spin-parity assignments, magic numbers, alpha and beta decay systematics and so forth. In spite of all those great successes, there exist many limitations. The agreements between observed electric quadrupole moments and the shell model predictions in most cases are poor. The transition probabilities of low-lying states are normally greater than single-particle estimates. In the regions away from closed shells, rotational and vibrational band structure occur, which can not be explained by the shell models. Many properties that nuclei exhibit can not be identified with the motion of individual nucleons. Instead their origin lies in the collective motion of nucleons, the motion in which many nucleons move coherently with well-defined phases. All those observations lead to the development of various collective models.

2.2.1 Collective degrees of freedom: basis of collective models

The collective motion of nuclei consists of shape oscillation of the nuclear surface about an equilibrium spherical shape (the vibrational degree of freedom) and of rotations of the nucleus as a permanently deformed rigid body (the rotational degree of freedom). Instead of describing a nucleus by its $3A$ degrees of freedom, the collective models are formulated in terms of collective coordinates $\alpha^{[\lambda]}$, which are functions of the $3A$ nuclear coordinates. The collective coordinates are normally introduced on the basis of classical pictures, such as the vibrating surface or rotating body. The Hamiltonian is then constructed following general invariance principles. The collective coordinates that describe the nuclear surface motion are defined by the expansion of the surface into spherical harmonics $Y_{\lambda\mu}(\theta\phi)$:

$$R(\theta, \phi, t) = R_0 [1 + \sum_{\lambda, \mu} (-1)^\mu \alpha_{\lambda-\mu}(t) Y_{\lambda\mu}(\theta, \phi)] \quad (9)$$

where $\alpha^{[\lambda]} = \{\alpha_{\lambda\mu}\}$ with $\mu = \lambda, \lambda-1, \dots, -\lambda$ are time dependent, describing the

oscillating nuclear surface according to equation 9, and they are also components of an irreducible tensor of rank λ , transforming accordingly.

For the closed shell nuclei, the equipotentials are spheres with $R = R_0$. The nucleons outside the closed shell polarize the spherical field, giving rise to a deformed average field whose equipotential may be described by equation 9. The position coordinates on the equipotential surface can then be described by $\alpha_{\lambda\mu}$. Different λ values specify the modes of deformations. $\lambda = 2$ gives quadrupole deformation, while $\lambda = 3$ gives octupole deformation. The experimental vibrational and rotational spectra indicate that the $\lambda = 2$ term in equation 9 is a dominant term. The nuclear surface with only quadrupole deformation is described by:

$$R = R_0 [1 + \sum_{\mu} \alpha_{\mu}^* Y_{2\mu}(\theta, \phi)] \quad (10)$$

where $\alpha_1 = \alpha_{-1} = 0$, $\alpha_2 = \alpha_{-2}$. α_0 and α_2 describe the shape of the "intrinsic" nucleus.

Bohr [Boh52, Boh54] introduced two deformation parameters γ and β by defining:

$$\alpha_0 = \beta \cos \gamma, \quad \alpha_2 = \frac{1}{2} \sqrt{2} \beta \sin \gamma. \quad (11)$$

Their significance of these two parameters is clearly manifested in the following equation:

$$\delta R_i = \left(\frac{4}{5} \pi \right)^{1/2} \beta \cos \left(\gamma - \frac{2}{3} i \pi \right) \quad (12)$$

where $i=1,2,3$ for x,y,z . From this equation we can see that the nucleus is axially symmetric if $\gamma = 0^\circ, 60^\circ, 120^\circ, \dots$, and it has a prolate shape if $\alpha_0 > 0$ and oblate shape if $\alpha_0 < 0$.

Assuming the nuclei have only quadrupole deformation, the Hamiltonian can be written in terms of kinetic energy $T(\pi^{[2]}, \alpha^{[2]})$ and potential energy $V(\alpha^{[2]})$:

$$H = T(\pi^{[2]}, \alpha^{[2]}) + V(\alpha^{[2]}) \quad (13)$$

where $\pi^{[2]}$ is the canonically conjugate momentum for $\alpha^{[2]}$. If $\alpha^{[2]}$ is small, we can expand H in a series:

$$T(\pi^{[2]}, \alpha^{[2]}) = \left(\frac{1}{2}\sqrt{5}/B_2\right)[\pi^{[2]} \times \pi^{[2]}]^{[0]} + B_3[[\pi^{[2]} \times \alpha^{[2]}]^{[2]} \times \pi^{[2]}]^{[0]} + \dots, \quad (14)$$

and

$$V(\alpha^{[2]}) = \frac{1}{2}\sqrt{5} C_2[\alpha^{[2]} \times \alpha^{[2]}]^{[0]} + C_3[[\alpha^{[2]} \times \alpha^{[2]}]^{[2]} \times \alpha^{[2]}]^{[0]} + \dots \quad (15)$$

The B 's and C 's are called the "inertia parameter" and "stiffness parameter", characterizing the inertia of the collective motion and the stiffness of potential energy $V(\alpha)$, respectively. These parameters can be obtained either by fitting the experimental data or by calculating from a more sophisticated nuclear model. The Hamiltonian describes the collective motion in terms of the variable $\alpha^{[2]}$. Whether it represents vibration about spherical equilibrium, or rotating deformed nucleus, or rotating and vibrating deformed nucleus is determined by the structure of the potential energy $V(\alpha)$.

In the vibrational limit of collective motion (assuming only vibration exists in nuclei), the simple yet important case is the harmonic quadrupole oscillator, where the Hamiltonian can be written as:

$$H_{HQ} = -(2B_2)^{-1} \sum_{\mu} \pi_{2\mu}^* \pi_{2\mu} + \frac{1}{2} C_2 \sum_{\mu} \alpha_{2\mu}^* \alpha_{2\mu} \quad (16)$$

Introducing the phonon operator $\beta_{2\mu}$, we have:

$$H_{HQ} = \hbar \omega_2 \sum_{\mu} (\beta_{2\mu}^* \beta_{2\mu} + \frac{1}{2}) \quad (17)$$

where

$$\omega_2 = \sqrt{C_2/B_2} \quad (18)$$

is the frequency of the harmonic oscillator. By further introducing the phonon number operator $n_{2\mu} = \beta_{2\mu}^+ \beta_{2\mu}$, we have:

$$H_{HQ} = \hbar\omega_2 \sum_{\mu} (n_{2\mu} + \frac{1}{2}) \quad (19)$$

The eigenvalues of H_{HQ} give the energy levels:

$$E = (N + \frac{5}{2})\hbar\omega_2 \quad (20)$$

with parity $\pi = (-1)^{\lambda}$. For the quadrupole harmonic oscillator ($\lambda=2$), $\pi=+1$ for all energy levels. The spectrum pattern is shown in Fig. 2-1. The ground state is the phonon vacuum state ($N=0$) with angular momentum $I = 0$. The first excited state has one phonon ($N=1$) with $I = 2$. The second excited state is a two phonon state ($N=2$), and it is 3-fold degenerate with $I = 0^+, 2^+, 4^+$. $N=3$ represents the 3 phonon state, which is 5-fold degenerate with $I = 0^+, 2^+, 3^+, 4^+, 6^+$. Many even-even nuclei near closed shells are found to exhibit a similar pattern of energy spectra.

The limiting case for nuclear rotational motion is the rigid rotor, where the Hamiltonian is simply $H = L^2/2\mathfrak{J}$. \mathfrak{J} is the moment of inertia, and the energy eigenvalues are:

$$E_I = \frac{\hbar^2}{2\mathfrak{J}} I(I+1) \quad (21)$$

where I can only take even values due to the symmetrization of wavefunctions. The ideal energy spectrum pattern is shown in Fig. 2-2. Rotational spectra can be observed only in deformed nuclei. They are found in the mass regions $150 < A < 190$ and $A > 220$.

The actual nuclei are far more complex than those limiting cases. The energy spectra are often found to exhibit both rotational and vibrational energy levels. To

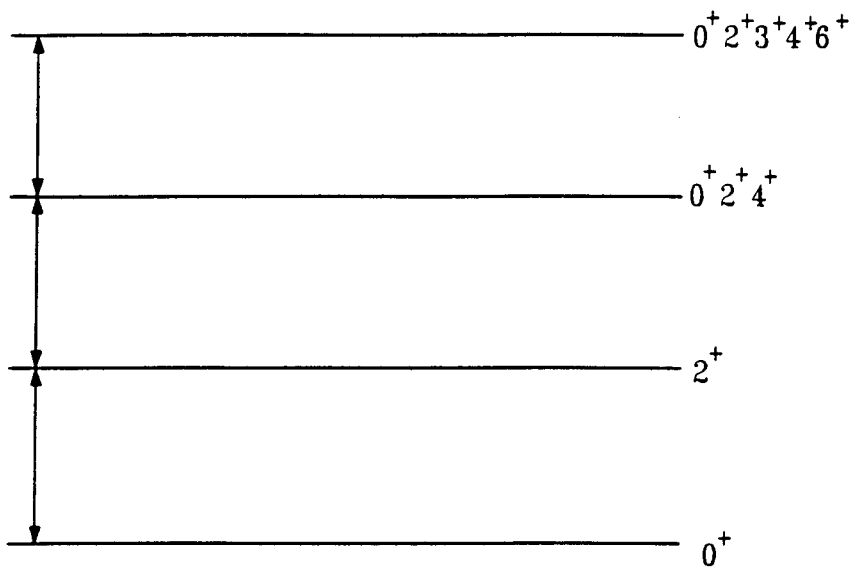


Fig. 2-1 Energy spectrum of the harmonic quadrupole oscillator.

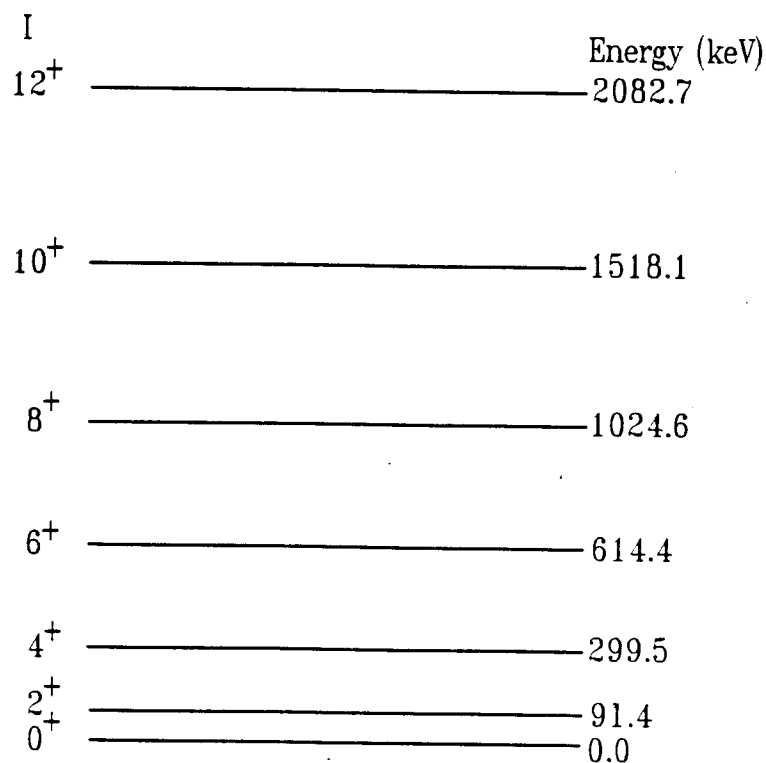


Fig. 2-2 Typical band structure of a pure rotational nucleus.

describe the collective motion of actual nuclei, more sophisticated models are necessary.

2.2.2 The rotation-vibration model (RVM)

The rotation-vibration model treats deformed nuclei as undergoing both rotational and vibrational collective motion at the same time. It was first proposed by A. Bohr [Boh52]. Faessler[Fae65] later solved the Hamiltonian systematically for deformed nuclei with β - and γ -vibrations. The Hamiltonian can be expressed in three terms, with the third term being small and treated as a perturbation:

$$H = H_{\text{rot}} + H_{\text{vib}} + H_{\text{rot-vib}} \quad (22)$$

The energy eigenvalues and eigenfunctions of $H_{\text{rot}} + H_{\text{vib}}$ can be solved exactly, and they are shown as equation 23 and 24. The selection rules for the rotational quantum number I are obtained purely from the symmetrization of the wavefunctions.

$$|IMKn_2n_0\rangle = \frac{(2I+1)}{16\pi^2(1+\delta_{K0})} [D_{MK}{}^{I*}(\theta_j) + (-1)^I D_{M-K}{}^{I*}(\theta_j)] \chi_{K,n_2}(\eta) |n_0\rangle \quad (23)$$

$$E_{IKn_2n_0} = (I(I+1)-K^2) \frac{1}{2}\epsilon + \left(\frac{1}{2}|K|+1+2n_2\right) E_\gamma + \left(n_0 + \frac{1}{2}\right) E_\beta \quad (24)$$

where

$$K=0,2,4,\dots \text{ with } I=0,2,4,\dots \text{ for } K=0 \text{ and } I=K,K+1,K+2,\dots \text{ for } K\neq0 \quad (25)$$

For a given set of K , n_0 , n_2 , the change of I forms a band. The energy spectrum usually consists of rotational energy levels built on vibrational band-heads. There exist two major types of vibrations, β - and δ -vibration. The β -vibrations enlarge and shorten the ellipsoid along the symmetry axis, preserving the axial symmetry; while the δ -vibrations represent motion perpendicular to the symmetry axis, breaking the symmetry of the ellipsoid. Many nuclei exhibit the band structure predicted by the

rotation-vibration model. Fig. 2-3 is a typical band structure for a deformed even-even nucleus. The introduction of the $H_{\text{rot-vib}}$ term causes the states of three bands to mix and results in a spin-dependent correction to the moment of inertia of the nucleus.

2.2.3 The general collective model (GCM)

The models presented previously deal with quadrupole excitation, and treat nuclear collective motion as small amplitude motion around definite static deformations. However, many nuclei exhibit no well-defined deformation. For some nuclei the collective potential possesses either a shallow minimum, or a small stiffness, and for others there even exist two or more different shapes at the same time (shape coexistence). In general, the potential energy surfaces of nuclei are much more complex, the small-amplitude approximation is not valid, and the general collective Hamiltonian needs to be solved. The first attempt in this direction was made by Kumar and Baranger [Kum65, Kum67], and later Gneuss and Greiner developed a model using potential which is flexible enough for a large number of nuclei. Hess et al.[Hes80] improved the Gneuss-Greiner version in 1980 and 1981, which leads to a general collective model.

In the general collective model, the collective Schrödinger equation can be solved by diagonalizing the Hamiltonian within the basis of the five-dimensional harmonic oscillator. Eigenfunctions are constructed analytically. The collective properties are determined by the mass parameters and by the potential energy surface which shows pictorially the dynamic collective properties of the nucleus (e.g. the existence of structure isomerism and the γ -softness of the nucleus). The potential and kinetic energies in the model are chosen as general as possible, and all other simple models are contained in it and can be treated as a limit.

Nuclear shape coexistence can be described by the general collective model. Shape coexistence occurs when there are two (or more) local minima in the potential energy surface. Each minimum corresponds to a particular static deformation. The collective wave functions localized around the minimum belong to the sequence of energy levels characteristic of that particular deformation. Fig. 2-4 shows the potential

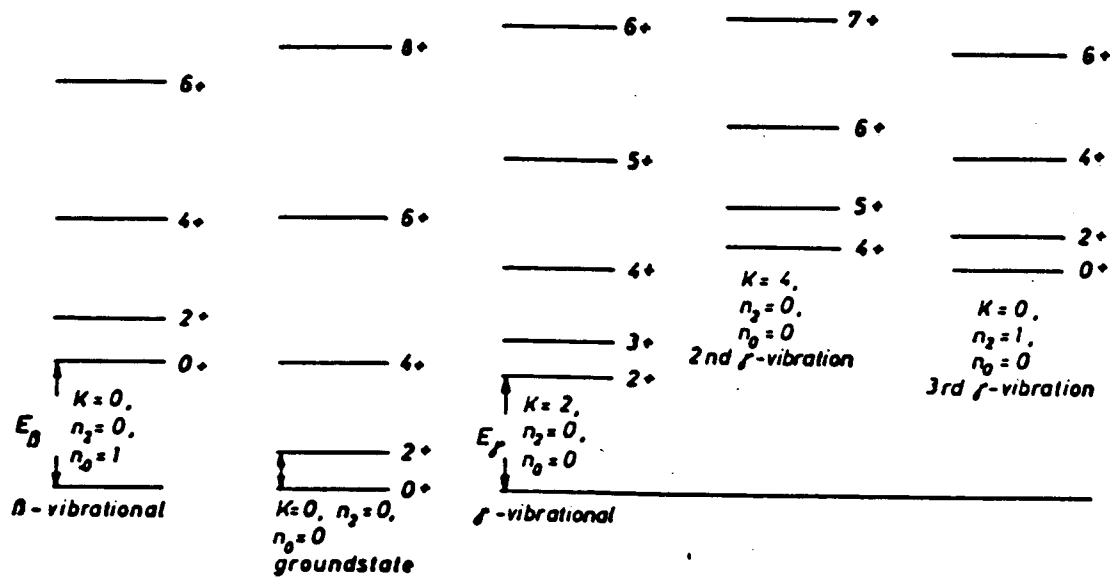


Fig. 2-3 Typical band structure for a deformed even-even nucleus [Gre87].

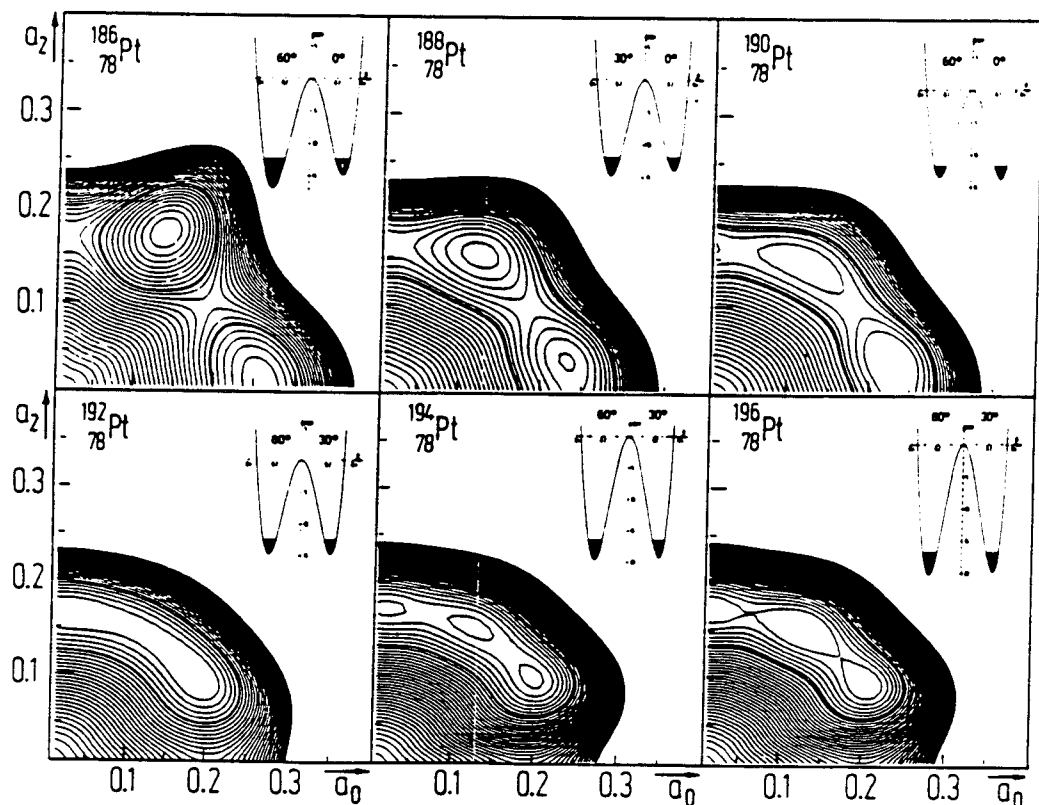


Fig. 2-4 PES reveals γ -softness and shape coexistence for $^{186-196}\text{Pt}$ [Gre87].

energy surfaces for $^{186-196}\text{Pt}$. Clearly two minima in PES for ^{186}Pt indicate the coexistence of two shapes. It can also be seen that some nuclei exhibit strong γ -softness.

2.3 The Unified Models: Particle-core Coupling

The previous discussions on nuclear models (both single particle and collective models) treated nuclear collective and single particle degrees of freedom separately. The shell models were developed without taking account of collective modes of nuclear motion. For odd- A nuclei, however, the average nuclear field experienced by single particles is formed by the even-even core which undergoes both vibration and rotation. In these cases, the interaction between single particle and collective degrees of freedom has to be considered. The general approach for particle-core coupling is to treat the unpaired nucleon explicitly, and lump all the other nucleons into the core. The Hamiltonian then takes the form of equation 26, where H_{core} is the Hamiltonian for the even-even core which can be treated by the Rotation-Vibration Model, Asymmetric Rotator Model, or General Collective Model. $H_{\text{s.p.}}$ describes the unpaired particle moving in shell-model potential, and H_{int} represents the coupling between the particle and the core:

$$H = H_{\text{core}} + H_{\text{s.p.}} + H_{\text{int}} \quad (26)$$

Depending on the strength of the coupling (strong coupling and weak coupling) and the way the particle is coupled to the core, many models have been developed. A few of the most commonly used will be presented.

2.3.1 Weak coupling limit

For nearly spherical nuclei with small surface vibration, the coupling is expected to be weak. H_{int} can be treated as perturbation to the Hamiltonian $H_{\text{core}} + H_{\text{s.p.}}$. If only quadrupole vibration of the surface is considered for collective motion of the core and the spherical shell model is used for single particle motion, the

Hamiltonian for odd- A nuclei can be of the form:

$$H = H_{\text{coll}} + H_{\text{s.p.}} + H_{\text{int}} \quad (27)$$

where

$$H_{\text{coll}} = \frac{1}{2B} \sum_{\mu} |\pi_{2\mu}|^2 + \frac{1}{2} C \sum_{\mu} |\alpha_{2\mu}|^2, \quad (28)$$

$$H_{\text{s.p.}} = \frac{\mathbf{p}^2}{2m} + \frac{1}{2} m \omega^2 r^2 + \mathbf{C} \mathbf{l} \cdot \mathbf{s} + D \ell^2, \quad (29)$$

$$H_{\text{int}} = -m \omega^2 r^2 \sum_{\mu} \alpha_{2\mu}^* Y_{2\mu}. \quad (30)$$

The solutions for H_{coll} and $H_{\text{s.p.}}$ are known previously. If $|NIm_1\rangle$ and $|jm_2\rangle$ designate the collective and single particle eigenstates respectively, the eigenstates for $H_{\text{coll}} + H_{\text{s.p.}}$ can be built from collective and single particle spaces, i.e.,

$$|NIjM\rangle = \sum_{m_1, m_2} (IjJ | m_1 m_2 M) |NIm_1\rangle |jm_2\rangle \quad (31)$$

The pattern of energy levels of $H_{\text{coll}} + H_{\text{s.p.}}$ is similar to that of collective vibrational motion except that states with $I \neq 0$ become multiplets which are degenerate when $H_{\text{int}} = 0$. The non-zero H_{int} breaks the degeneracy of these states, and mixes all the multiplets with the same spin and parity. The admixture depends on the particular shell model configuration as well as on the collective properties of the nucleus.

2.3.2 Strong coupling limit

For well-deformed nuclei, H_{int} can be quite strong and it can no longer be treated as small perturbation. The total Hamiltonian still takes the same form, but, $H_{\text{s.p.}}$ should represent a single particle Hamiltonian in deformed shell model, and H_{coll} should be the collective Hamiltonian for the deformed nuclei (e.g. rotation-vibration hamiltonian). The core has a momentum of M , and all extra outer nucleons have a

total angular momentum of \mathbf{J} . The angular momentum of the whole system \mathbf{I} is the vector sum of \mathbf{M} and \mathbf{J} . In the strong coupling limit, the good quantum numbers are Ω and K , the projections of \mathbf{J} and \mathbf{I} along the symmetry axis of the nucleus respectively.

The Hamiltonian of the system can be written in the following form, where H_{coll} describes the rotating and vibrating core, $H_{s.p.}$ is the shell model Hamiltonian for single particle moving in deformed potential (Nilsson Model), and H' represent all the small coupling terms including the particle-rotation coupling (Coriolis coupling):

$$H = H_{\text{coll}} + H_{s.p.} + H' \quad (32)$$

Neglecting the particle-rotation coupling the energy eigenvalues are given by:

$$E = E_\Omega + \frac{1}{2}\epsilon[I(I+1) - (K-\Omega)^2] + (\frac{1}{2}|K-\Omega| + 1 + 2n_2)E_\gamma + (n_0 + \frac{1}{2})E_\beta \quad (33)$$

where E_Ω is the single particle energy in the Nilsson model.

The energy spectrum consists of rotational bands with $I = \Omega, \Omega+1, \Omega+2, \dots$ built on each single particle state. There are also β - and γ -vibrational excitations of the core in addition to the single-particle excitations. The effect of the particle-rotation (Coriolis) coupling is to add an extra term E' [equation 34] to the energy expressed by equation 33:

$$E' = -a[(-1)^{I+\frac{1}{2}}(I+\frac{1}{2})]\frac{1}{2}\epsilon\delta_{K,\frac{1}{2}} - 2K\Omega\frac{1}{2}\epsilon \quad (34)$$

where a is called decoupling parameter. The Coriolis coupling of the $K = 1/2$ bands can be very large, and it causes large distortion of energy level spacing of the bands.

The general characteristic of odd- A deformed nuclei is rotational bands built on single-particle states described by the Nilsson model. The unified model has been very successful in describing the properties of the odd-particle in the deformed region.

2.4 Shape Coexistence - Theoretical Description

Since the discovery of shape coexistence in nuclei, different theoretical approaches have been taken to describe the phenomena. The general collective model, through the use of potential energy surface, has successfully accounted for the coexisting properties of many nuclei. It has been used to explain shape coexistence in the light Hg isotopes [Rag80] and to predict deformation parameters for both Hg and Pt isotopes [Ben87]. As discussed in 2.2.3 the shape coexistence occurs when there is a double minimum in the potential energy surface, giving rise to two different, metastable deformed shapes. Another approach is of microscopic nature. It is based on the concepts that the nuclear deformation is caused by the residual proton-neutron force among the valence nucleons [Sha53]. In singly-closed nuclei, there is only one type of valence nucleon. These nuclei exhibit no deformation, since there is no proton-neutron force among valence nucleons. By exciting other type of nucleons out of the closed shell, nucleons of both types interact to produce shape deformation. Shape coexistence corresponds to the coexistence of two different valence nucleon configurations.

Nuclei with a closed shell \pm a pair of protons or a pair of neutrons have quite different structure. It is believed that in some nuclei the interaction between the proton and neutron pair is the cause for shape deformation and shape coexistence occurs when there is an excitation of a proton or neutron pair across a major shell. Zganjar [Zga88] suggests that for Pt isotopes shape coexistence is caused by the excitation of a proton pair from within one major shell into the next higher major shell ($d_{3/2}$ to $h_{9/2}$), creating coexisting proton-hole configuration ($\pi(4h)$ and $\pi(2p-6h)$).

Experimental evidence indicates that E0 transition strength between states of the same spin and parity is linked to the mixing of states of two different shapes [Hey88]. Kantele [Kan84] and Heyde [Hey88] used a semiempirical two-level mixing model to explain why this band mixing causes enhancement of E0 transitions. In the shell model, the electric monopole operator is defined by

$$O(E0) = \sum_{i=1}^A e_i r_i^2 \quad (35)$$

where e_i is the charge on the i^{th} nucleon at distance r_i . The diagonal matrix elements of the E0 operator give charge radii squared while the off-diagonal matrix elements yield the transition amplitudes. If a nucleus possesses states of two different deformations, the differences in charge radii squared should be observed. In the simple two-level mixing model, the mixed states are expressed in terms of unmixed states, as listed below:

$$|0_1^+\rangle = a|0_a^+\rangle + b|0_b^+\rangle, \quad |0_2^+ = -b|0_a^+\rangle + a|0_b^+\rangle, \quad (36)$$

where $a^2 + b^2 = 1$. The matrix element of monopole operator between the two mixed states can be written:

$$\langle 0_2^+ | r^2 | 0_1^+ \rangle = ab \Delta_{ba} \langle r^2 \rangle + (a^2 - b^2) \langle r^2 \rangle_{ab}, \quad (37)$$

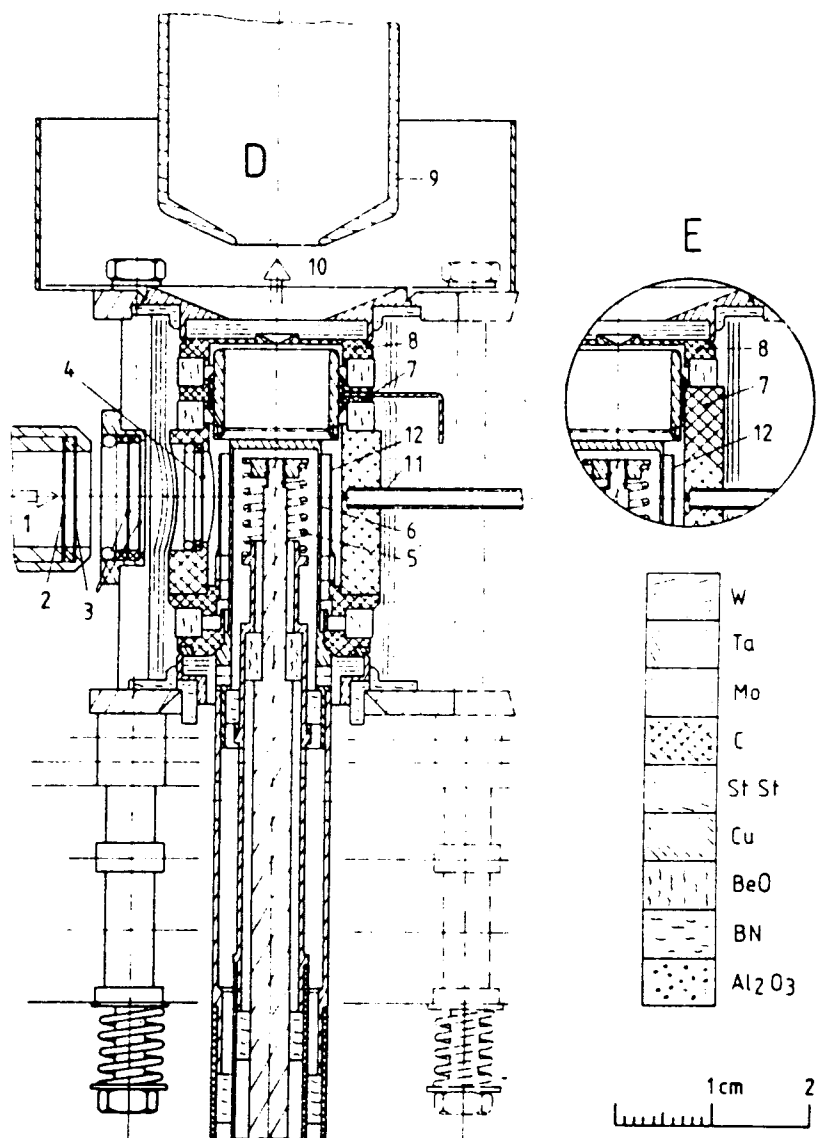
where $\Delta_{ba} = \langle r^2 \rangle_b - \langle r^2 \rangle_a$ is the difference of mean radii squared of two unmixed states and $\langle r^2 \rangle_{ab} = \langle 0_a^+ | r^2 | 0_b^+ \rangle = \langle 0_b^+ | r^2 | 0_a^+ \rangle$. This suggests that if mean radii squared are different and there is mixing between the two states E0 transition between $|0_1^+\rangle$ and $|0_2^+\rangle$ will be enhanced. E0 transitions between states of the same spin and parity can be used to help identify coexisting states and understand the band mixing. In terms of energy levels the band mixing tends to displace the mixed states.

Chapter 3. Experimental Details - Spectroscopy

The experiment for the study of the decay of $^{184}\text{Au} \rightarrow ^{184}\text{Pt}$ was performed at the UNISOR (UNiversity Isotope Separator at Oak Ridge) facility which comprises an isotope separator operated on-line to the 25-MV folded tandem accelerator at the Holifield Heavy-Ion Research Facility, Oak Ridge, Tennessee. UNISOR is a consortium of 12 universities formed in 1971 for the purpose of nuclear structure studies of nuclei far from stability. In 1987, the UNISOR Nuclear Orientation Facility (NOF), a ^3He - ^4He dilution refrigerator on-line to the mass separator, was commissioned [Gir88].

3.1 The Production of Radioactive Nuclei

The excited states of ^{184}Pt were studied through the radioactive decay of ^{184}Au ($t_{1/2} = 53$ s). The radioactive nuclei of ^{184}Au were produced by bombarding the thin target made of ^{181}Ta with a heavy-ion beam (^{12}C) from the tandem accelerator. In choosing the beam type and target material for the production of the desired nuclei, ^{184}Au in this study, the Projection Angular-Momentum Coupled Evaporation code (PACE2, [HHIRF Computer Handbook]) was used. Given the specific target and beam type, the program calculates and generates as its output the total reaction cross-section as well as the cross-section for each of all possible reaction products. The target thickness and beam energy were further determined by running program STOPX [HHIRF Computer Handbook], which calculates the energy loss of the beam in the target. The optimum thickness of Ta target and energy of ^{12}C beam for this experiment were 5×9.4 mg/cm 2 , and 140 MeV, respectively. They were chosen so that the production yield of the reaction $^{181}\text{Ta}(^{12}\text{C}, 9n)^{184}\text{Au}$ was maximized and all reaction products could recoil out of the target material due to the momentum transfer from the heavy-ion beam. The target foils were mounted in the window of the separator ion source. Fig. 3-1 is a schematic diagram of the FEBIAD-B2 ion source [Kir81]



FEBIAD-D ion source with separately heated catcher. The inset shows part of the simplified version FEBIAD-E, where catcher and anode potential are identical. (1) UNILAC beam; (2) foil target ($2\text{--}5 \text{ mg/cm}^2$); (3) carbon heat-shields ($\sim 20 \mu\text{g/cm}^2$); (4) tantalum window ($0.8\text{--}1.5 \text{ mg/cm}^2$); (5) filament for electron bombardment heating of the (6) tantalum capsule cathode; (7) anode with grid for primary electron extraction; (8) outlet plate; (9) extraction electrode; (10) separator beam; (11) gas line, in version D used also as electrical support for the (12) catcher electrode.

Fig. 3-1 A schematic diagram of the FEBIAD-B2 ion source [Kir81].

employed in this experiment. The main purpose of the ion source was to collect all nuclear reaction products and ionize them to a positive charge for mass separation. To achieve the maximum separation efficiency, all reaction products need to be ionized with the same amount of charge (normally singly charged) so that all products having the same mass would have the same charge-to-mass ratio. The compound nuclei formed from the nuclear reaction were recoiled from the target material and deposited into the "catcher" made of thin (typically $\leq 1 \text{ mg/cm}^2$) tantalum metal in which they became neutral atoms by picking up electrons. The ion source was operated at a temperature as high as 1800°C . The high temperature was achieved and maintained by the continuous electron bombardment of the tantalum capsule cathode from the filament. The electron bombardment also caused the cathode to emit a large number of electrons from its surface which in turn formed a small plasma region where neutral atoms, being evaporated from the "catcher", were ionized. The positive singly charged ions were then extracted by the electric potential of 50 kV on the extractor and sent to the separator for mass separation. Stable, natural xenon isotopes in gaseous form injected into the ion source as well as the existing tantalum atoms were used for mass calibration of the separator.

Fig. 3-2 is a schematic diagram of the layout of UNISOR facility, showing all the major equipment items. The facility is based on a Danfysik isotope separator on-line to the tandem accelerator. The separator has a 90-degree deflection and 1.5 m radius of curvature. The analyzing magnet can provide either a beam spot or a line focus with a mass resolution of $\Delta m/m < 1/2000$, and a mass range of $\pm 8\%$ can be collected in the collection chamber shown schematically in Fig. 3-3. Three beam lines coming out the separator are used to guide the beam to counting stations for on-line experiments, and radioactive sources of longer half-life can also be collected on the focal plane in the collection chamber which can be removed for off-line measurements. Since nuclear reactions normally produce nuclei of several masses, data collection for two (or more) nuclei can be conducted concurrently when necessary. The central beam line leads the mass-separated products to the Nuclear Orientation Facility which will be described in detail in Chapter 6 of this presentation.

UNISOR
University Isotope Separator—Oak Ridge

ORAU 817

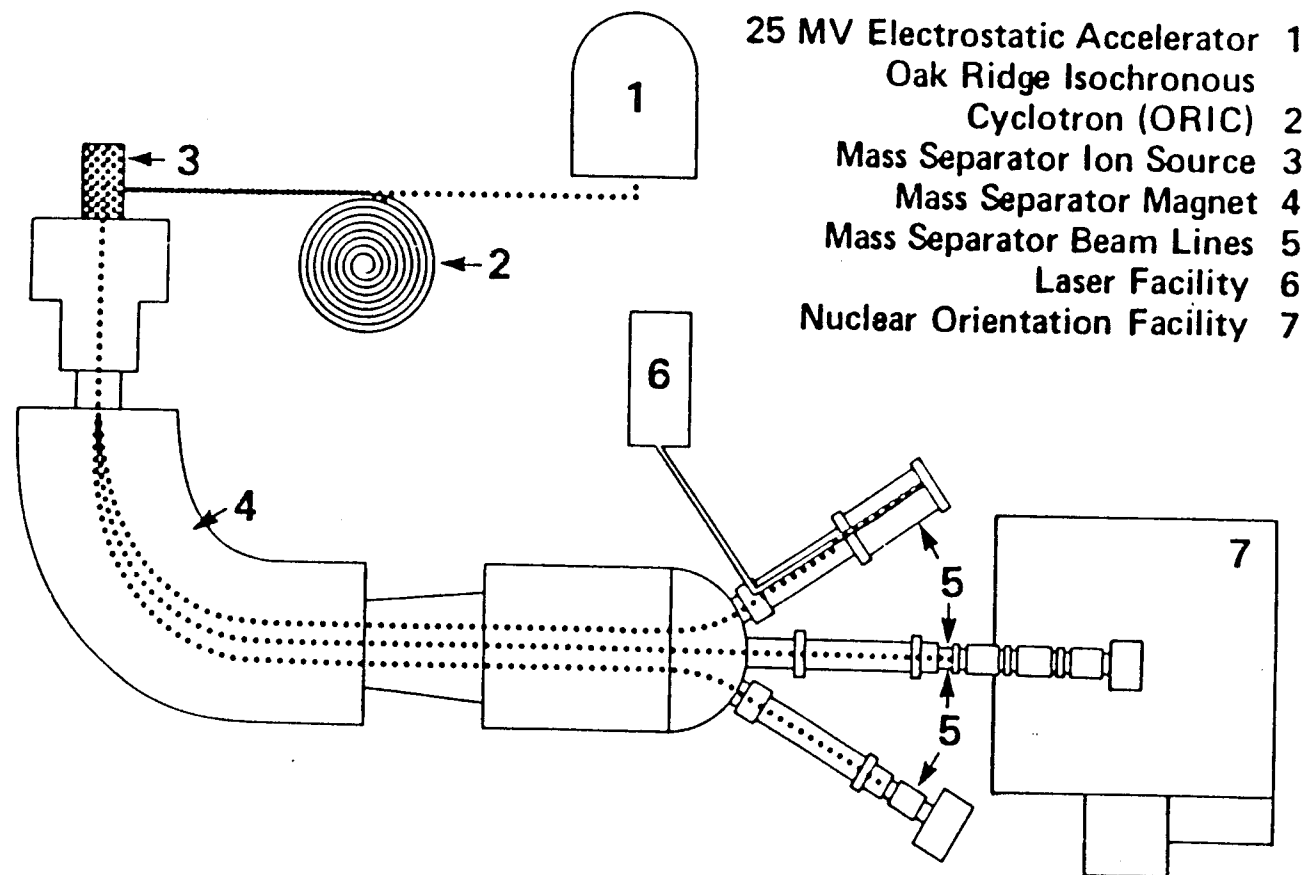


Fig. 3-2 A schematic layout of UNISOR facility at ORNL

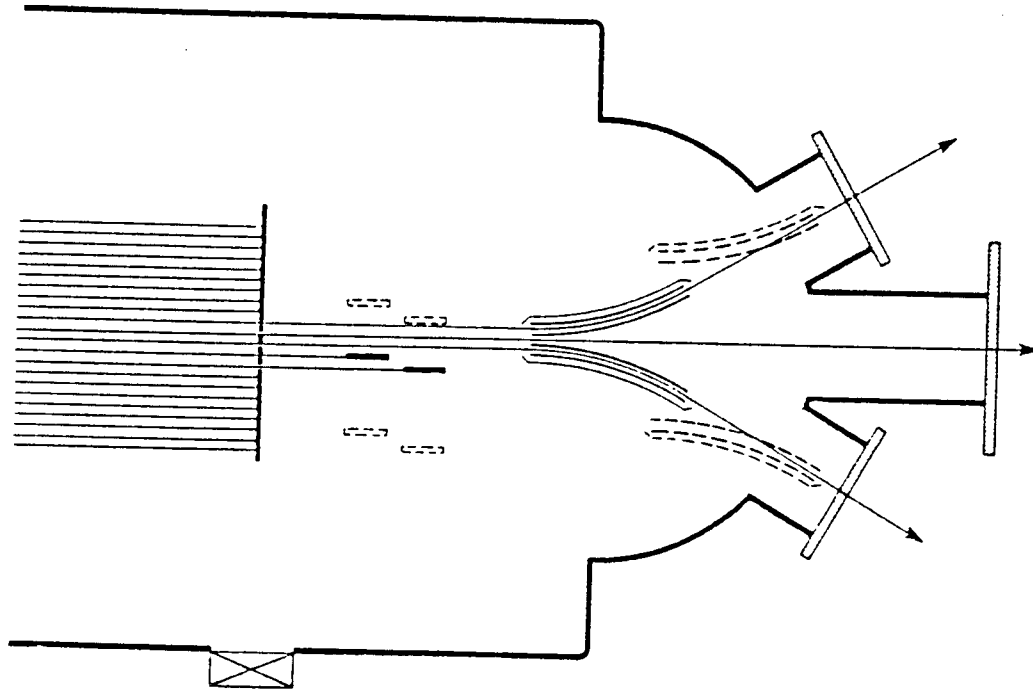


Fig. 3-3 Collection chamber of UNISOR isotope separator.

Two pairs of deflection plates were installed in the collection chamber to guide the selected beam into the side beam lines; they can be adjusted externally to intercept beams of different masses. The left beam line is used for laser spectroscopy experiments. The decay-spectroscopy measurement of ^{184}Au was taken on the right beam line which is equipped with a tape transport system shown in Fig. 3-4. It consists of a continuous loop of magnetic recording tape, wound on a reel and driven by a step motor. The extracted beam of ^{184}Au was focused and deposited on the tape, and the collected samples were transported to the counting stations. The new samples were being collected while the previously collected ones were counted. The system was controlled by data acquisition software, running in a continuous mode to make use of beam efficiently.

Tape
transport

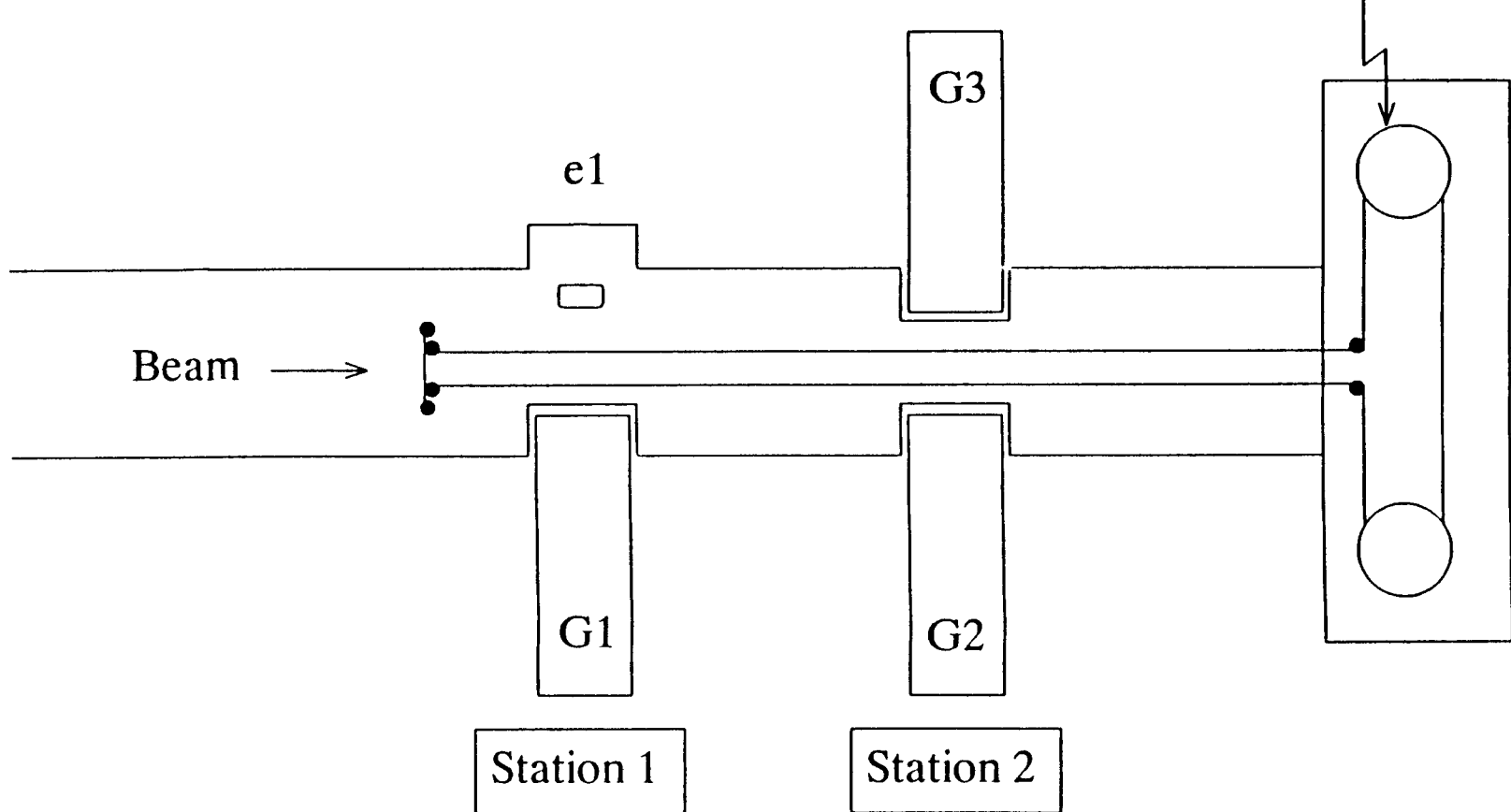


Fig. 3-4 Tape transport system on the right beam line [Gum92].

3.2 Data Acquisition

3.2.1 Radiation detection

The detecting system of the spectroscopy experiment consists of three Ortec Ge(Li) detectors for gamma-ray measurements and one Si(Li) detector for conversion electron measurement. Two Ge(Li) detectors were placed opposite each other to collect gamma-gamma coincidence data, and one Ge(Li) detector and the Si(Li) detector were set up in the same way for conversion-electron-gamma coincidence. All four detectors were used to take multiscaling data concurrently (See Fig. 3-4 for the schematic diagram of the detector set-up). The resolutions of the Ge(Li) detectors were around 1.74 keV (FWHM) to 1.98 keV at 1332 keV. The Si(Li) electron detector was of KeVex type, with a surface area of approximately 200 mm², depletion depth of 3 mm, and a resolution of 2.30 keV at 975 keV. It was part of the "mini-orange" spectrometer system designed and built at Louisiana State University by Dr. E. F. Zganjar to be used specifically on the UNISOR on-line spectroscopy facility. The system was maintained within its own vacuum system, consisting of a bellows, a liquid nitrogen cryostat, an ion-pump, a gate valve connecting with the beam line and a "mini-orange" magnet used to minimize the positron background and focus electrons onto the Si(Li) detector. The independent vacuum system allows changes of experimental set-up without the long time delay caused by the warm-up and cool-down of the detector. The distance between the detector and the radioactive source could be adjusted by cranking the bellows screw. In this study the "mini-orange" magnet was not used in order to increase the counting statistics.

3.2.2 Singles data collection

The electronic circuitry consisted of all standard NIM modules through which signals from the detectors were shaped and amplified (Fig. 3-5 shows the block diagram of electronics used in this work). Two computer-based (Tennecomp and HHIRF Concurrent 3230 by Perkin-Elmer) data acquisition systems interfaced to the

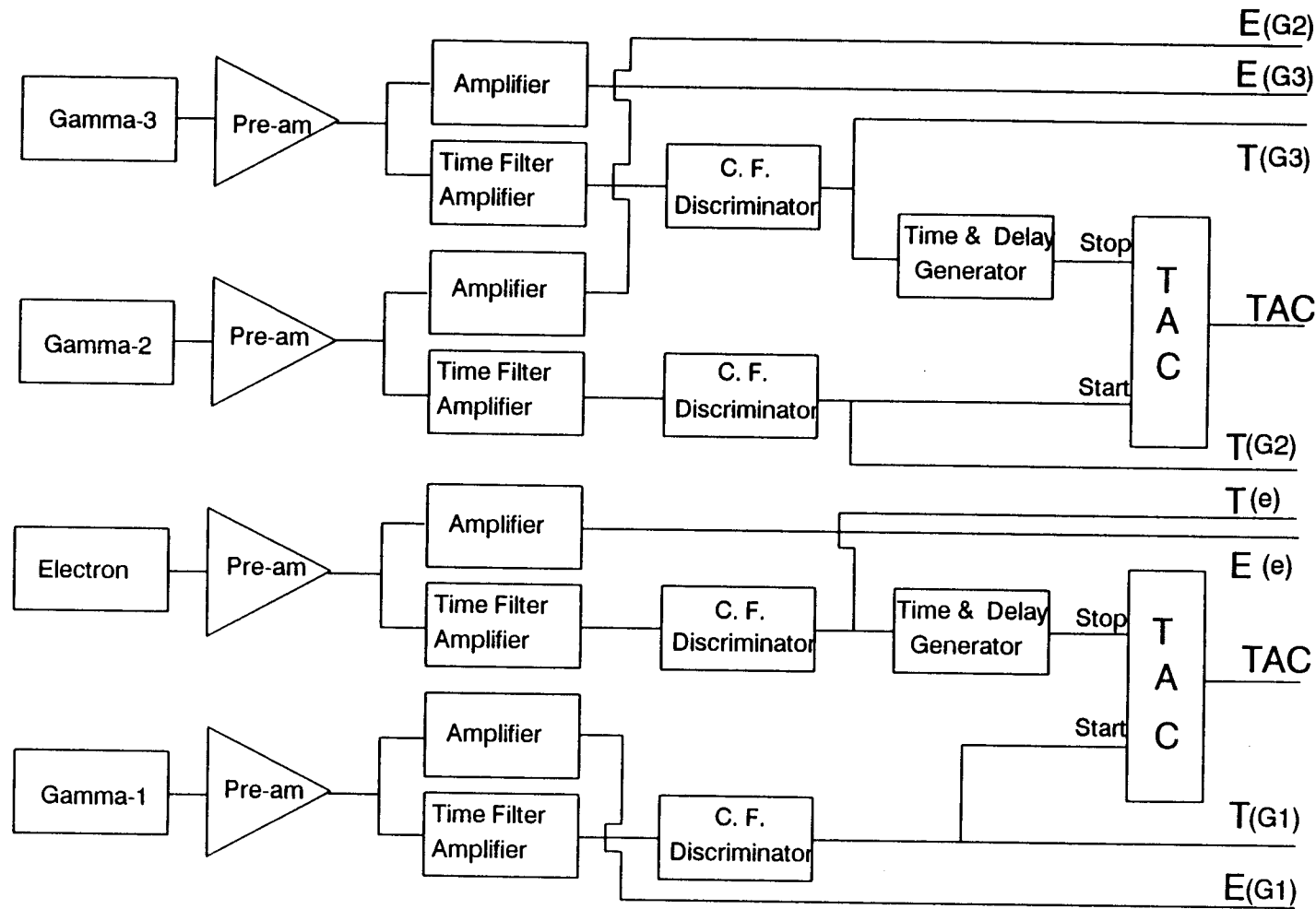


Fig. 3-5 The block diagram of the electronic set-up in a typical UNISOR spectroscopy experiment.

detecting electronics via analog-to-digital converters (ADC) were used to collect data in this experiment. The gamma-ray and conversion electron singles data were taken in multiscaled mode, using PDP-11 computer-based Tennecomp TP-5000 system[Spe81] which is part of the UNISOR facility. This system has 6 Nuclear Data ADC's, 1600 bpi magnetic tape drive, a hard disk drive and live display of spectrum. It is capable of acquiring the singles data for a maximum of 6 detectors in the multiscaling mode as well as two 3-parameter coincidence data simultaneously. The programs written in the machine language TIL (Tennecomp Interactive Language [Bai75]) are available for running standard spectroscopy experiment and controlling the external devices (start/stop of ADCs, tape transport system, beam switch, etc.). An interface between Tennecomp and Perkin-Elmer exists which allows the singles spectrum to be transferred directly to the Perkin-Elmer where extensive spectrum analysis programs are available and the plotting features of those programs can be used to monitor on-going experiments. Sources extracted from the separator were collected on the tape and counted for 60 seconds in 30 time planes with 2 seconds for each time plane. The tape transport system controlled by the multiscaling program moved the tape and brought the freshly collected source to counting stations in every 60 seconds. The multiscaled data were mainly used to determine the halflives of different gamma-rays in the spectrum and aid in the assignments of a particular gamma-ray to the proper nucleus by following its decay or growth from plane to plane.

3.2.3 Coincidence data collection

The three-parameter (energy-energy-time) gamma-gamma and conversion-electron-gamma coincidence data were taken concurrently with the singles data, using HHIRF Perkin-Elmer Concurrent 3230 computer system. The data were collected and built into an event-by-event data stream by a CAMAC-based, programmable controller called the "Event Handler"[Hen79] which executes a user-defined procedure describing the experimental hardware configuration and the structure of the data stream. A Macro-like language is available for programming this device. The data

stream, read out from CAMAC modules by the Event Handler, was put into a FIFO buffer in the host computer, and written in a fixed format on 6250 bpi magnetic tape drives for subsequent processing. This data acquisition system also allows one to process the data simultaneously, generating histogram files to monitor the quality of the data being taken. The coincidence data would be used to determine conversion electron coefficients, establish the coincidences among different gamma rays and eventually aid in the construction of decay scheme. The processing and analysis will be described in more detail in the next chapter.

3.3 Calibrations

Energy and efficiency calibrations were performed before and after the spectroscopy run. For gamma-ray calibration, absolutely calibrated NBS (National Bureau of Standards) source 4275 was used. The source is a mixture of radioactive nuclides containing ^{125}Sb - $^{125\text{m}}\text{Te}$, ^{154}Eu and ^{155}Eu , and has an energy range of 27 to 1596 keV for x and gamma rays. The absolute emission rates were given at a reference time for all the lines in the spectrum, and detector efficiency calibration could be made accordingly. A source containing a mixture of ^{133}Ba and ^{207}Bi placed in the same geometry as that of separated source on the tape was used to perform the electron energy calibration, and known conversion coefficients for electron lines in those nuclei were used to obtain the efficiency calibrations for the electron detector. ^{22}Na and ^{207}Bi were used to set up the timing for gamma-gamma coincidence and electron-gamma coincidence, respectively. The 59 keV x ray of ^{241}Am was used as reference to set the discrimination level on the Constant Fraction Discriminators.

Chapter 4. Data Analysis and Results - Spectroscopy

The complexity of the level structure of the nuclei far from stability requires experimental data of highest statistical quality. With the advent of large-volume high-resolution detectors and computerized data acquisition systems with large storage capabilities, the collection of large volume of high quality spectral data has become possible. To process and analyze the large amount of complicated nuclear spectral data, many numerical techniques and computer programs have been developed. The data analysis in this study was done mainly on HHIRF Concurrent 3230 computer system where a variety of programs for spectral analysis is available. The software package has been developed by the staff of the computer facility at ORNL to process data acquired utilizing the HHIRF facility. Some of this analysis were performed at OSU on the Micro-Vax where a HHIRF software package modified for use on VAX machines is available. During the analysis process another spectrum-fitting program, SAMPO [Rou69] has been used intensively.

4.1 Singles Data Analysis

The gamma ray and conversion electron singles data were analyzed using program SAMPO. This program was developed originally by Routti et al. in 1969 for computer analysis of gamma-ray spectra from semiconductor detectors, and it has been modified many times and adapted to run on many different machines. The program fits the photopeaks, in the least-squares sense, as a Gaussian center with simple exponential tails on both sides. The tails join the Gaussian at the points where the function and its first derivative are continuous. Three parameters, the width of the Gaussian and the distances from the centroid to the junction points, are used to define the peak. These shape parameters are sensitive to small variations in experimental configurations, and they vary smoothly with energy. They are determined, once for every experimental set-up, by fitting the intense and well-isolated lines in the

spectrum, and interpolation is used for values of these parameters for any line. The background can be chosen either as a straight line or as a polynomial. Once the shape, energy and efficiency calibration parameters are entered, the program can be run either automatically to find the peaks and do the fitting, or interactively with the user specifying the fitting interval, number and the positions of the peaks in the interval. The output of SAMPO includes peak positions with deviation in channel number and energy, intensities with associated errors and relative intensities normalized to the strongest peak in the spectrum. The program is advantageous for fitting closely-lying multiplets, and it is capable of fitting up to eight peaks within one interval. However, some multiplets have peaks so closely clustered together that gated coincidence technique has to be used in order to determine their relative intensities.

The multiscaled gamma-ray and conversion electron data, collected during the whole spectroscopy run, were checked for deficiencies (gain shift, poor resolution and high background), and summed up to construct singles spectra of good statistics, using program DAM (Data Analysis and Manipulation [HHIRF computer manual]). The gamma-ray singles spectrum from the decay of ^{184}Au to ^{184}Pt is shown in Fig. 4-1, and the conversion electron spectrum is shown in Fig. 4-2. The energies and relative intensities for individual gamma-rays were determined from the SAMPO fit of the gamma-ray sum spectrum, and they are listed in columns 1 and 2 of Table 4-1.

4.2 Multiscaling Data Analysis - Determination of Half-lives

Multiscaling data (30 time planes with 2 seconds per time plane) were collected at the first counting station for both gamma-rays and conversion electrons. Both the gamma-ray and conversion electron multiscaling data consist of 30 spectra, with each spectrum containing the data of a single time plane accumulated throughout the spectroscopy run. All 30 spectra were analyzed using program SAM (Spectrum Analysis and Manipulation [HHIRF Computer Manual] which is an interactive gaussian peak-fitting routine. In using SAM the goodness of the fits was judged by viewing the fitting curves on a monitor. Fig. 4-3 illustrates a typical fitting curve for

Table 4-1 Energies and relative intensities of gamma rays placed in the decay of ^{184}Au to ^{184}Pt .

E_γ (keV) ^{a)}	I_γ ^{a,b)}	E_i (keV)	E_f (keV)	Comment
118.9		1794.5	1675.6	[1]
157.0	0.05 ^{c)}	648.7	491.7	
162.97(4)	100.00	163.0	0.0	
221.85(4)	5.81(7)	2552.8	2330.9	
272.93(4)	89.9(9)	435.9	163.0	
279.1	0.37 ^{c)}	1306.9	1027.8	
280.63(39)	0.33(14)	1453.6	1172.5	
291.02(5)	0.43(2)	939.7	648.7	
294.44(6)	0.33(2)	1234.2	939.7	
297.30(6)	0.41(2)	1469.9	1172.5	
328.6	0.66 ^{c)}	1172.5	843.9	
328.77(3)	3.34(5)	491.7	163.0	
352.12(4)	1.14(3)	843.9	491.7	
362.33(3)	41.4(5)	798.2	435.9	
367.18(5)	1.47(7)	1306.9	939.7	
376.98(4)	0.97(3)	2330.9	1953.9	
379.13(3)	2.69(4)	1027.8	648.7	
390.2		2330.9	1940.7	[1]
390.37(3)	2.23 ^{c)}	1234.2	843.9	
404.36(4)	0.49(2)	1431.7	1027.8	
408.07(3)	1.21(2)	843.9	435.9	
423.77(17)		1730.6	1306.9	[1]Poor fit
425.27(27)	0.79 ^{c)}	1597.4	1172.5	Poor fit
432.24(3)	4.24(11)	1230.5	798.2	
434.77(5)	3.76(19)	1462.5	1027.8	
441.29(6)	1.11(7)	1675.6	1234.2	

Table 4-1 (continued)

E_{γ} (keV) ^{a)}	I_{γ} ^{a,b)}	E_i (kev)	E_f (kev)	Comment
447.89(3)	0.43(1)	2330.9	1882.9	
479.02(4)	0.82(3)	2330.9	1852.1	
485.73(3)	11.8 ^{c)}	648.7	163.0	
487.6		1794.5	1306.9	[1]
491.7		491.7	0.0	Pure E0
491.94(10)	0.70(11)	1431.7	939.7	
503.89(5)	1.91 ^{c)}	939.7	435.9	
525.22(4)	0.39 ^{c)}	1172.5	648.7	
530.2		1469.9	939.7	Pure E0
531.11(5)	0.73(2)	2330.9	1799.7	
565.39(5)	0.60(2)	1799.7	1234.2	
569.56(7)	0.68(4)	1597.4	1027.8	
575.99(12)	0.80(4)	1883.0	1306.9	
578.95(21)	0.24(6)	1519.0	939.7	
585.2		2552.8	1967.6	[1]
585.5	0.79 ^{c)}	1234.2	648.7	
585.9		2330.9	1745.0	[1]
587.65(6)	0.93(4)	1431.7	843.9	
591.89(5)	6.93(19)	1027.8	435.9	
600.37(6)	0.57(2)	2330.9	1730.6	
609.41(14)	0.60(15)	1453.6	843.9	
626.22(7)	0.34(2)	1469.9	843.9	
648.66(5)	5.90(10)	648.70	0.0	
653.78(16)	0.41(7)	2453.0	1799.7	
660.92(7)	0.47(3)	2460.6	1799.7	
664.22(4)	4.23 ^{c)}	1462.5	798.2	
665.0	0.63 ^{c)}	1693.0	1027.8	

Table 4-1 (continued)

E_γ (keV) ^{a)}	I_γ ^{a,b)}	E_i (keV)	E_f (keV)	Comment
669.93(7)	0.60(3)	2552.8	1882.9	
672.95(9)	1.10(10)	2104.6	1431.7	
676.0		2108.0	1431.7	[1]
680.8	0.54 ^{c)}	1172.5	491.7	
680.9	1.24 ^{c)}	843.9	163.0	
691.07(5)	1.06(3)	1630.8	939.7	
700.31(81)	0.12(18)	2330.9	1630.8	
736.89(8)	0.31(2)			[2]
753.0	1.47 ^{c)}	1693.0	939.7	
753.1		2552.8	1799.7	[1]
753.5	0.59 ^{c)}	1597.4	843.9	
758.65(5)	0.64(2)			[2]
771.87(11)	0.40(4)	1799.7	1027.8	
776.80(4)	12.12(13)	939.7	163.0	
783.0		2302.0	1519.0	[1]
783.0	1.58 ^{c)}	1431.7	648.7	
784.80(8)	1.00(6)			[2]
798.40(5)	3.18(4)	1234.2	435.9	
800.62(7)	0.54(3)	2652.8	1852.1	
805.43(7)	0.50(2)	2536.3	1730.6	
807.71(6)	0.63(2)	2552.8	1745.0	
808.3		2608.0	1799.7	[1]
811.53(5)	0.82(2)	2611.2	1799.7	
821.2	0.64 ^{c)}	1469.9	648.7	
822.0		2453.0	1630.8	[1]
822.2		2552.8	1730.6	[1]
826.47(7)	1.13(6)	2652.8	1826.4	

Table 4-1 (continued)

E_γ (keV) ^{a)}	I_γ ^{a,b)}	E_i (keV)	E_f (keV)	Comment
830.6		2460.6	1630.0	[1]
831.09(5)	5.11(6)	1630.0	798.5	
838.31(8)	0.32(2)	1682.1	843.9	
843.93(5)	9.50(12)	843.9	0.0	
855.1	0.58 ^{c)}	1882.9	1027.8	
858.0				[1][2]
864.85(5)	3.25(5)	1027.8	163.0	
868.22(7)	1.63(8)	2330.9	1462.5	
869.8	0.64 ^{c)}	1713.7	843.9	
870.3	0.51 ^{c)}	1519.0	648.7	
871		2975	2104.6	[1]
871.0	8.40 ^{c)}	1306.9	435.9	
898.83(5)	1.03(2)	2330.9	1431.7	
918.10(7)	0.42(2)	2631.8	1713.7	
922.0		2552.8	1630.8	[1]
923.36(5)	2.14(4)	2637.6	1713.7	
932.33(6)	1.21(4)	1730.6	798.2	
938	0.37 ^{c)}	1736	798.2	
939.8	0.62 ^{c)}	1967.6	1027.8	
941.1	0.26 ^{c)}	1785.0	843.9	
948.7	0.59 ^{c)}	1597.4	648.7	
964	0.45 ^{c)}	1613	648.7	
983.0				[1][2]
990.0				[1][2]
995.75(8)	0.57(3)	1431.7	435.9	
1001.46(4)	2.06(4)	1799.7	798.2	
1009.60(4)	4.11(6)	1172.5	163.0	

Table 4-1 (continued)

E_{γ} (keV) ^{a)}	I_{γ} ^{a,b)}	E_i (keV)	E_f (keV)	Comment
1024.00(11)	0.25(2)	2330.9	1306.9	
1026.54(5)	2.85(9)	1462.5	435.9	
1033.92(5)	0.87(2)	1469.9	435.9	
1041.0				[1][2]
1065.0	0.27 ^{c)}	1713.7	648.7	
1071.34(4)	4.28(5)	1234.2	163.0	
1073.87(5)	1.35(3)	2536.3	1462.5	
1083.1	1.21 ^{c)}	1519.0	435.9	
1084.7	2.13 ^{c)}	1882.9	798.2	
1090.16(4)	4.49(6)	2552.8	1462.5	
1096.04(28)	0.21(5)	1894.0	798.2	
1100.37(5)	1.67(4)	2330.9	1230.5	
1142.47(10)	0.43(3)	1940.7	798.2	
1155.70(4)	1.59(3)	1953.9	798.2	
1161.59(5)	1.33(3)	1597.4	435.9	
1167.66(4)	1.43(3)	2637.6	1469.9	
1169.4	≤ 0.63	1967.6	798.2	
1172.51(6)	0.97(3)	1172.5	0.0	
1175.5	0.55 ^{c)}	1613	435.9	
1177.7	0.45 ^{c)}	1826.4	648.7	
1218	0.12 ^{c)}	1710	491.7	
1221.98(8)	0.49(3)	2453.0	1230.5	
1229.43(5)	1.00(3)	2536.3	1306.9	
1239.71(5)	1.02(3)	1675.6	435.9	
1245.9		2552.8	1306.9	[1]
1246.2	5.31 ^{c)}	1682.1	435.9	
1263.46(8)	0.38(2)	2063.0	798.2	

Table 4-1 (continued)

E_γ (keV) ^{a)}	I_γ ^{a,b)}	E_i (keV)	E_f (keV)	Comment
1274.25(11)	0.25(2)	2074.0	798.2	
1290.58(7)	0.62(3)	1453.6	163.0	
1293.24(8)	0.47(3)	1785.0	491.7	
1303.1	0.46 ^{c)}	2330.9	1027.8	
1306.84(5)	1.44(3)	1469.9	163.0	
1309.22(5)	1.95(4)	1745.0	435.9	
1322.24(5)	0.78(2)	2552.8	1230.5	
1356.05(10)	0.57(5)	1519.0	163.0	
1359.77(60)	0.34(7)	2159.0	798.2	
1363.76(6)	1.01(4)	1799.7	435.9	
1371.47(7)	0.42(2)	2171.0	798.2	
1390.45(8)	0.45(2)	1826.4	435.9	
1397.36(4)	2.57(4)	2631.8	1234.2	
1416.20(5)	1.41(4)	1852.1	435.9	
1418.38(9)	0.50(3)	2652.8	1234.2	
1449.0				[1][2]
1455.50(12)	0.35(3)	2253.7	798.2	
1459.3	0.59 ^{c)}	2631.8	1172.5	
1489.2	0.42 ^{c)}	1926.0	435.9	
1504.73(7)	0.59(3)	1940.7	435.9	
1519.10(5)	1.52(4)	1682.1	163.0	
1524.93(4)	2.35(6)	2552.8	1027.8	
1531.7	0.66 ^{c)}	1967.6	435.9	
1532.64(5)	1.32(4)	2330.9	798.2	
1545.61(7)	0.52(3)	1982.0	435.9	
1550.77(8)	1.23(9)	1713.7	163.0	
1596.0		2394.0	798.2	[1]

Table 4-1 (continued)

E_{γ} (keV) ^{a)}	I_{γ} ^{a,b)}	E_i (keV)	E_f (keV)	Comment
1610.91(8)	0.41(3)	2048.0	435.9	
1614.16(11)	0.31(2)	2554.0	939.7	
1643.95(8)	0.38(2)	1808.0	163.0	
1654.31(8)	0.37(2)	2453.0	798.2	
1663.15(5)	1.04(4)	1826.4	163.0	
1671.56(12)	0.24(2)	2611.2	939.7	
1689.10(9)	0.43(3)	1852.1	163.0	
1691.92(8)	0.49(3)	2631.8	939.7	
1697.94(5)	1.31(4)	2637.6	939.7	
1712.0	0.15 ^{c)}	2203.0	491.7	
1713.09(5)	1.68(5)	2652.8	939.7	
1716.21(11)	0.31(2)	1879.0	163.0	
1722.43(5)	0.99(3)	2159.0	435.9	
1738.31(9)	0.61(4)	2536.3	798.2	
1754.62(4)	5.33(13)	2552.8	798.2	
1794.14(7)	0.48(3)	2637.6	843.9	
1804.60(5)	0.96(3)	1967.6	163.0	
1813.44(4)	5.05(11)	2611.2	798.2	
1848.23(5)	1.07(3)	2011.2	163.0	
1894.0	0.54 ^{c)}	2692.0	798.2	
1919.0	0.56 ^{c)}	2717.0	798.2	
1983.19(7)	0.53(3)	2631.8	648.7	
1988.99(5)	1.27(3)	2637.6	648.7	
2025.44(17)	0.27(3)	2824.0	798.2	
2040.0	0.56 ^{c)}	2203.0	163.0	
2040.3	0.16 ^{c)}	2532.0	491.7	
2116.98(4)	1.99(4)	2552.8	435.9	

Table 4-1 (continued)

E_{γ} (keV) ^{a)}	I_{γ} ^{a,b)}	E_i (keV)	E_f (keV)	Comment
2175.3	0.47 ^{c)}	2611.2	435.9	
2196.11(5)	1.90(4)	2631.8	435.9	
2201.7	1.47 ^{c)}	2637.6	435.9	
2468.96(6)	0.64(2)	2631.8	163.0	
2474.76(4)	2.85(4)	2637.6	163.0	
2490.03(4)	1.56(3)	2652.8	163.0	

- a) Numbers in parenthesis are errors and indicate uncertainties in the last significant figures reported.
- b) All intensities are normalized to 163.0-keV line.
- c) Intensity values determined by using peak areas from coincidence spectra.
- [1] Weak peaks ($I_{\gamma} \leq 0.3$).
- [2] Not placed in the decay scheme.

a portion of gamma-ray spectrum. The areas for all the strong peaks in the 30 spectra were extracted from the fits and decay curves were plotted. The half-lives of these strong transitions were then determined by fitting the natural logarithm of the areas against time. Table 4-2 lists the half-lives of the strong gamma transitions in the decay of $^{184}\text{Au} \rightarrow ^{184}\text{Pt}$, and Table 4-3 lists the half-lives of some of the conversion electrons in the decay. It should be noted that for conversion electron spectra only a few isolated peaks could be fitted with SAM due to the poor resolution of electron detector, and the fits were normally not very good. The decay curves for some of the prominent gamma transitions and conversion electrons are shown in Fig. 4-4 and Fig. 4-5, respectively.

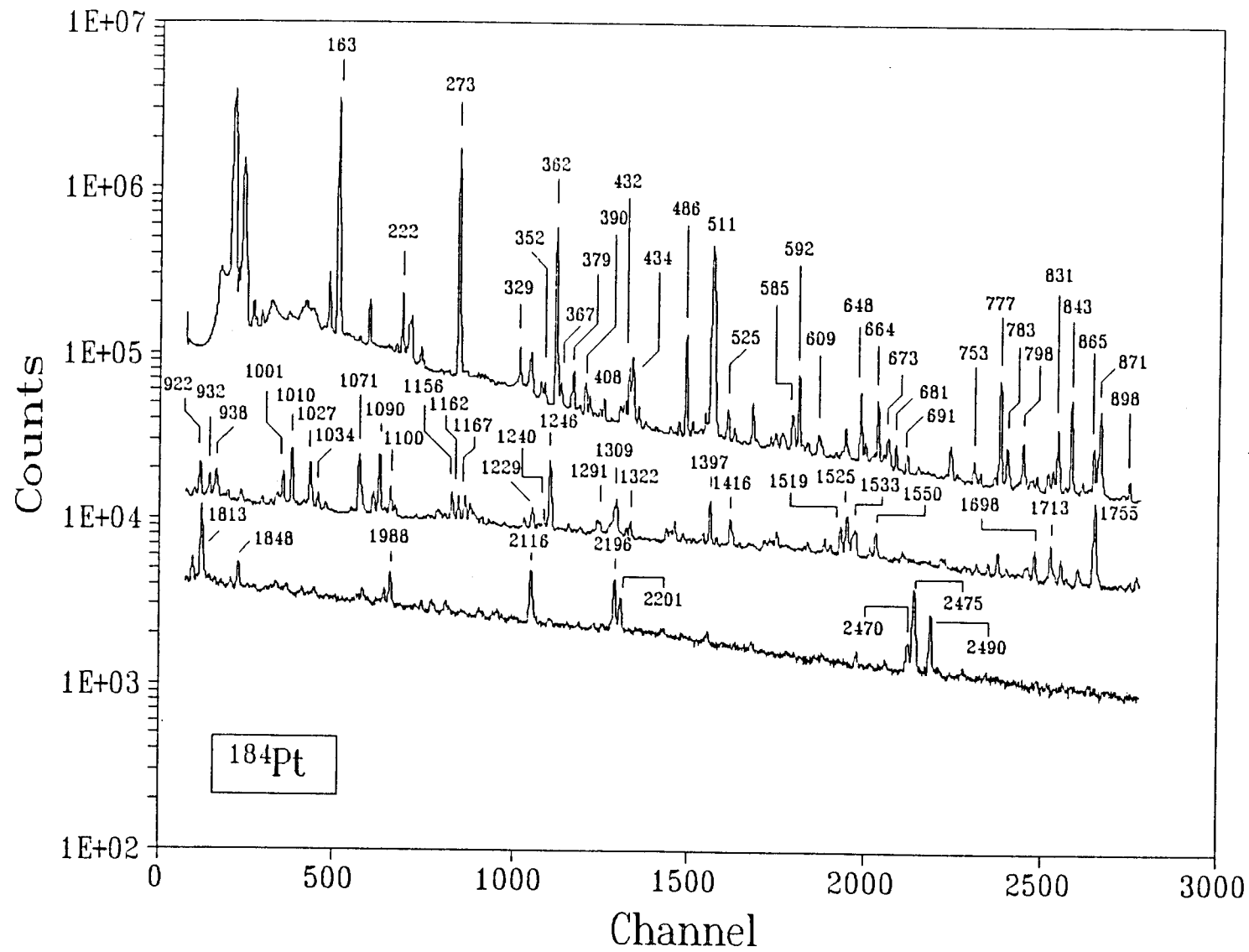


Fig. 4-1 Gamma-ray singles spectrum of ^{184}Pt .

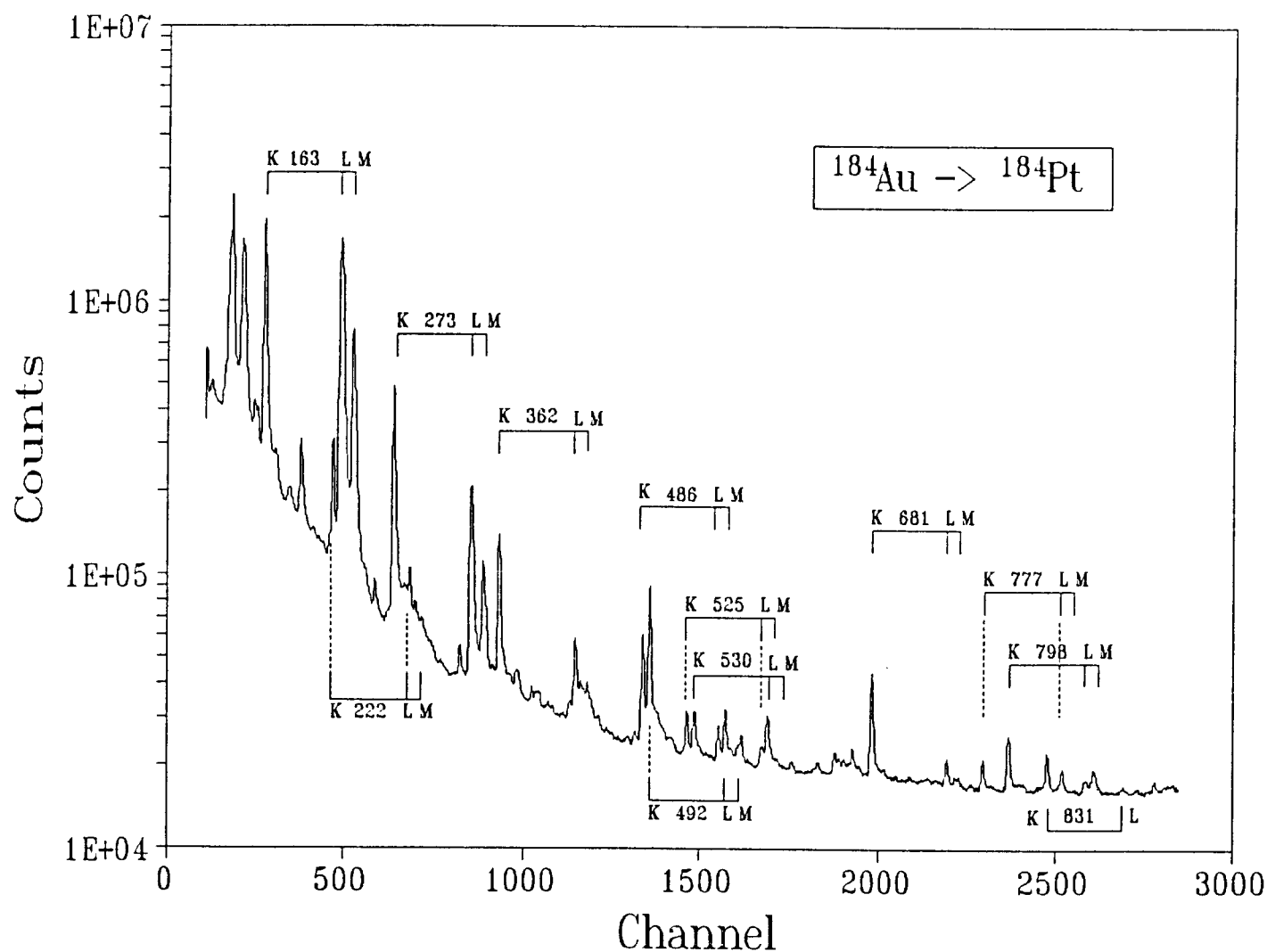


Fig. 4-2 The conversion electron spectrum of ^{184}Pt .

DET 1.SPK

20-OCT-91 22:00:36

1 0.74

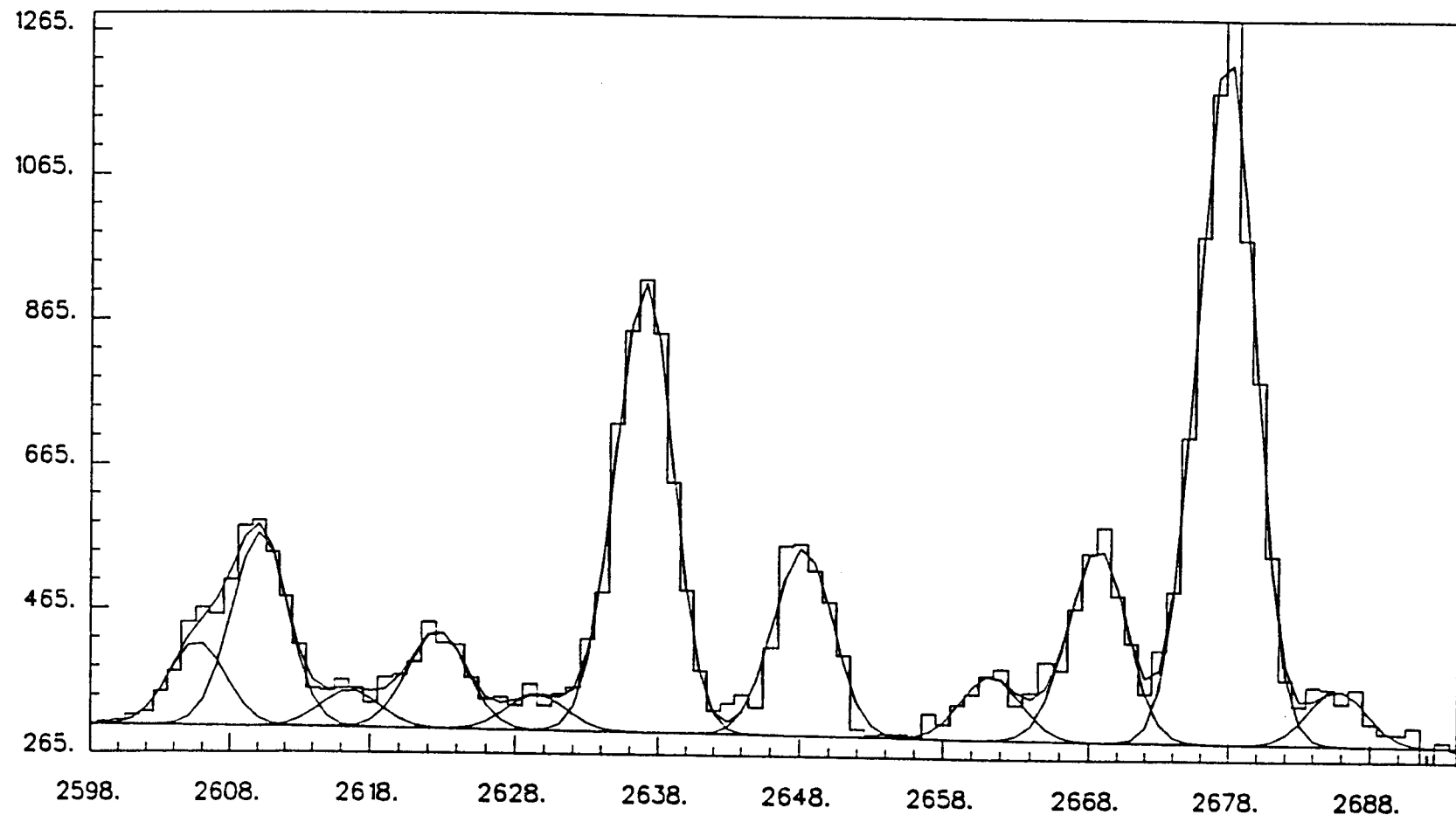


Fig. 4-3 Typical SAM fitting curve for a portion of gamma-ray spectrum.

Table 4-2 A compilation of half-lives of strong gamma transitions in ^{184}Pt .

E_{γ} (keV)	$T_{1/2}$ (sec)	E_{γ} (keV)	$T_{1/2}$ (sec)
163.0	61.6 ± 0.9	843.9	70.9 ± 1.7
221.9	53.1 ± 0.9	864.9	56.5 ± 1.6
272.9	56.5 ± 0.6	871.0 ^g	53.4 ± 1.0
328.8 ^a	88.1 ± 3.5	898.8	54.1 ± 3.2
352.1	65.8 ± 2.8	923.4	57.0 ± 2.1
362.3	52.9 ± 0.6	932.3	52.2 ± 2.6
367.2	51.4 ± 2.0	938.7 ^h	54.9 ± 2.3
377.0	54.7 ± 2.4	1001.5	55.5 ± 2.2
379.1	57.9 ± 1.8	1009.6	73.2 ± 2.7
390.4 ^b	60.6 ± 2.0	1026.5	52.4 ± 1.6
404.4	52.8 ± 3.2	1071.3	64.8 ± 2.1
408.1	75.0 ± 3.8	1084.7	56.7 ± 4.3
432.2	52.0 ± 0.9	1090.2	51.2 ± 1.1
441.3	52.5 ± 2.2	1100.4	51.8 ± 2.4
479.0	46.9 ± 1.9	1155.7	54.0 ± 3.3
485.7	66.6 ± 1.2	1161.6	56.9 ± 4.9
491.7	46.2 ± 2.7	1167.7	66.4 ± 6.3
525.2	47.5 ± 1.0	1229.4	52.4 ± 3.2
531.1 ^c	86.9 ± 10.4	1239.7	61.7 ± 4.1
591.9	54.5 ± 1.0	1245.9 ⁱ	54.4 ± 0.8
648.7	66.2 ± 1.6	1397.4	69.2 ± 3.5
664.2	54.1 ± 1.2	1416.2	56.3 ± 3.6
680.9 ^d	79.4 ± 4.9	1519.1	63.9 ± 5.8
753.0 ^e	51.9 ± 1.6	1524.9	55.6 ± 2.7
776.8	66.2 ± 1.4	1550.8	81.4 ± 6.1
783.0 ^f	55.1 ± 3.2	1663.2	70.2 ± 10.5
798.4	61.9 ± 2.0	1697.9	76.3 ± 9.1
831.1	53.3 ± 1.1	1713.1	78.7 ± 4.8

Table 4-2 (continued)

E_{γ} (keV)	$T_{1/2}$ (sec)	E_{γ} (keV)	$T_{1/2}$ (sec)
1722.4	62.4 ± 5.9	2196.1	70.8 ± 4.0
1754.6	53.6 ± 1.0	2201.7	65.1 ± 4.6
1813.4	53.9 ± 1.3	2474.8	72.4 ± 2.3
1989.0	90.0 ± 11.8	2490.0	84.3 ± 5.7
2117.0	54.9 ± 2.7		
a. Doublet, transitions of $1173 \rightarrow 844$ and $492 \rightarrow 163$.			
b. Doublet, transitions of $2331 \rightarrow 1954$ and $1234 \rightarrow 844$.			
c. Doublet, transitions of $1470 \rightarrow 940$ (pure E0) and $2331 \rightarrow 1800$.			
d. Doublet, transitions of $1173 \rightarrow 492$ and $844 \rightarrow 163$.			
e. Triplet, transitions of $1693 \rightarrow 940$, $2553 \rightarrow 1800$ and $1597 \rightarrow 844$.			
f. Doublet, transitions of $2302 \rightarrow 1519$ and $1431 \rightarrow 649$.			
g. Doublet, transitions of $2975 \rightarrow 2105$ and $1307 \rightarrow 436$.			
h. Doublet, transitions of $1736 \rightarrow 798$ and $1968 \rightarrow 1028$.			
i. Doublet, transitions of $2553 \rightarrow 1307$ and $1682 \rightarrow 436$.			

4.3 Coincidence Data Analysis - Determination of Internal Conversion Coefficients

The analysis of singles data can yield relative intensities of the transitions and aid in determining whether a particular transition belongs to the decay of the study. From the results one can also assign some of the transitions to the level scheme by following the Ritz energy sum rule. But for a large number of the peaks in the spectrum the use of coincidence data is the only way to place them in the decay scheme. The coincidence data processing was performed on HHIRF Concurrent 3230

Table 4-3 A compilation of half-lives of strong conversion electrons in ^{184}Pt .

E_e (keV)	$T_{1/2}$ (sec)	E_e (keV)	$T_{1/2}$ (sec)
70.0L ₁₂₃ ^a	94.6 ± 1.6	525.2K	75.6 ± 5.3
70.0M+N ^b	72.6 ± 1.1	530.2K	58.5 ± 3.2
163.0K	63.7 ± 2.0	680.9K	71.8 ± 2.4
272.9K	52.3 ± 0.6	776.8K	65.2 ± 5.5
362.3K	53.3 ± 1.4	776.8L	74.9 ± 8.8
362.3L	53.5 ± 1.4	798.4K	59.7 ± 2.9
485.7K	59.9 ± 2.0	798.4L	74.9 ± 8.8
485.7L	79.0 ± 9.3	831.1K	58.3 ± 3.9
491.9K	58.9 ± 1.4	871.0K	56.8 ± 7.1
491.9L	65.1 ± 4.5		

a, b. Peaks are too close to be resolved.

computer system, using the high level Comprehensive HIistograming Language (CHIL)[Mil85]. This language generates instructions for histograming data (on-line) or selecting interesting events for further analysis (off-line). The magnetic tapes containing the event-by-event three-parameter coincidence data were first scanned with CHIL-based tape scan program to create the event matrices consisting of counts of gamma-gamma (or gamma-electron) coincidence pairs falling within a certain time interval. The event matrices were two dimensional with two axes representing energies of gamma-rays (or electrons) from the two detectors in coincidence. Once they were created, gates (energy windows) along one axis could be set, and the projections of the matrices along the other axis would result in spectra representing all events in coincidence with the gates of interest. The gated spectra were then stored for further analysis.

The CHIL codes used to scan the event tapes for this experiment are listed in Appendix B. All the parameters in the scan codes are identical to those used in the event handler program (Appendix A). The scan codes contain instructions to construct

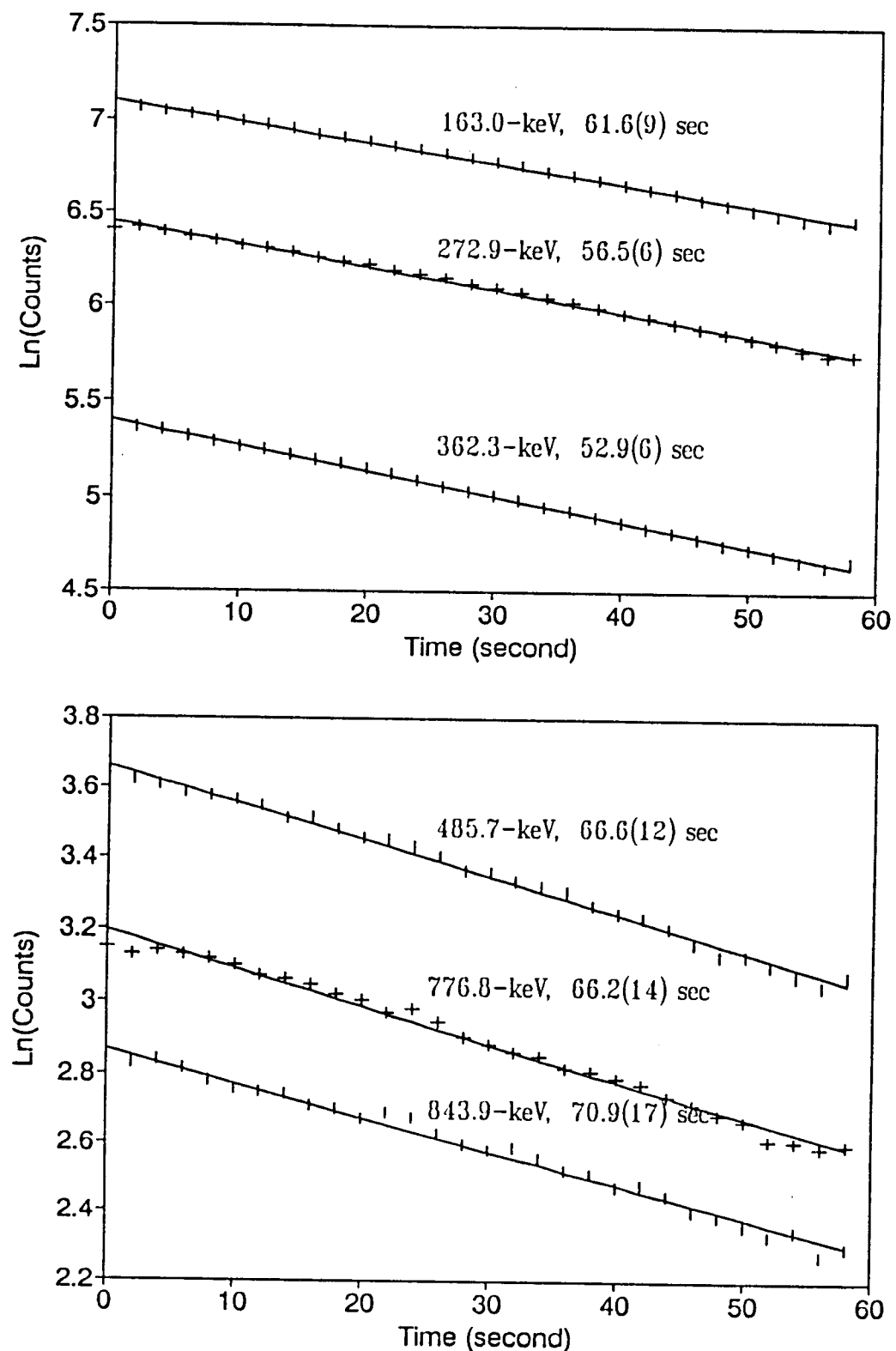


Fig. 4-4 Decay curves of strong gamma transitions in ^{184}Pt .

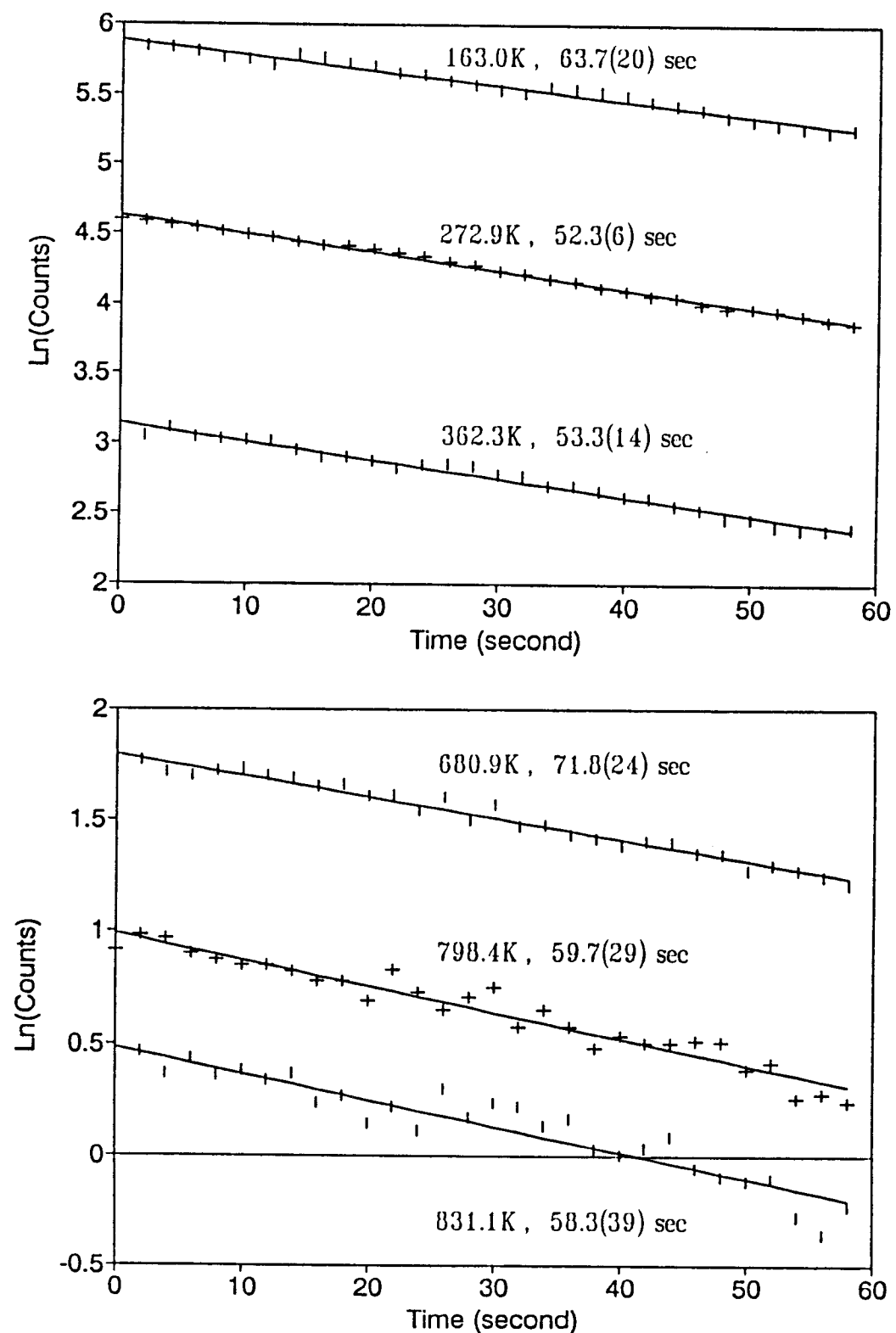


Fig. 4-5 Decay curves of strong conversion electrons in ^{184}Pt .

two-dimensional matrices of 4096x4096 that contain events representing coincidence pairs falling within the chosen time windows. The time windows were set according to the TAC spectra, and they were chosen so that the statistics of true coincidence data could be maximized and random counts in the matrices were kept at the minimum. The last line of the codes contains the definitions of x - and y -axis (e^- as x -axis, gamma as y -axis in the electron-gamma case), the dimension of the matrix (4096) and the TAC spectrum used with the gate set. After the tapes were scanned twice, two matrices or histogram files (e^- - γ and γ - γ) were created.

From the matrices the coincidence relationship among the transitions could be developed by setting energy gates along the x - and y -axes. When a gate for a particular transition was set along one axis, the transitions that are in coincidence with that particular transition were found by projecting the matrices along the other axis. For example, if a gate on a particular gamma-ray was set along the y -axis, the x -axis projections of two matrices would yield the gamma rays and conversion electrons that are in coincidence, respectively. The gated spectra were created using data analysis and manipulation program (DAM) which has the feature for processing 2-D matrices. To determine the actual gate width and position for an individual transition, the total coincidence projections were first looked at, and 1-D spectra were created by gating the full range (4096 channels) along one axis. For each transition, the coincident transitions were found in the following way. A gate was first set by specifying the lower and higher channel covering the full width of the peak, and projection of the matrix was saved into a buffer. To remove the chance coincidences, a background gate with the same number of channels was also set close to the peak, and the projection was subtracted from the buffer, leaving only the true coincidence. The buffer content could be either extracted in the form of sequential spectrum (background-subtracted gated spectrum), or displayed on the screen and copied to a printer. The gated spectra were analyzed interactively by simply viewing the screen-display using program DAM, which turned out to be accurate enough for most of the gates pulled. Automatic fitting programs were also used when necessary. Table 4-4 lists some of the gamma-gamma coincidence relationships that were important in the

Table 4-4 Important gamma-gamma relationships placed in $^{184}\text{Au} \rightarrow ^{184}\text{Pt}$.

Gate (keV)	Coincidences
163.0	S: 273 329 486 777 1010 1072 I: 681 865 1520 1551 2476 W: 1291 1357 1664 1805 1849 2469 2491 D: 1072
221.9	I: 377 479 586 868 1101 W: 391 448 531 600 1024 1303 1533 D: 702 1097 1392 1896
272.9	S: 362 408 504 592 799 871 1246 I: 939 996 1027 1034 1083 1162 1240 1308
1363	1417 2118 W: 213 1390 1505 1738 1894 2196 2202 D: 737 2175
328.8	S: 352 I: 681 W: 157 1293
362.3	S: 432 664 831 I: 932 1001 1085 1156 1755 1813 W: 1142 1456 1533
379.1	I: 486 649
390.4	I: 844 W: 352 408 681
425.3	233 329 525 681 737 1010 1173
432.2	I: 1100 W: 1322
434.8	I: 379 592 865 D: 184 230
485.7	S: 379 I: 291 783

Table 4-4 (continued)

Gate (keV)	Coincidences
485.7	W: 525 586 821 870 949 964 1983 1989 195 D: 805 1065 1176
591.9	I: 435 W: 279 404 570 664 1525 D: 207 772 855 940 1302
776.8	I: 367 W: 294 492 691 753 1698 1713 D: 233 579 1615 1692
831.1	I: 924 D: 702
843.9	I: 390 W: 329 588 609 754 870 D: 184 626 675 839 940 1788
871.0	I: 1246 W: 424 575 1230 D: 1024
932.3	W: 822 D: 601 806
1009.6	W: 281 297 425 D: 346 1459
1026.5	W: 1090 D: 868 1075
1071.3	W: 229 441 565 1398 D: 1097 1419
1084.7	D: 448 670
1090.2	I: 435 664 W: 228 1027
1155.7	W: 377

Table 4-4 (continued)

Gate (keV)	Coincidences
1245.9	W: 279 367 509 871
1309.2	D: 586
1397.4	S: 1072
	W: 207 294 391 586 799
1416.2	W: 479
1713.1	W: 291 504 777

Note: coincidences are identified as S (strong, over 500 coincidence events), I (intermediate, coincidence events range from 100 to 500), W(weak, 25 to 100 coincidences), and D (doubtful, coincidence below 25)

construction of the $^{184}\text{Au} \rightarrow ^{184}\text{Pt}$ decay scheme.

Techniques that are used to extract internal conversion coefficients are discussed extensively by J. H. Hamilton [Ham75]. Since the onset of Ge(Li) detectors, the method that has been used most for ICC measurements in complex decay schemes is the normalized-peak-to-gamma (NPG) method. In this method relative electron and gamma-ray intensities obtained with different detecting instruments are normalized through a known conversion coefficient of a particular transition in the spectrum; this particular transition can be either one of the transitions in the decay scheme of study, or a standard decay from another isotope. If this method is applied for even-even nuclei, the theoretical value of one of the pure E2 transitions in the decay can be used for normalization. In obtaining the conversion coefficients for transitions in a decay scheme, gamma and electron singles spectra should be analyzed using one of the peak-fitting routines, and relative gamma and electron intensities to the pure E2 transition are calculated. For a particular transition the ratio of relative gamma intensity to that of the pure E2 transition multiplied by $\alpha(\text{E}2)$ of the pure E2 transition gives the

conversion coefficient. In the present study, the use of this method was restricted to a few transitions due to the high line density in the electron spectrum. However, the gamma-electron coincidence data provided a way of getting around the unresolved multiplet problem. By gating on a particular gamma-ray and extracting both gamma-ray and electron spectrum, the complex multiplets could be resolved, and the NPG method was applied. Conversion coefficients for some of the important transitions in decay $^{184}\text{Au} \rightarrow ^{184}\text{Pt}$ are presented in Table 8-1. Fig. 4-6 to Fig. 4-8 are some of the gated gamma and electron spectra used in the determination of conversion coefficients.

4.4 Construction of Decay Scheme

The construction of the decay scheme for $^{184}\text{Au} \rightarrow ^{184}\text{Pt}$ (shown in Fig. 4-10) was based on the Ritz energy sum rule and the use of $\gamma\text{-}\gamma\text{-t}$ and $\gamma\text{-e}^-\text{-t}$ coincidence data. We have established 52 energy levels and placed about 180 transitions in the decay scheme. Fig. 4-9 is the decay scheme taken from Nuclear Data Sheet [NDS89]. In comparison with this decay scheme, we have established a large number of energy levels between 1730.6-keV level and 2552.8-keV level. We have added 6_3^+ level at 1800-keV to the excited coexisting band. More importantly we have identified the second set of coexisting bands built on $K^* = 2^+$, which is unprecedented. Strong E0 transitions are found linking states of these two bands (see Fig. 8-1).

4.5 Discussion - Ground State Structure of ^{184}Au

The ground state of ^{184}Au was known to have a half-life of 53 seconds and a spin of 3 before this experiment. The data analysis of pulsed source on-line nuclear orientation at NICOLE [Sto89] suggests the existence of an isomeric state in the ^{184}Au ground state structure. The NICOLE group further concluded that the isomeric state has a half-life of 12 seconds and a spin of 5; and this state lies about 70 keV below the known 53-sec state. The half-life results of strong γ rays and electrons of this experiment also suggests the existence of an isomeric state in ^{184}Au , but a different

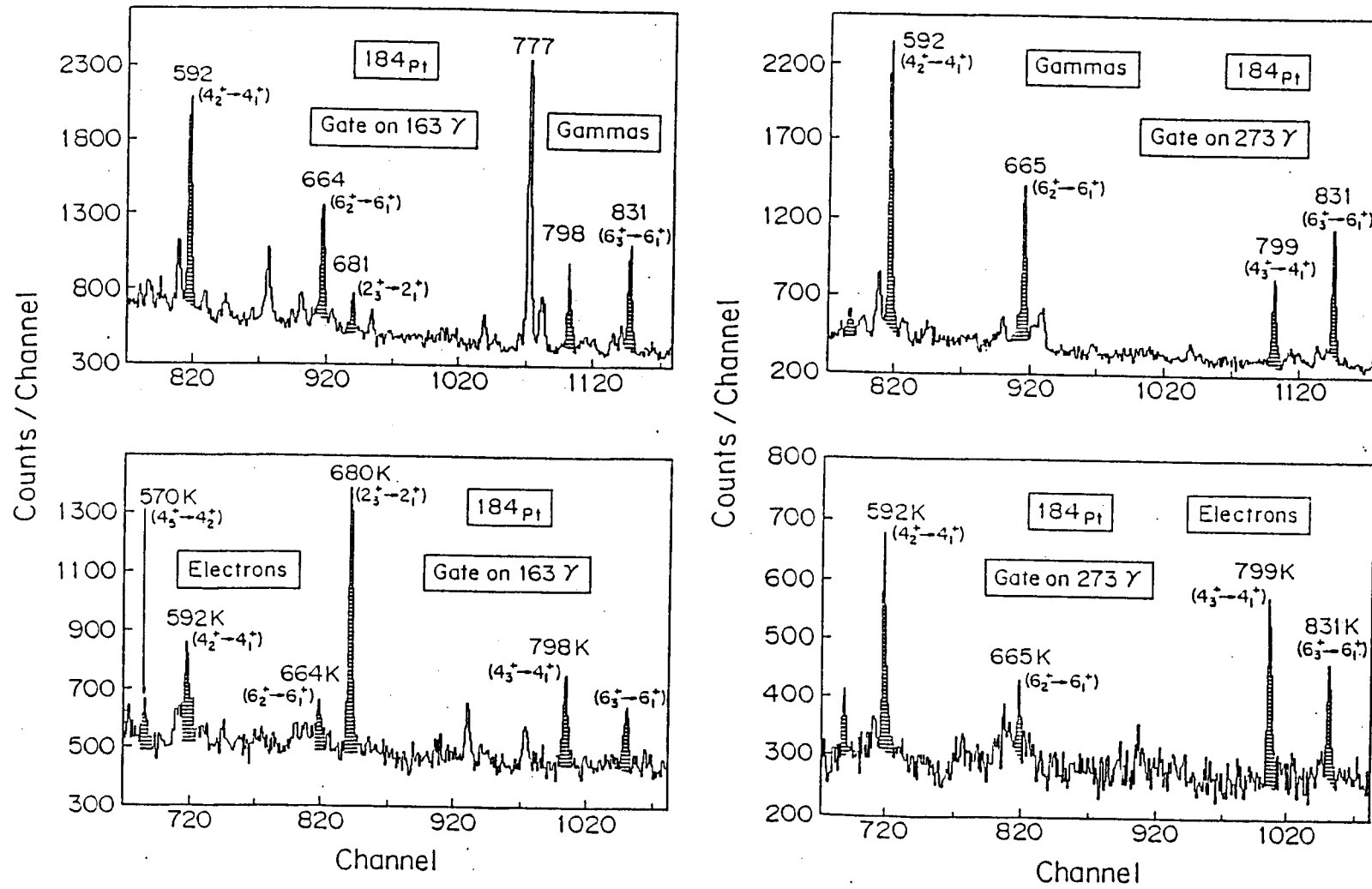


Fig. 4-6 Portions of gamma-ray and electron spectrum gated on 163-keV (left) and 273-keV (right) γ -rays.

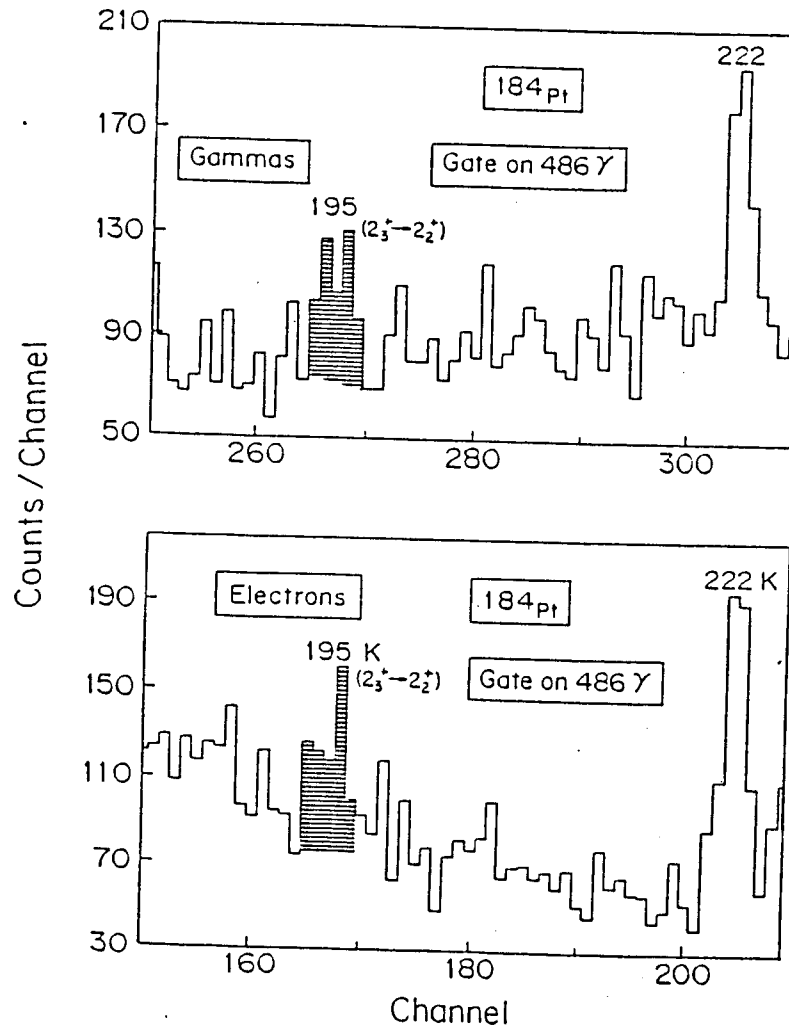
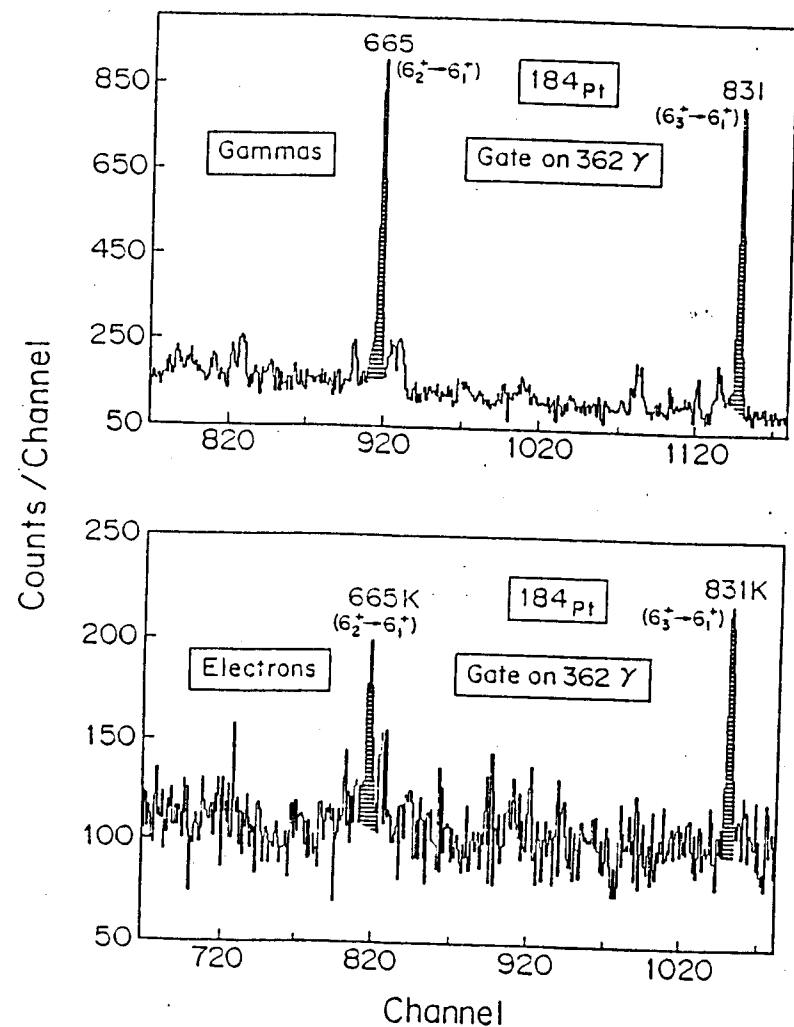


Fig. 4-7 Portions of gamma- and electron-spectrum gated on 362-keV (left) and 486-keV (right) γ -rays.

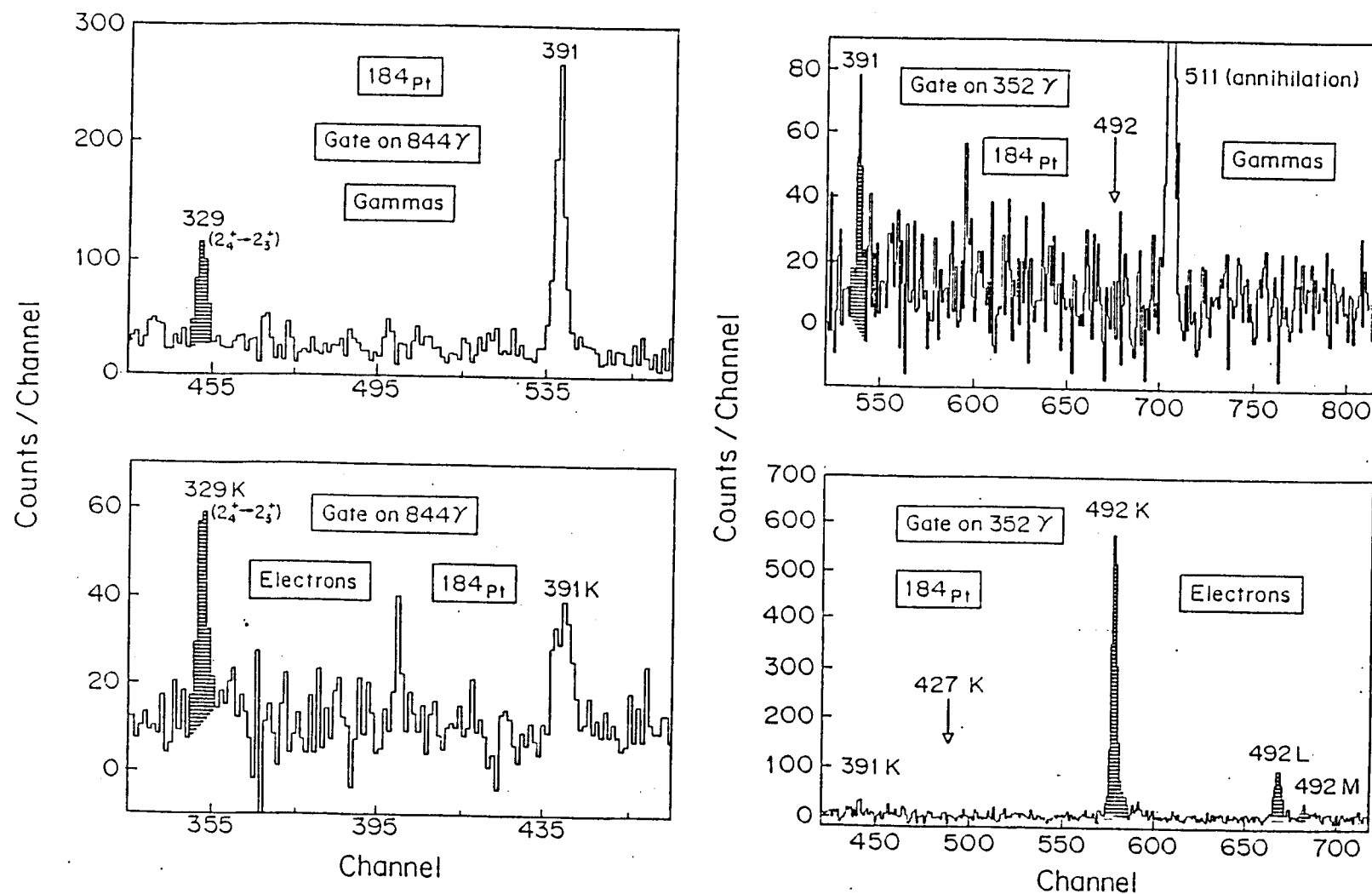


Fig. 4-8 Portions of gamma- and electron-spectrum gated on 844-keV (left) and 352- keV (right) γ -rays.

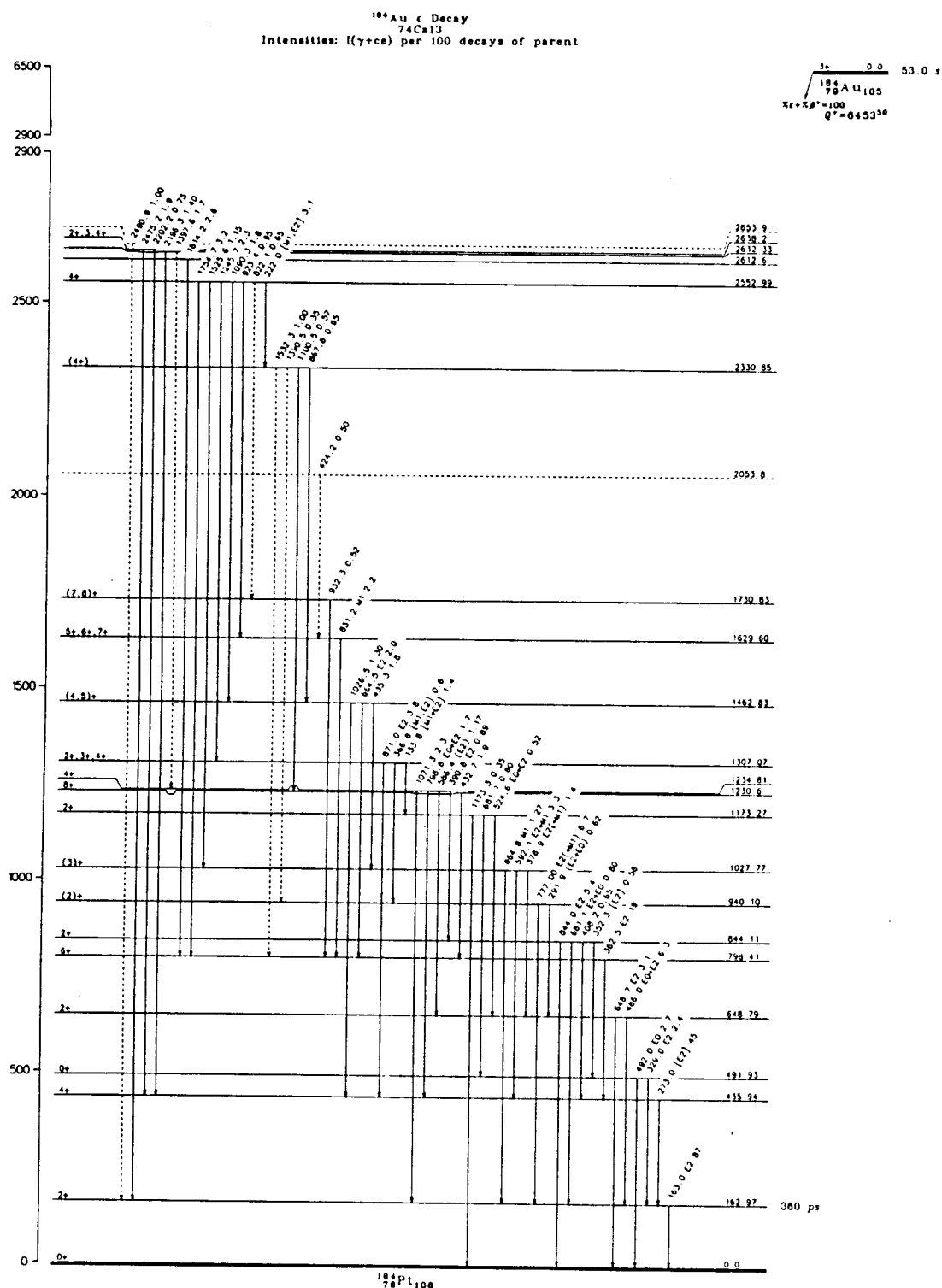


Fig. 4-9 Decay scheme of ¹⁸⁴Pt from Nuclear Data Sheet [NDS89].

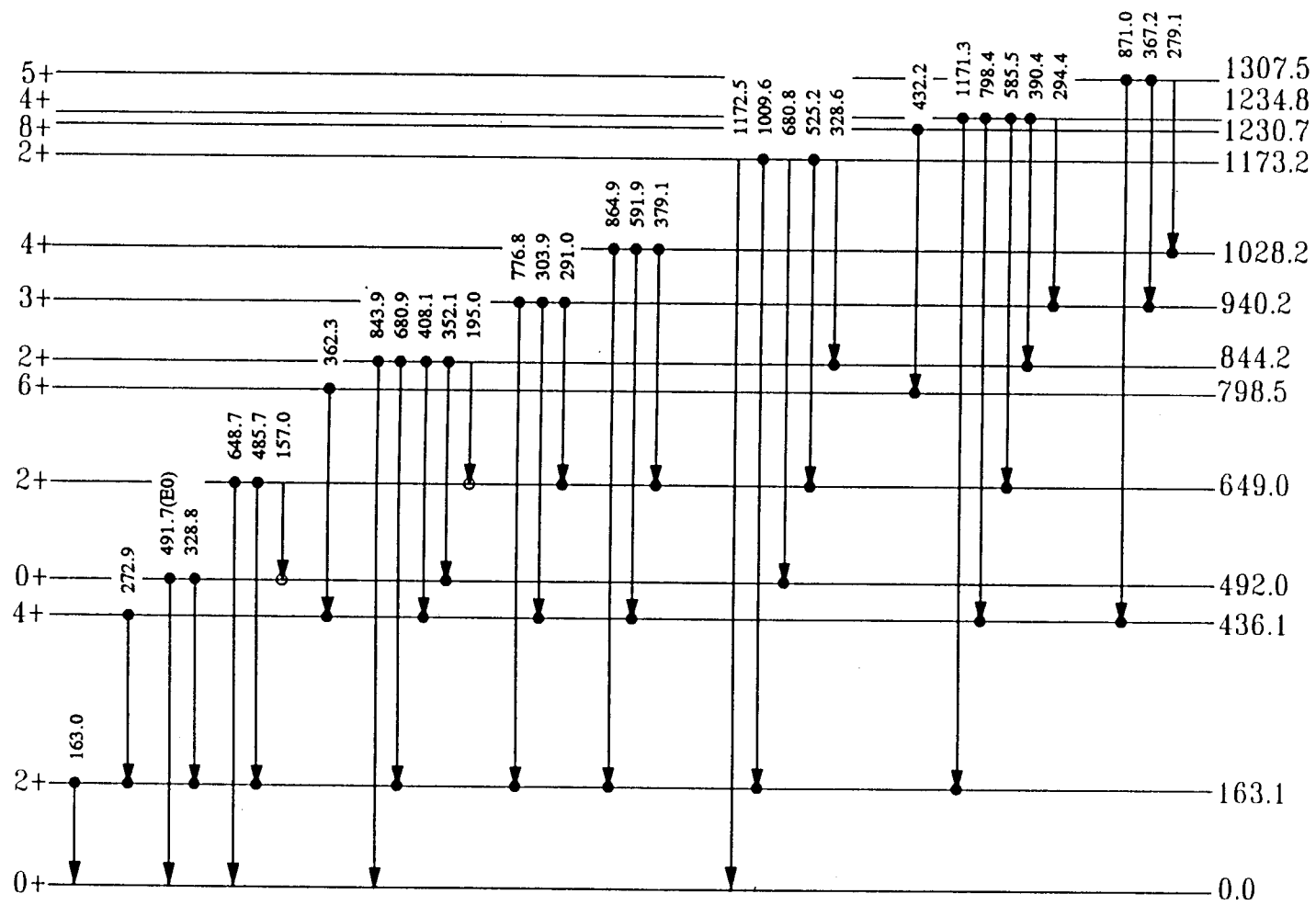


Fig. 4-10 Proposed decay scheme of $^{184}\text{Au} \rightarrow ^{184}\text{Pt}$ (coincidences denoted by ●).

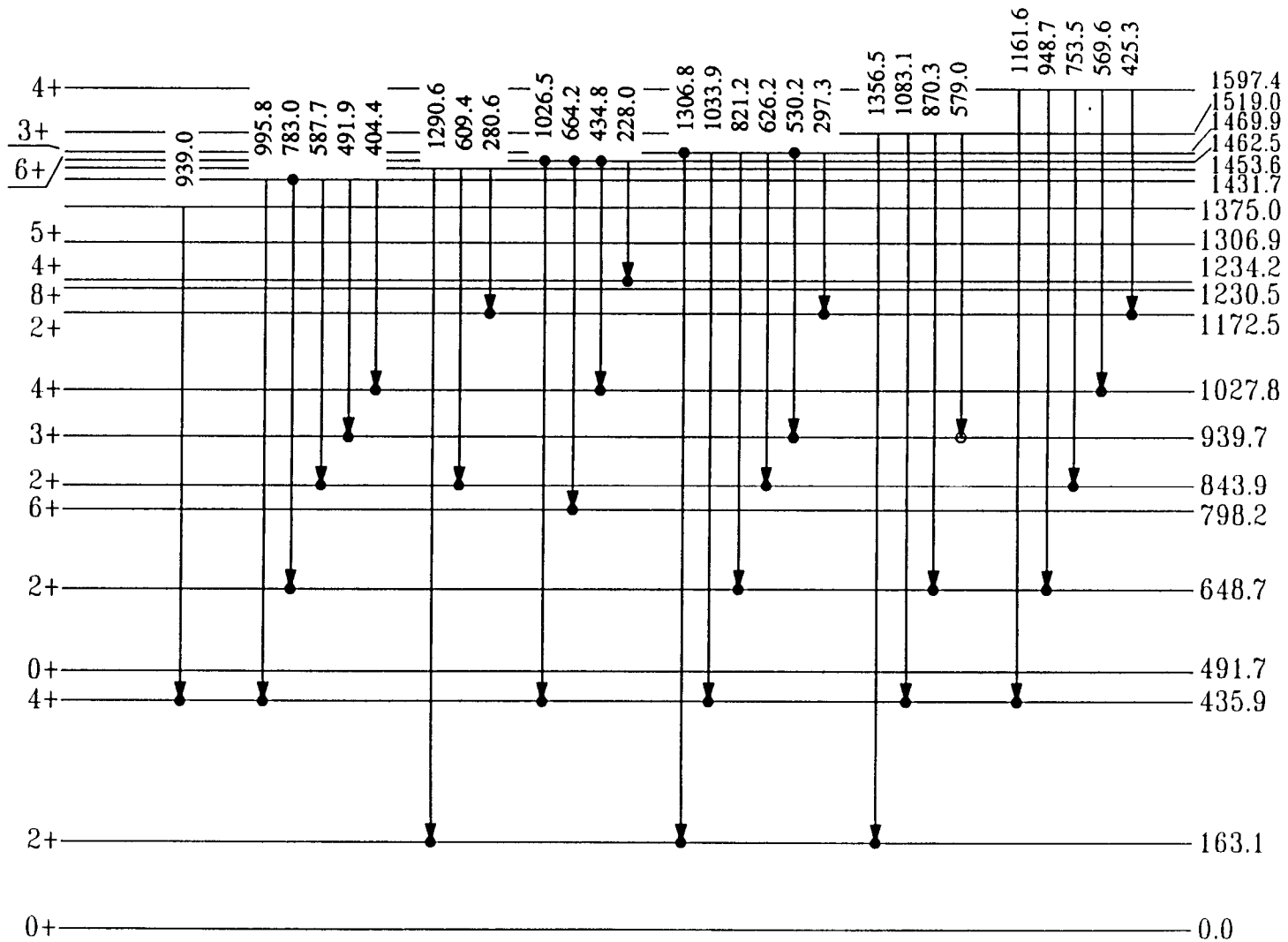


Fig. 4-10 (continued)

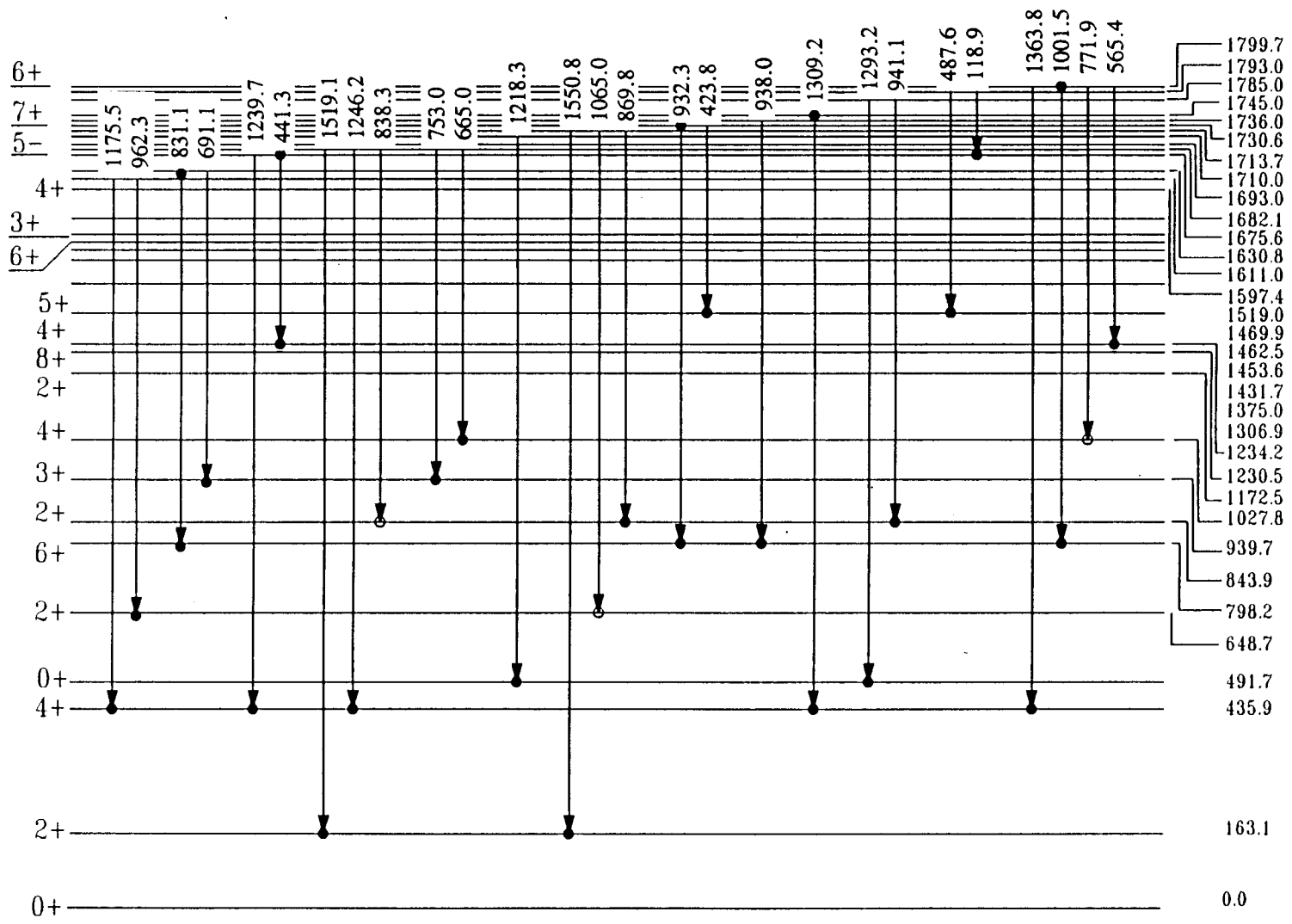


Fig. 4-10 (continued)

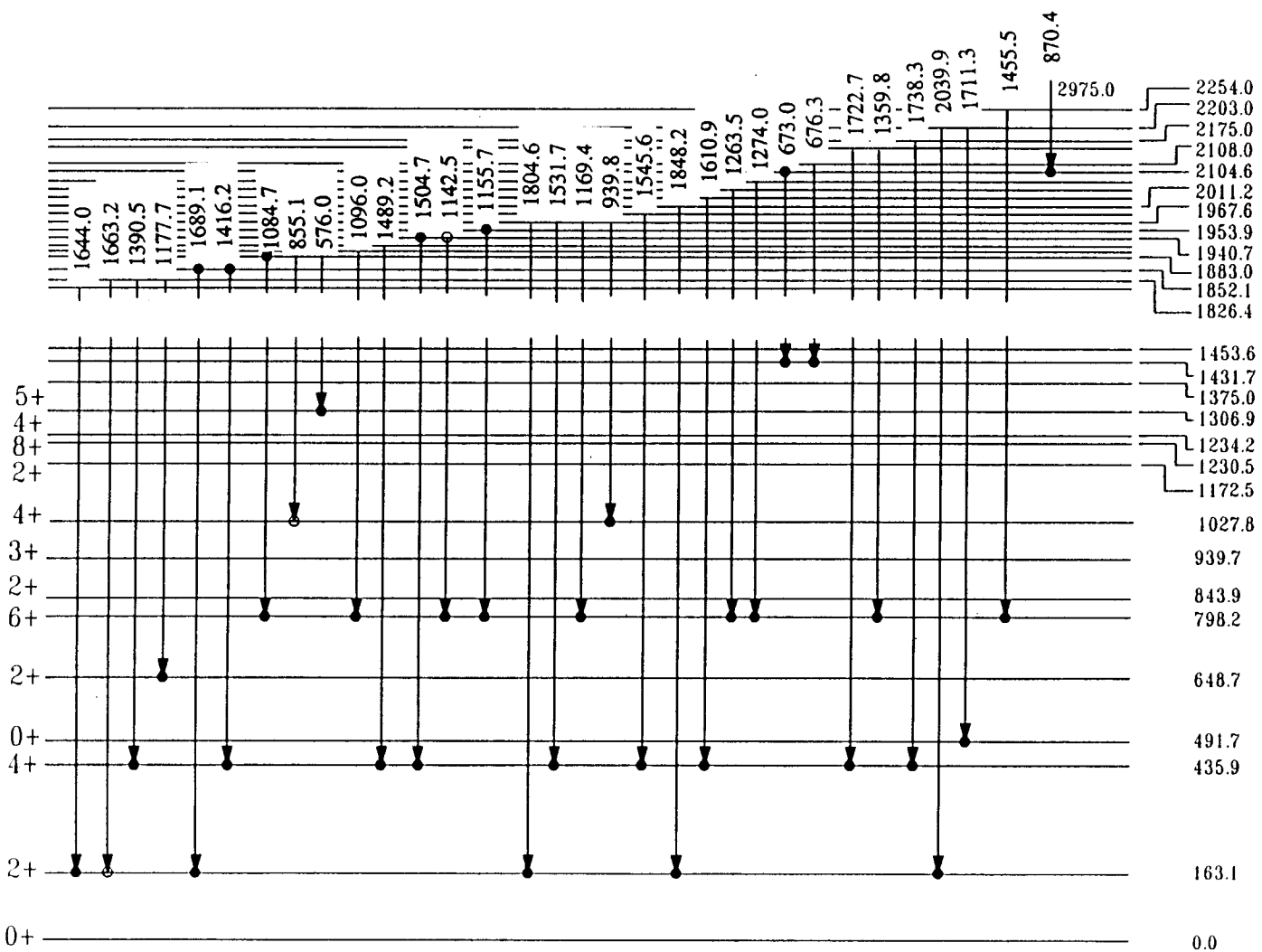


Fig. 4-10 (continued)

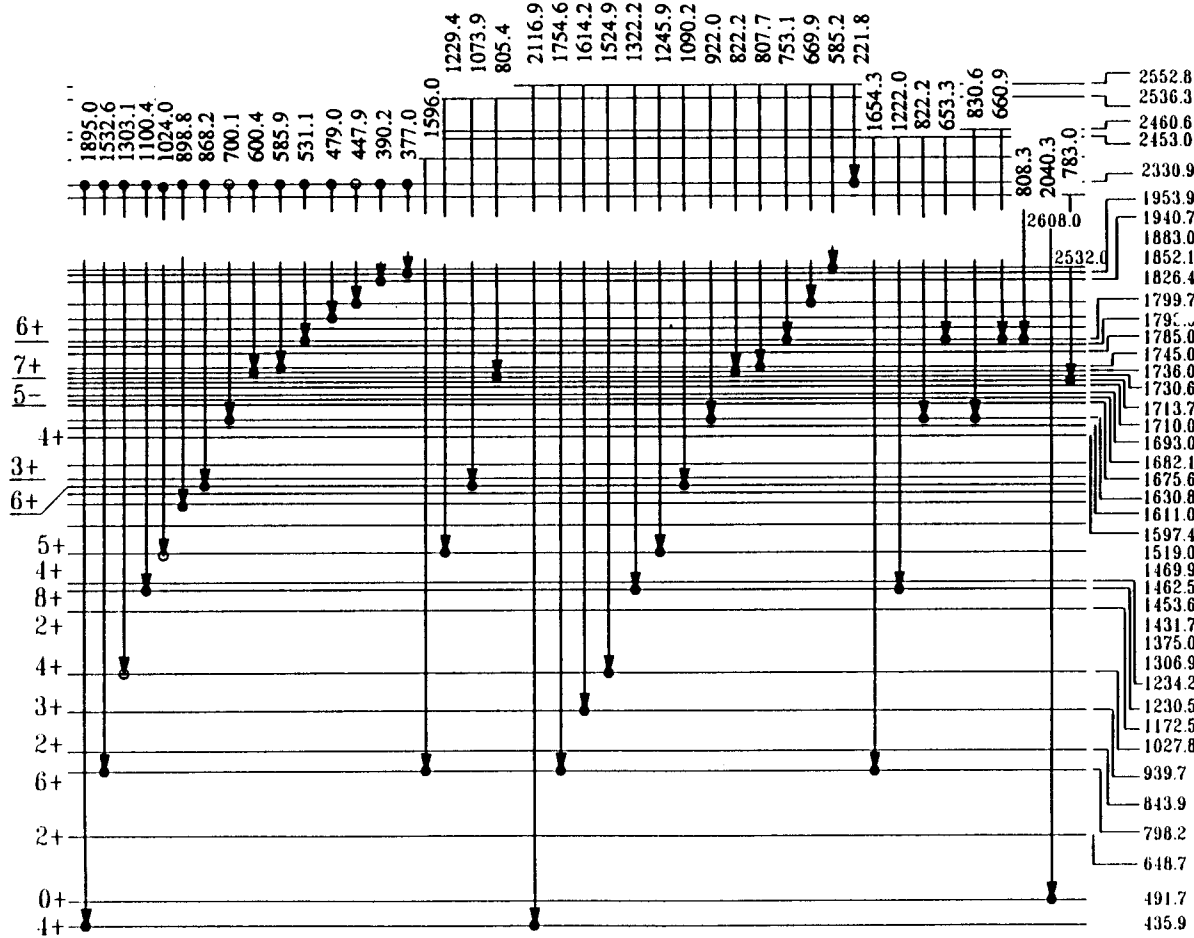


Fig. 4-10 (continued)

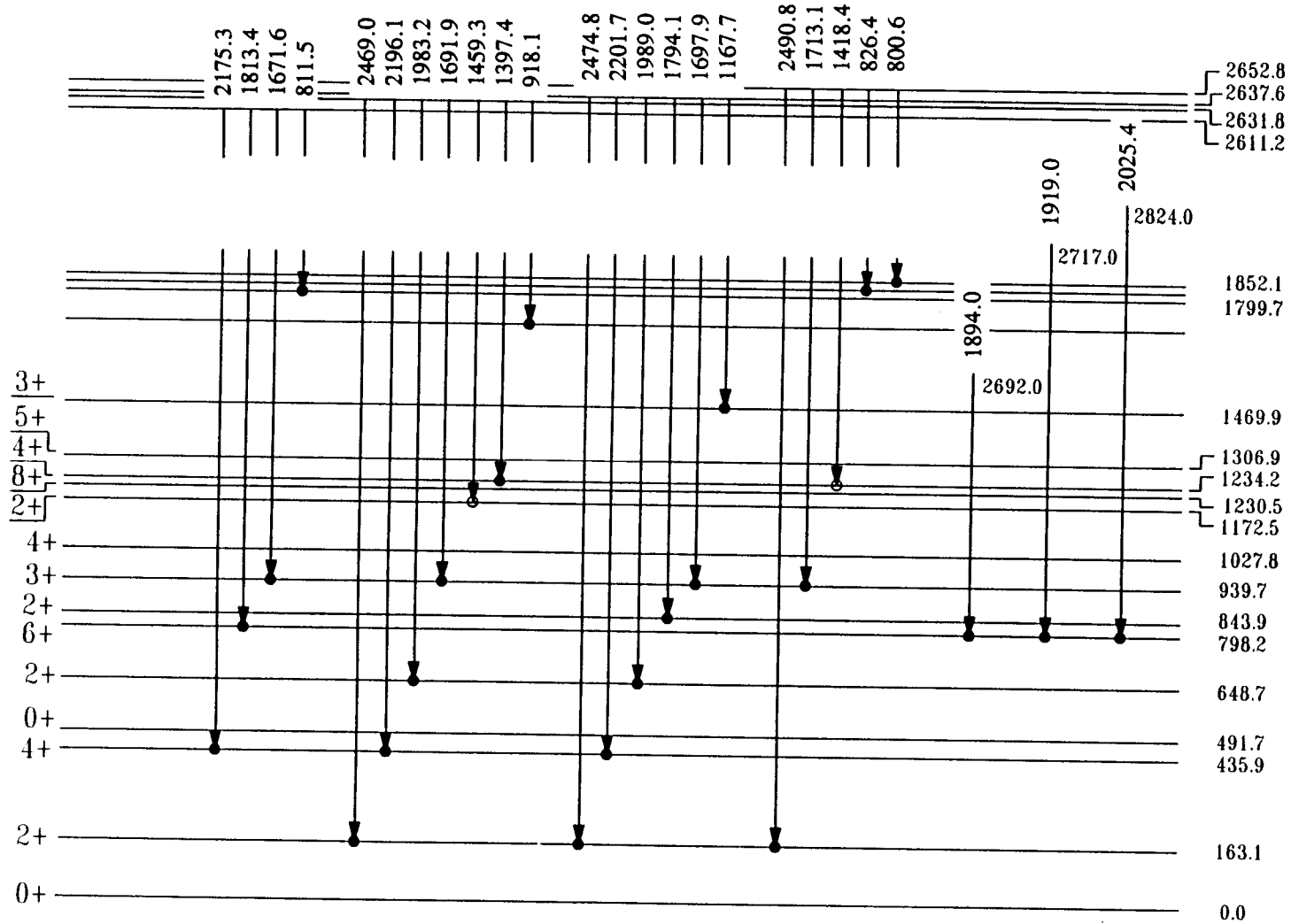


Fig. 4-10 (continued)

picture emerged regarding the half-life of this state. From Table 4-2 and Table 4-3 we can clearly see that there are three sets of half-lives. There is an upper limit of 73 seconds and a lower limit of 53 seconds. There are transitions whose half-lives lie between 56 second to 66 seconds. Most transitions originating from high spin states have a shorter half-life, while the transitions from low spin have a longer half-life. From this evidence we believe that the ground state structure of ^{184}Au consists of (at least) two isomeric states of high and low spin with the half-life of high spin state being 53 seconds, the other being 73 seconds. Both states decay to levels of ^{184}Pt via β^+ with the high spin state mainly populating high spin levels in ^{184}Pt and low spin state of ^{184}Au mainly low spin levels in ^{184}Pt . The middle range half-life occurs to those transitions (e.g. 163-keV, half-life 61.6 sec, $2^+ \rightarrow 0^+$) that originate from low spin levels fed both from direct β^+ decay and from the cascade decay of upper levels. There are other evidences that support this construction.

Table 4-5 contains the intensity balance for some of the levels in the decay of $^{184}\text{Au} \rightarrow ^{184}\text{Pt}$ (I_γ , 163 = 100). From the β^+ feeding pattern and selection rules we can conclude that the spin of the low spin state is either 2^+ or 3^+ and that of the high spin state takes values of either 5^+ or 6^+ . The NICOLE group also reported, based on the Weisskopf estimates, that there might be a highly converted transition of M3 type with energy between 70 keV and 100 keV linking the two isomeric states. One of peaks in our conversion electron spectrum has an energy of 70 keV and a half-life of 73 seconds. If this is the M3 transition linking the two isomeric states, the most likely combinations of two spins are 2,5 or 3,6.

There are also discrepancies in the results of relative γ intensities from different studies. The table below is a comparison of relative intensity data for three strong γ transitions among four studies. Both NICOLE and an old UNISOR test run produced ^{184}Hg to study the decay of $^{184}\text{Au} \rightarrow ^{184}\text{Pt}$; and Cailliau et al. and OSU directly produced ^{184}Au , observing the decay of $^{184}\text{Au} \rightarrow ^{184}\text{Pt}$. Even though there is a discrepancy between Cailliau et al.'s data and our data, the table is a strong indication that by producing ^{184}Au , high spin states became more populated, which is what we expect to see, i.e. nuclear reactions populate higher spin states.

Table 4-5 Intensity balance for levels in $^{184}\text{Au} \rightarrow ^{184}\text{Pt}$ ($I_{\gamma}, 163\text{-keV} = 100$).

Level		I_T in	I_T out	β -feeding
163	2+	160	178	18
436	4+	94	102	8
492	0+	2.8	5.6	2.8
649	2+	11	19	8
798	6+	32	44	12
844	2+	7	14	7
940	3+	10	15	5
1028	4+	11	13	2
1173	2+	2.3	7.1	5
1230	8+	3.0	4.2	1.2
1234	4+	4.8	11.2	6.4
1307	5+	2.7	10.5	7.8
1432	4+	2.1	4.1	2.0
1454		0	1.6	1.6
1462	6+	7	11	4
1470	3+	1.4	4.0	2.6
1519		0	2.5	2.5
1597		0	3.1	3.1
1613		0	0.4	0.4
1630	(6+)	3	5	2
1631		0	1.1	1.1
1676	5-	2	2.1	0.1
1683		0	7.2	7.2
1714		0.4	2.0	1.6
1731	7+	1.1	1.9	0.8

Table 4-6 Comparison of relative intensities.

Ref. Source	Cailliau	NICOLE	UNISOR TEST	OSU
Decay Mode	Au → Pt	Hg→Au→Pt	Hg→Au→Pt	Au→Pt
163-keV	100	100	100	100
273-keV	79	51	54	90
362-keV	35	21	20	40

Another experiment has been scheduled this summer to study spectroscopy of the decay of $^{184}\text{Hg} \rightarrow ^{184}\text{Au}$ at UNISOR. We hope that the ground state structure of ^{184}Au can be clarified and the decay of $^{184}\text{Au} \rightarrow ^{184}\text{Pt}$ can be further understood.

Chapter 5. Theory of the Method - Nuclear Orientation

The detailed description of low-temperature nuclear orientation, general formalism, technique and the various aspects of application, can be found in the book edited by Stone and Postma [Sto86]. In the following section a simplified version of the theory of the method will be given, followed by a brief summary of general formalism of nuclear orientation and a brief discussion about the extraction of information on nuclear properties.

5.1 A Simplified Picture

The principle of the method of low temperature nuclear orientation can be simply illustrated in Fig. 5-1 by a simple dipole transition ($I=1$ to $I=0$). The emission probability for any nuclear transition depends on the angle between the initial nuclear

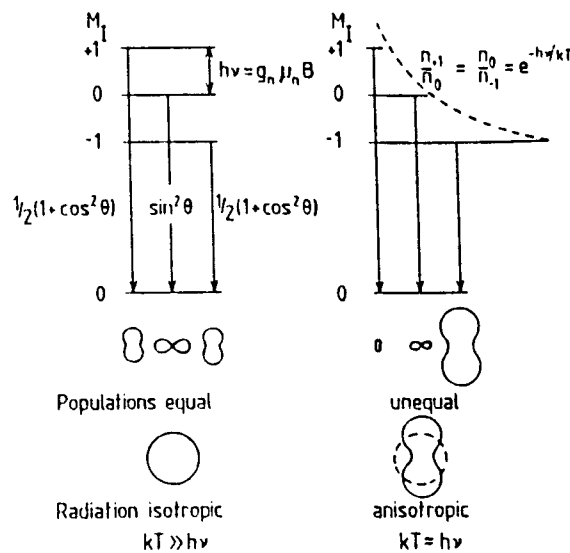


Fig. 5-1 The illustration of the effect of nuclear orientation for a dipole transition [Gel83].

spin and the direction of emission detection. When we average all directions with equal weight only isotropic radiation can be observed. As shown in the figure, when an external field \mathbf{B} is applied, the nuclear state with $I=1$ splits into three substates with $m=0$ and $m=\pm 1$. The angular patterns for transitions from these three substates to the ground level are different ($\sin^2\theta$ for $m=0$, and $(1+\cos^2\theta)/2$ for $m=\pm 1$). Since we can not distinguish among these three transitions even with detectors of the best resolution, what we observe at room temperature is the mixture of transitions equally from three substates. The radiation is isotropic. As the temperature approaches the limit so that $kT \approx \Delta E$, the energy splitting, the populations of substates are made unequal due to the Boltzmann distribution, $\exp(-\Delta E/kT)$, and appreciable ordering of states appears. As a result the directional distribution of the radiation becomes anisotropic.

5.2 General Formalism of Nuclear Orientation

The angular distribution of radiation emitted from oriented nuclei was discussed comprehensively by Steffen and Alder [Ste75], and the angular distribution function W for radiation X emitted from a state of spin I_0 can be expressed in the following equation:

$$W(k, Q) = \frac{d\Omega}{4\pi} \sum_{\lambda q q'} \rho_q^\lambda A_{\lambda q'}(X; Q) D_{qq'}^{(\lambda)}(e_z \rightarrow kx') \quad (38)$$

where the statistical tensors ρ_q^λ describe the orientation of the nuclear state and $A_{\lambda q'}(X, Q)$ is called the angular distribution coefficient, describing the properties of the emitted radiation. The D -function transforms from the quantization axis of the ensemble of nuclear spins to the lab coordinate system, and it can be reduced to the spherical harmonics $Y_{\lambda q}(\theta, \phi)$ if the polarization of the radiation is not measured. The angular distribution becomes the directional distribution without the measurement of radiation polarization.

For axially symmetric orientation of the initial nuclear state, the formula of

directional distribution of radiation is further simplified as in the equation below:

$$W(\theta) = \sum_{\lambda} B_{\lambda}(I_0) A_{\lambda}(X) P_{\lambda}(\cos \theta) , \quad (39)$$

where θ is the angle between the orientation axis and direction in which the radiation is detected, and $P_{\lambda}(\cos \theta)$ are the Legendre polynomials.

There are two correction factors that need to be added to equation 39. Some transitions that occur before the transition of interest may lead to reorientation of nuclear state. This reorientation effect can be accounted for by adding a deorientation coefficient U_{λ} in the equation. A geometrical correction Q_{λ} factor has also to be included to account for the effect due to the finite size of detector and radiation source as well. In practice the distribution function takes the following form:

$$W(\theta) = \sum_{\lambda} Q_{\lambda} B_{\lambda} U_{\lambda} A_{\lambda} P_{\lambda}(\cos \theta) . \quad (40)$$

The orientation of the nuclear ensemble is achieved through the interaction of the external field with either the magnetic dipole moment or electric quadrupole moment, depending on the actual field being applied. The orientation parameters B_{λ} are commonly used to describe the degree of the orientation of nuclear states. They are related to the statistical tensors which, in turn are related to the density matrix of the oriented states, as shown in the following equations:

$$\rho_q^{\lambda}(I_0) = (\hat{I}_0)^{-1} B_{\lambda}(I_0) \delta_{q0} , \quad (41)$$

and

$$\rho_q^{\lambda}(I_0) = \hat{\lambda} \sum_m (-1)^{l_0+m'} \begin{Bmatrix} l_0 & l_0 & \lambda \\ -m' & m & q \end{Bmatrix} \langle I_0 m | \rho | I_0 m' \rangle , \quad (42)$$

where $\begin{Bmatrix} l_0 & l_0 & \lambda \\ -m' & m & q \end{Bmatrix}$ is a Wigner 3-j symbol and the density matrix $\langle I_0 m | \rho | I_0 m' \rangle$

describes the oriented ensemble, which can be constructed once the interaction of nuclei with the environment is known. If the Hamiltonian is diagonal in the basis representation $|I_0m\rangle$, the elements of the density matrix takes the following simple form in thermal equilibrium:

$$\langle I_0m | \rho | I_0m' \rangle = p(m) \delta_{mm'} , \quad (43)$$

where $p(m)$ are called the population parameters and are given by:

$$p(m) = \text{Const.} : e^{E(m)/kT} , \quad (44)$$

where $E(m)$ are the energies of the nuclear substates.

The representation of the orientation parameters can be given by combining equations 41, 42, 43:

$$B_\lambda(I_0) = [(2I_0+1)(2\lambda+1)]^{1/2} \sum_m (-1)^{I_0+m} \begin{pmatrix} I_0 & I_0 & \lambda \\ -m & m & 0 \end{pmatrix} p(m) , \quad (45)$$

and $B_\lambda = 0$ for $\lambda > 2I_0$.

In the low temperature nuclear orientation, the energy sublevel splitting is achieved by the application of either a magnetic field or electric field gradient, using the magnetic dipole interaction and electric quadrupole interaction respectively. In all UNISOR experiments, the magnetic dipole interaction has been used. The superconducting magnet provides the external magnetic field which in turn polarized the ferromagnetic hosts, making use of the hyperfine interaction. The interaction Hamiltonian and the energy of substates in choosing $|I_0m\rangle$ as basis states are expressed as:

$$H = -\mu B , \text{ and } E(m) = -gmB_z , \quad (46)$$

where $g = \mu/I_0$ is the nuclear g-factor.

The interaction of the nuclear magnetic dipole moment with the magnetic field removes the m-degeneracy of nuclear states and thus causes the ordering of substates due to Boltzmann distribution. The population of energy sublevels is then given by:

$$p(m) = \langle I_0 m | I_0 m \rangle = \frac{e^{m\Delta_M/T}}{\sum_m e^{m\Delta_M/T}}, \quad (47)$$

$$\Delta_M = \frac{gB_z}{kI_0}, \text{ with } \Delta_M(\text{mK}) = 0.366 \frac{\mu(\mu_N)B_z(\text{Tesla})}{I_0}, \quad (48)$$

and $B_\lambda(I_0)$ will be given by equation 45 with population parameters from equation 47. In order to achieve a sizable degree of orientation, Δ_M and T need to be of the same order. If $g = 0.5$, and $B = 30$ Tesla, we have $\Delta_M = 5.49$ mK. B_λ values are very sensitive to the change of Δ_M/T , and at high temperature B_λ are proportional to $(\Delta_M/T)^\lambda$.

The nuclear ensemble is said to be oriented if $p(m) \neq p(m')$, and it is said to be aligned if $p(m) = p(-m)$, and polarized if $p(m) \neq p(-m)$. For magnetic dipole interaction, since $p(m) \neq p(-m)$, the nuclear ensemble is polarized. B_λ are non-zero both for even and odd λ . In the case of electric quadrupole interaction, $p(m) = p(-m)$, the nuclear ensemble is aligned and B_λ are non-zero only for even λ values.

The deorientation U_λ coefficients are used to account for the effect of unobserved transitions between the level of orientation and the level from which the observed transition originates. The effect of those transitions is to reduce the degree of orientation of the level of interest, and the deorientation coefficients have values always smaller than or equal to 1. They depend on the spins of all intermediate levels and multipolarities of all unobserved transitions as well as the relative intensities of multipole components. The general expression is given by Steffen [Ste71]:

$$U(I_1, I_2) = \frac{\sum_L U_\lambda(I_1, I_2, L) |\langle I_2 \| L \| I_1 \rangle|^2}{\sum_L |\langle I_2 \| L \| I_1 \rangle|^2}, \quad (49)$$

with the deorientation coefficient for each multipolarity L being expressed as:

If there is a cascade of transitions between the level of orientation and the level from which the transition of interest originates, the deorientation coefficient can be

$$U_\lambda(I_1, I_2, L) = (-1)^{I_1+I_2+L+\lambda} [(2I_1+1)(2I_2+1)]^{1/2} \begin{Bmatrix} I_1 & I_1 & \lambda \\ I_2 & I_2 & L \end{Bmatrix} . \quad (50)$$

computed from the top down on a state-by-state basis, and the effective values is the product of all individual coefficients.

The distribution coefficients A_λ describe the properties of the observed radiation. They depend on the multipole character of the radiation and on the spins of the initial and final states. The character of the multipole radiation (E or M) is determined by the relative parities of the nuclear states. For radiation emitted from initial state of spin I_i and parity π_i to final state of spin I_f and parity π_f , the quantum number of angular momentum it carries satisfies the following relationship with I_i and I_f : $|I_i - I_f| \leq L \leq I_i + I_f$, and the parity of the radiation is the product of π_i and π_f : $\Delta\pi = \pi_i\pi_f$. A transition with a particular L is an electric multipole if $\Delta\pi = (-1)^L$ or a magnetic multipole if $\Delta\pi = (-1)^{L+1}$. In general, most transitions are mixtures of electric and magnetic multipoles with the lowest one or two multipole orders contributing, i.e. either $E(L) + M(L')$ or $M(L) + E(L')$ depending on the parity change. The relative amplitude of two transitions with different multipole order is called multipole mixing ratio, and is defined as:

$$\delta = \frac{\langle I_f \| L' \| I_i \rangle}{\langle I_f \| L \| I_i \rangle} , \quad (51)$$

where $L' = L + 1$.

With the mutipole order of transitions discussed and mixing ratio defined in the above equation, the directional distribution coefficients are given by

$$A_\lambda(\gamma) = \frac{F_\lambda(LLI_i) + 2\delta F_\lambda(LL'I_i) + \delta^2 F_\lambda(L'L'I_i)}{1 + \delta^2} \quad (52)$$

where F_λ are called F -coefficients and defined as

$$F_\lambda(LL'I_fI_i) = (-1)^{I_i+I_f+1} \hat{\lambda} \hat{L} \hat{L}' \hat{I}_i \begin{bmatrix} L & L' & \lambda \\ 1 & -1 & 0 \end{bmatrix} \begin{bmatrix} L & L' & \lambda \\ I_i & I_i & I_f \end{bmatrix}, \quad (53)$$

and the tables of F -coefficients for spins I_i up to 8 and multipolarity up to 3 are given by [Kra71].

It should be pointed out that the directional distribution coefficients given by equation 52 are non-zero only when $\lambda =$ even due to the assumption of parity invariance; thus only the even- λ terms occur in the directional distribution function $W(\theta)$.

The solid angle correction factors Q_λ are not related to the properties of the nuclear ensemble under study. Due to the finite solid angle subtended by detector and source, the observed directional distribution differs from that of "point" source with detector. Normally the effect due to the finite detector is more severe, and only one correction is applied. The solid angle correction factors for coaxial Ge(Li) detectors were extensively computed by Camp and Van Lehn [Cam69], and their values have been interpolated to apply to a variety of Ge(Li) detectors. The correction factors for NaI detectors were tabulated by Yates [Yat65].

In this study, Krane's method [Kra72] has been used to calculate Q_2 's and Q_4 's for the detector used in this study. Only the effect due to the finite size of the detectors was considered. In general, the Q_λ values vary slightly with the energy of gamma-rays. Since the difference over a range of energy was found to be very small, only one set of Q_λ has been used.

5.3 The Extraction of Information on Nuclear Structure

As stated in the introduction section, nuclear orientation as a reliable experimental tool can provide useful information on many physical parameters. The following is a brief discussion about theoretical consideration on which extraction of nuclear structure information is based.

Determination of spin and magnetic moment of parent state is discussed in detail by Berkes [Ber86]. In static orientation experiments the nuclear ensemble is in thermal equilibrium with the environment and B_λ parameters can be determined by Boltzmann coefficients ($\exp\{-E(m)/kT\}$). Since B_λ depends on the product of μB , the extranuclear field B has to be known to determine the magnetic moment μ .

Two methods can be used to extract μB . In the first methods, the directional distribution of a radiation (γ ray in most of cases) is observed at different temperatures, and since B_λ are the function of Δ_M/T the fit of $W(\theta)$ versus $1/T$ can in general yield the absolute value of the magnetic moment. This method is used when one knows the decay well, and there is at least one pure multipole transition in the daughter nucleus which is not preceded by many unobserved transitions (U_λ and A_λ are known). If $A_\lambda U_\lambda$ are not known unambiguously, the method can also be applied under the condition that the saturation of the orientation can be achieved. Another method to determine μB is NMR-ON in which the determination of resonant frequency gives product gB .

The hyperfine magnetic field in ferromagnetic lattices has been used to determine the magnetic moments. The ferromagnetic materials used most often are Fe, Co, Ni and Gd. In those materials, the effective field can be described by

$$\mathbf{B}_{\text{eff}} = (1+K)\mathbf{B}_{\text{ext}} + \mathbf{B}_{hf}, \quad (54)$$

where \mathbf{B}_{ext} is the applied external field, \mathbf{B}_{hf} is the hyperfine field and K is the Knight shift in the hosts. The hyperfine fields in Fe, Co, Ni and Gd lattices have been tabulated by Rao [Rao79].

The spin of the parent state can possibly be determined from the analysis of B_λ parameters. At saturation (very high B and low T), the orientation becomes sensitive to the spin. Since NMR-ON gives the g -factor directly while B_λ normally are sensitive to μ , the parent spin can also be determined by comparing the analysis of B_λ with NMR-ON results.

Determination of spins and $(L+1)/L$ multipole mixing ratios, δ : If B_λ and U_λ are known, the determination of multipole mixing ratios for a particular transition is

straightforward. Directional distribution coefficients can be evaluated from the distribution function $W(\theta)$, and the multipole mixing ratio can then be derived, as indicated by equation 52. In most of cases B_λ are not known and only a complete decay scheme will facilitate the determination of U_λ , special methods designed to get around the unknown have to be applied.

The method used extensively in this study is the relative calculation. It can be applied to the case where the transition of interest shares the same initial level with another transition of pure multipole order. Since they originate from the same level, the degree of orientation is common, and the values of $B_\lambda U_\lambda$ are the same for both transitions. For pure multipole transition the distribution coefficient is known (same as the F -coefficient), and the distribution coefficient of the transition of interest can be determined by comparing their anisotropies. This relative calculation has the advantage that many unknown and ill-determined quantities can be eliminated from the analysis and the accuracy is determined by the statistical precision of the measurements. The method may be applied in complex decay schemes in which ground state transitions ($I_i \rightarrow 0$) exist and one may have to guess the initial spin. Similarly it can be applied to the case where the transitions from the same initial state to levels of known spins, δ -value and initial spin can be determined.

For unobserved gamma radiation with mixed multipolarity (L'/L), the U_λ also depend on the multipole mixing ratios, as shown in the following equation,

$$U_\lambda(I_1 I_2) = \frac{U_\lambda(I_1 I_2 L) + \delta^2 U_\lambda(I_1 I_2 L')}{1 + \delta^2} . \quad (55)$$

In some cases U_λ can be used to extract multipole mixing ratios.

The determination of nuclear spins normally involves a few transitions in cascade. Some of them have known mutipolarities and some levels are shared among the transitions. One needs first to make assumptions about the unknown spins and then to analyze the anisotropies of all transitions. Consistency among analysis results for all involved transitions and comparison with results from different experiments (e.g. conventional spectroscopy and angular correlation) often lead to confirmation of initial

spin assignments.

There are other quantities that can be extracted from nuclear orientation data. Details can be found in Low-Temperature Nuclear Orientation edited [Sto86].

Chapter 6. The Apparatus and Experimental Details - Nuclear Orientation

In this chapter the apparatus used and techniques employed to carry out the nuclear orientation experiments will be described first, followed by the discussion of experimental procedures and data acquisition system. The production and separation of radioactive isotopes were already discussed in Chapter 3. The UNISOR on-line nuclear orientation facility (UNISOR/NOF) consists of a ^3He - ^4He dilution refrigerator on line to the mass separator. The refrigerator is the main part of the facility, which provides the low temperature necessary for nuclear orientation. The cryostat will be outlined with the refrigerator. Detailed information on low temperature techniques and working principles can be found, among others, in books by Lousnmaa [Lou74] and Betts [Bet76]. The discussion of other technical considerations (thermometry, ion implantation, spin relaxation, etc.) will also presented.

6.1 Introduction: UNISOR Nuclear Orientation Facility (UNISOR/NOF)

The schematic layout of UNISOR/NOF is shown in Fig. 6-1. The production and separation of nuclei were discussed earlier in this thesis. The ions of chosen mass leaving the isotope separator are guided through central beam line. They are bent 90 degrees by an electrostatic deflector, and refocussed by a triplet quadrupole lens, and then guided into a vertical cold (4K) beam tube before they are finally deposited onto the ferromagnetic target attached to the cold finger of the refrigerator. The temperature of the cold finger is maintained at below 10 mK. The target foil is polarized by a superconducting magnet mounted around the cold finger to provide the magnetic hyperfine field. Eight detectors can be mounted around the cold finger to observe the radiation distribution. The features of UNISOR/NOF in comparison with other on-line facilities were presented by Girit[Gir88]. The unique feature of the UNISOR/NOF facility is the bottom beam access which allows detectors to be placed at 45° angles around the cold finger. The measurement of the radiation distribution

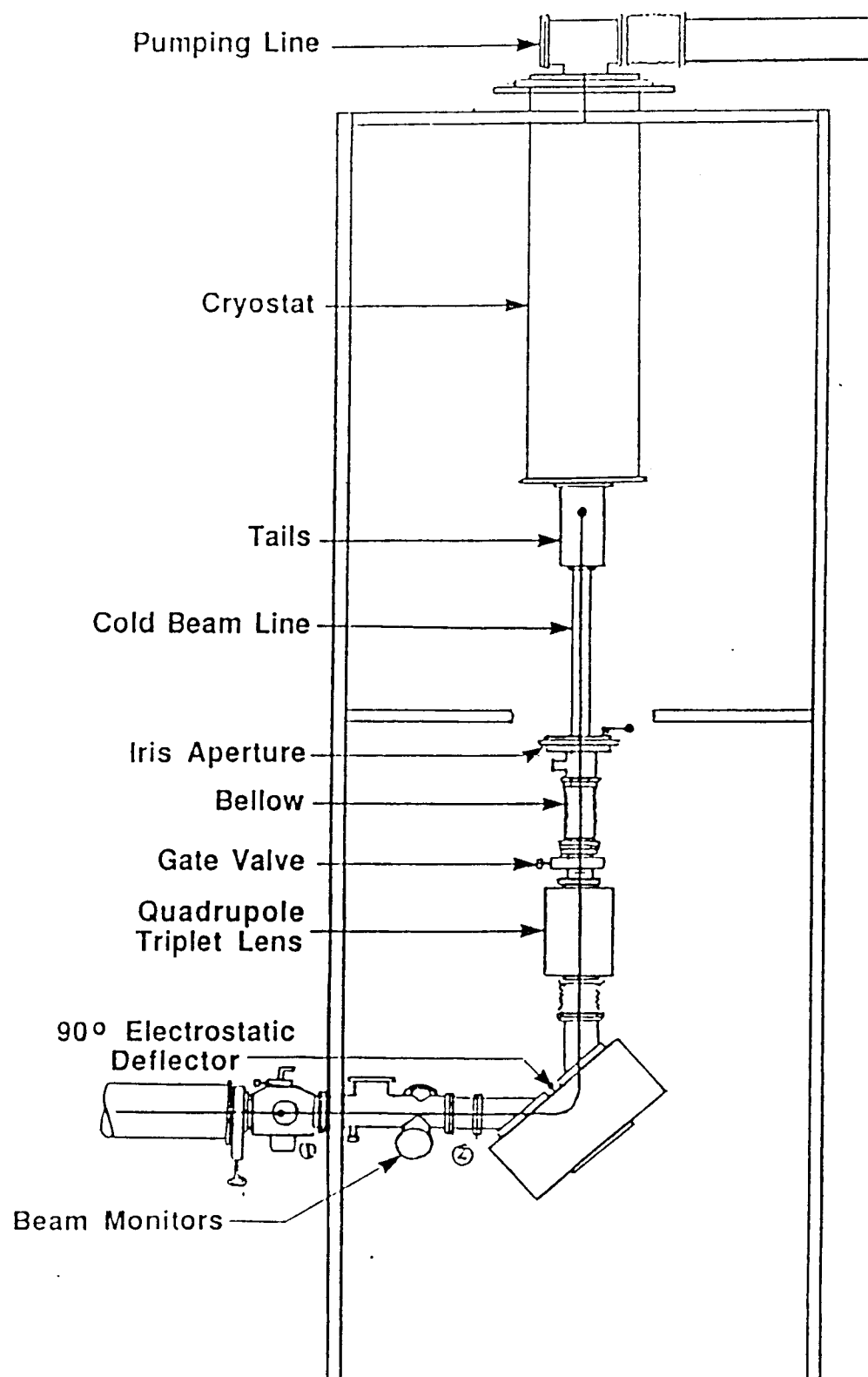


Fig. 6-1 A schematic layout of UNISOR/NOF.

at an extra angle (besides 0° and 90°) is critical if one intends to obtain both A_2 and A_4 distribution coefficients. Multipole mixing ratios can be unambiguously determined if both A_2 and A_4 values are known [Rik86]. The availability of 45° angles also allows one to set up detectors cylindrically around the cold finger and this cylindrical symmetry can be used to correct systematic counting errors associated with the beam wandering on the target. NMR apparatus has recently been installed on the facility, which would enable the investigation of NMR-ON.

6.2 The UNISOR ^3He - ^4He Dilution Refrigerator

As discussed earlier, the orientation of the nuclear ensemble requires ultralow temperature and strong magnetic field. The strong field can be provided by the magnetic hyperfine field in ferromagnetic materials placed in a less strong yet attainable external magnetic field. The only way to obtain ultralow temperature before 1967 was by adiabatic demagnetization of paramagnetic salt with which both stable low temperature and long counting periods could not be obtained. The application of nuclear orientation in the studies of nuclear structure enjoyed an explosion with the advent of the commercial ^3He - ^4He dilution refrigerator, which is capable of maintaining stable low temperatures for an indefinite time. The advantages of dilution refrigerators include their commercial availability, low base temperature, capability of continuous operation, among many others. The scope of nuclear structure study using nuclear orientation has been greatly extended by the design of top-loading facility. Radioactive samples and target can be loaded while the refrigerator is operational. This is really a very useful feature in that tremendous amount of time can be saved in cases that necessitate change of target at regular intervals (e.g. accumulation of daughter isotopes). The working principle of the dilution refrigerator was originally proposed by London et al. [Lon62] in 1962, and dilution refrigeration materialized for the first time in 1965.

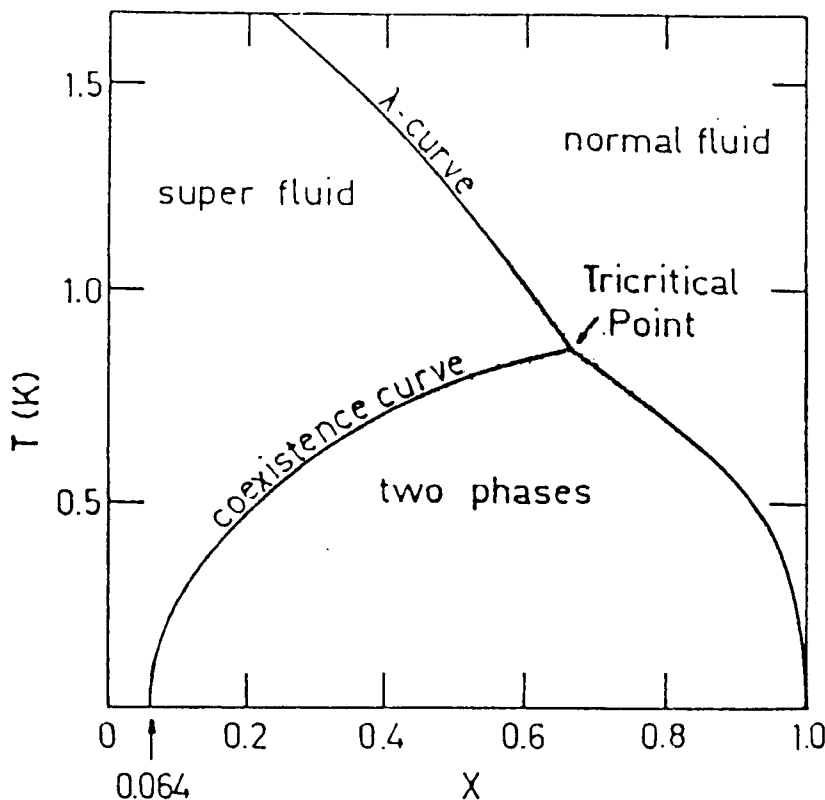


Fig. 6-2 The phase diagram of $^3\text{He}/^4\text{He}$ mixture [Oxf88].

6.2.1 Principle of dilution refrigerator

The operation of the dilution refrigerator is based on the unique properties of $^3\text{He}-^4\text{He}$ mixture at low temperature. When a mixture of the two isotopes of helium is cooled below a critical temperature, it separates into two phases as shown in Fig. 6-2, the "concentrated phase" being rich in ^3He and "dilute phase" being rich in ^4He . Since the concentration of ^3He in each phase is dependent on temperature and the enthalpies of ^3He are different in two different phases, it is possible to achieve cooling by transferring ^3He from the concentrated phase into the dilute phase. This process continues to work even at the lowest temperature where the concentration of ^3He will still be finite. That is the reason that low temperatures can be achieved with $^3\text{He}-^4\text{He}$ mixtures.

The properties of the $^3\text{He}-^4\text{He}$ mixture can be understood quantum

mechanically. When the temperature reaches below 0.5 K, the ^4He can be regarded as being in the ground state, and it has zero spin and is a superfluid. On the other hand, ^3He of spin one-half behaves like an ideal Fermi gas, moving through ^4He freely as if they were in vacuum. Since ^3He is lighter than ^4He the concentrated phase will stay on top of the dilute phase. At the phase boundary, ^3He behaves like a liquid in contact with its vapor, and ^3He in concentrated phase "evaporates" into dilute phase. If this process occurs in a chamber, it will cool the sample.

Fig. 6-3 is a schematic diagram of a continuously operating refrigerator. The ^3He - ^4He mixture is contained in the mixing chamber. As the ^3He evaporates from the concentrated phase into the dilute phase, the mixing chamber is cooled. In a continuously operating system, the ^3He must be pumped out from the dilute phase and returned to the concentrated phase keeping the system in a dynamic equilibrium. The temperature in the still is maintained by a heater around it at 0.6 to 0.7 K at which the vapor pressure of ^3He is much higher than that of ^4He , so ^3He evaporates preferentially. As ^3He evaporates from the still, its concentration becomes lower than that in the mixing chamber. It is this pressure difference that drives ^3He from the mixing chamber up to the still. A series of heat exchangers above the mixing chamber is used for the outgoing ^3He to cool the incoming flow of concentrated ^3He . The ^3He is removed from the still by a powerful vacuum pumping system, and with impurities removed by cold traps and filters it is returned to the cryostat. The condenser contains ^4He and is used to precool the returned ^3He . A flow impedance made of a capillary tube is used to condense the precooled ^3He gas. The arrows in Fig. 6-3 show the circulation circle. The mixture flows in the opposite direction during the cool-down of the refrigerator when the mixture is stored in tanks in the form of high pressured gas.

The cold finger is mounted in good contact in the mixing chamber, providing the low temperature necessary for the orientation of the nuclear ensemble. A coil heater is equipped around the mixing chamber to achieve a higher temperature, if experimenter so desires.

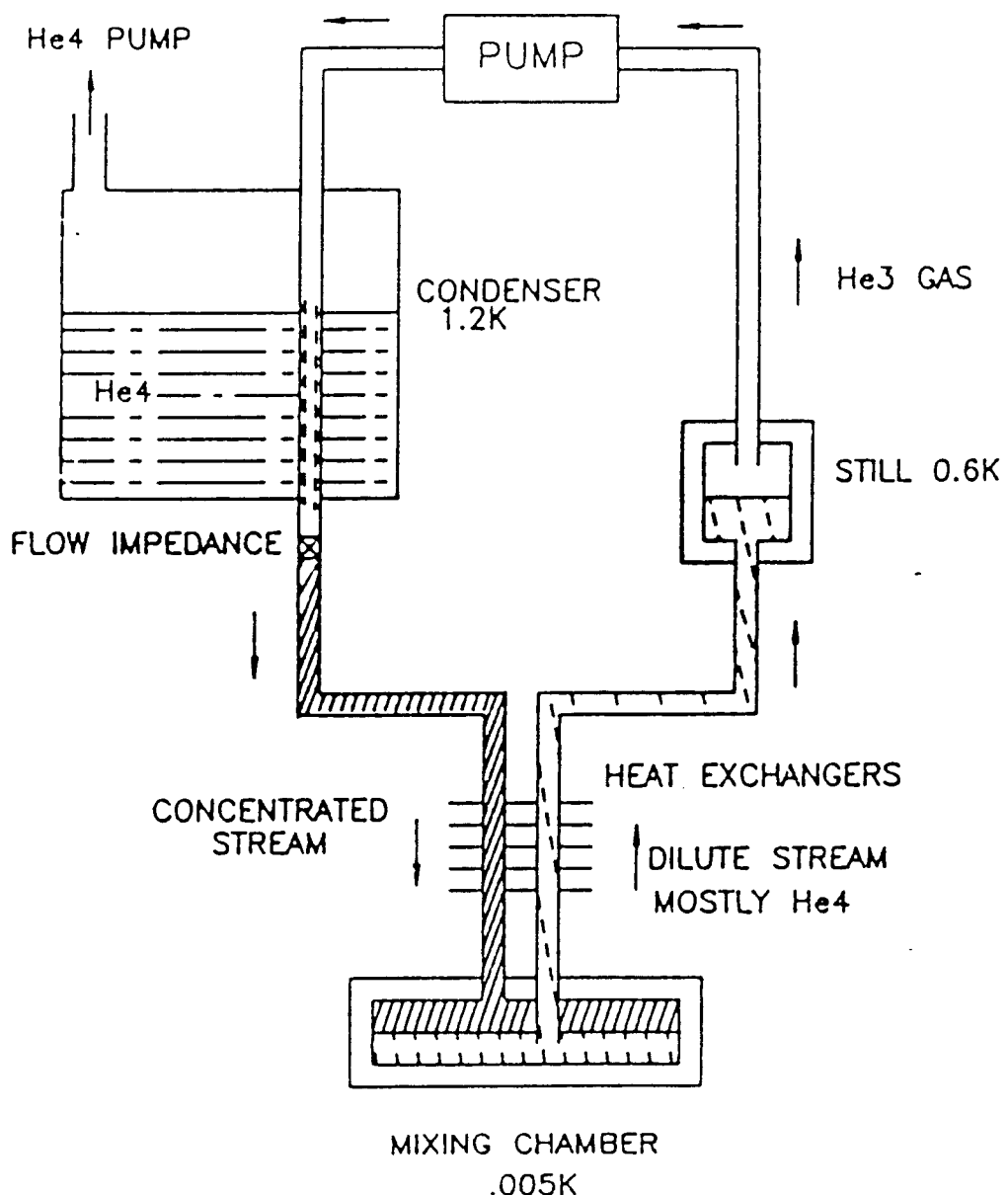


Fig. 6-3 Simplified schematic diagram of continuously operating refrigerator.

6.2.2 The ^3He - ^4He dilution refrigerator on UNISOR/NOF

The refrigerator at UNISOR (Fig. 6-4) was manufactured by Oxford Instruments, Ltd., and is of standard design with minor modifications of the tail and magnet for bottom beam access. Inside the cryostat wall, there is liquid nitrogen jacket and a helium vessel. Both the space between the outer wall and liquid nitrogen jacket (Outer Vacuum Chamber) and the space between the nitrogen jacket and helium vessel are evacuated for thermal isolation. The ^3He - ^4He dilution unit is mounted inside the vacuum chamber immersed in the helium vessel. The refrigerator is operated with a powerful rotary pump backed by an oil diffusion pump. At a circulation rate of 500 $\mu\text{mol/s}$ the cooling power of the refrigerator can be approximated by the relation: $Q(\mu\text{W}) = 0.017(T^2 - 44.9)$, where $T(\text{mK})$ is cold finger temperature. The lower part of the dilution unit is surrounded by four tails as vacuum and thermal shields. The outer tail has a diameter of 18 cm, so that the closest distance between source and detectors is 9 cm. Normally detectors are set about 1 cm from the outer tail. A superconducting magnet is linked to the helium bath and mounted around the cold finger, providing a magnetic field up to 1.5 Tesla with the field perpendicular to the beam direction. There is a 2.2 cm opening at the magnet bottom for beam entrance. A Faraday cup under the magnet is mounted on the 4 K shield to be used for monitoring the beam profile and as a baffle for off-line run (minimum temperature can be achieved with this baffle and iris closed). Connected to the tails is the cold beam line in which there is a plug (as thermal radiation stopper from the beam line), a pair of electrostatic deflectors (for steering the focused beam to the cold finger) and an iris (used to control the beam size). The top loading equipment facilitates the change of target materials without interrupting the operation of the refrigerator.

The cryostat is mounted in a 6 meter high frame with two platforms (one for top-loading operation, the other for detectors and electronics). All pumps and control panels are separated from the cryostat. The experiments performed so far show that a base temperature of 5 mK can be reached with all baffles closed, and a temperature around 8 mK can be maintained with the beam line open. The temperature during the

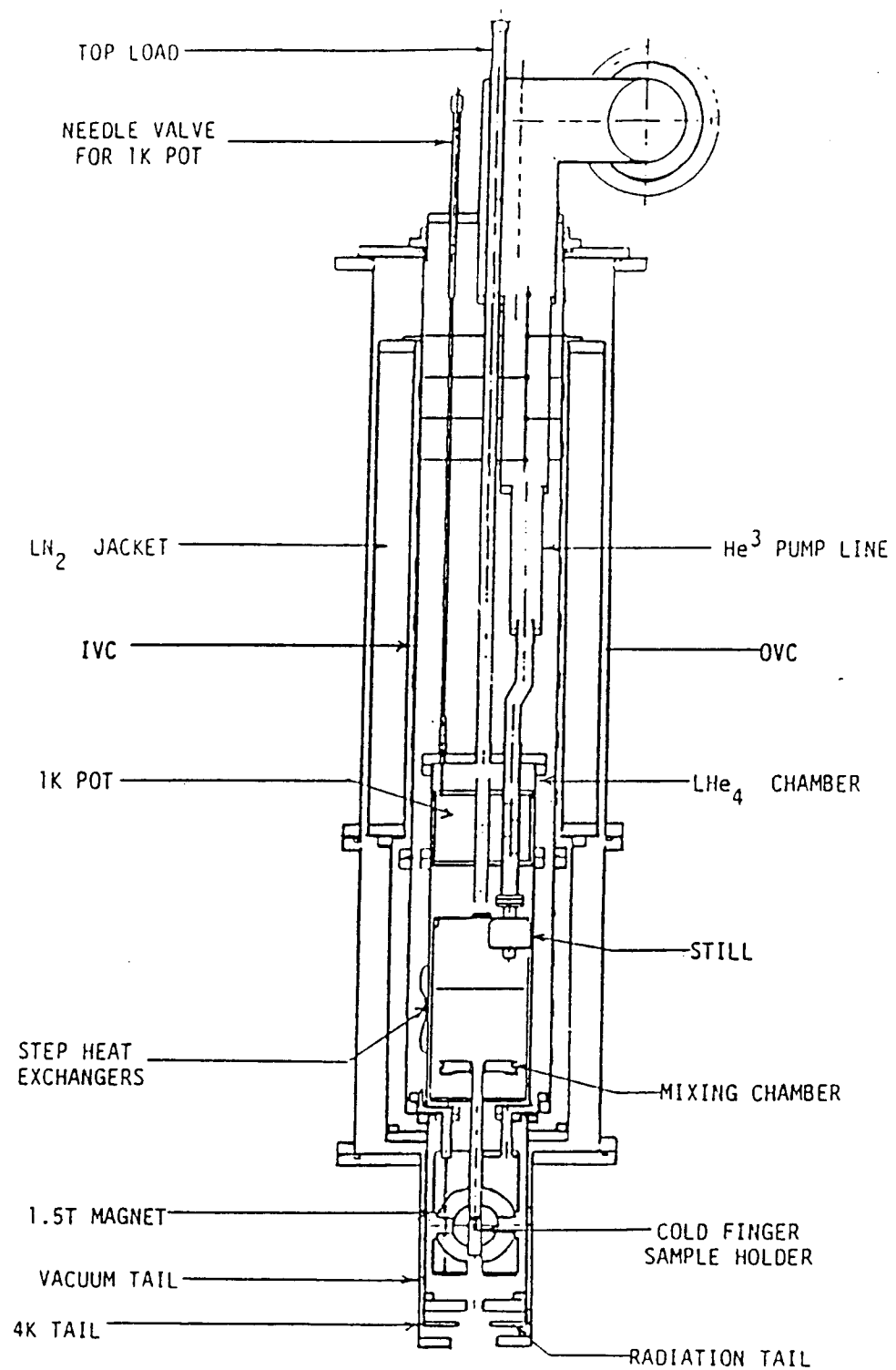


Fig. 6-4 Schematic diagram of UNISOR dilution refrigerator.

cool-down period can be monitored by calibrated carbon resistors (five of them are anchored at different places inside the unit), and a nuclear orientation thermometer has to be used when the temperature reaches the mK range.

6.3 Nuclear Orientation Thermometry

For the temperature below 1 K, radioactive nuclear orientation thermometers have to be used partly because these very low temperature measurements are normally performed in the presence of strong magnetic fields. As shown in Chapter 5, the distribution function $W(\theta)$ of radiation from oriented nuclear ensemble depends on the temperature T , magnetic hyperfine field and nuclear structure parameters. For some nuclei in which the hyperfine interaction and nuclear parameters are well known, the measurement of the anisotropy of gamma radiation emitted from these oriented nuclei can be used to determine temperature. These radiation sources therefore are used as an absolute (thermodynamic) thermometer. Since Δ_M in equation 48 can be measured with high precision through various experiments, nuclear orientation thermometry can be used as a direct and accurate means of measuring temperatures below 1 K. A detailed discussion of orientation thermometry can be found in Marshak[Mar88].

Among the nuclei whose low-temperature orientation properties are well known, three are commonly used as reliable thermometer sources. ^{54}Mn , ^{60}Co and ^{57}Co in a ferro-magnetic host such as iron and nickel provide temperature measurements in the range of 1.8 mK to 66 mK with reasonable accuracy. All three nuclei have simple and well-established decay schemes, and they compensate each other in terms of temperature sensitivity and radiation energy. The temperature sensitivity of a thermometer source is defined as $\delta W(\theta)/(\delta T/T)$. Fig. 6-5 shows the sensitivity curves for these thermometer nuclei in different ferromagnetic hosts. The factors to consider in choosing one thermometer source over another include the range of temperature measured and the peak position of the thermometer radiation relative to peaks of interest in the spectrum. The advantage of using ^{54}Mn lies in the fact that it does not cause radiation heating because it decays by electron capture and it emits

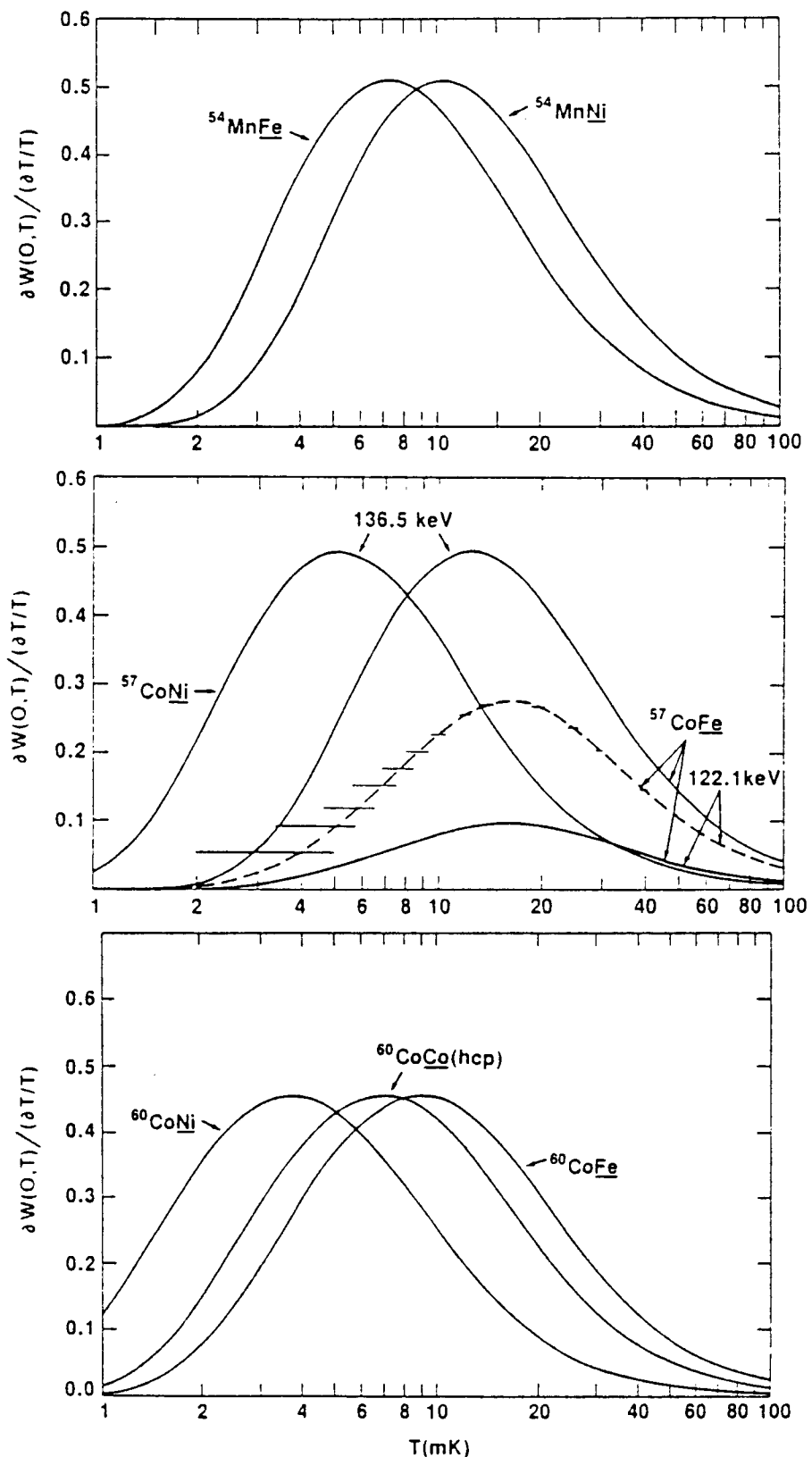


Fig. 6-5 Temperature sensitivity curves for three commonly used thermometers [Mar88].

a single, pure E2 transition of energy 835 keV. But both ^{57}Co and ^{60}Co have two gamma transitions that can be used for temperature measurement and they offer more flexibility in the choice of sensitivity range and energy. When ^{60}Co is used as thermometer source, extra caution should be exercised because all the low energy peaks will build on the Compton edge of high energy thermometer lines.

6.4 Sample Preparation

The preparation of the sample is a crucial part of the nuclear orientation experiment in that the orientation measurements deal with the hyperfine interaction of the nuclei under study with their ferromagnetic hosts. The achievement of a measurable magnitude of orientation depends, to a large degree, on whether the radioactivity can be fully incorporated into substitutional sites in the host lattice. The sample preparation in on-line experiments usually consists of two steps: the incorporation into the host lattice of the thermometer radioactivity (usually 0.1 to 10 μCi) by thermal diffusion, or crystal growing and the implantation of mass separated sources into the ferromagnetic host material. The first step, which is also the preparation procedure for samples used in off-line experiments, mainly involves depositing a drop of thermometer radioactivity on the ferro-magnetic foil and heating the foil in an oxygen-free environment at a certain temperature for a period of time. The foil is then polished with acetone or alcohol using steel wool after being removed from the oven, and stored in an inert atmosphere (usually vacuum) before being used. In the second step, the foil is soldered onto the cold finger and loaded in the refrigerator. The radioactive atoms coming out of the isotope separator are directed toward the cold finger and deposited on the foil for implantation.

There are practical problems in sample preparation that warrant special care and considerations. In alloying the radioactivity with the host, the radioactivity should be carrier free, and problem may arise when contaminants are introduced into the sample during the preparation process. The diffusion temperature and time are sometimes not known, but for some radioactive isotopes they can be estimated from

the diffusion coefficients [Ask70]. The number of isotopes that can be incorporated into a certain host lattice is limited due to the fact that the isotopes must be soluble in the host material. The solubility of elements in each other may be estimated theoretically. Other problems such as oxidation and formation of chlorides on host foils during the diffusion process can be avoided by heating the foils in an inert gas environment and by placing the foils in a hydrogen filled test tube, respectively. After foils are removed from the oven, excessive activity on the surface should be reduced by washing with dilute acid like HNO_3 and by gently rubbing with steel wool, but extra care should be taken not to damage the foil surface.

Ion implantation is the only practical method of incorporating the rare-earth isotopes into the host lattice since these elements are normally insoluble in iron and nickel. There are limitations associated with this method. Energy, beam intensity and quality of the foil surfaces are among the factors that should be considered in order for isotopes to experience maximum hyperfine field and achieve a sizable orientation. Another important factor to be considered in ion implantation is the spin-lattice relaxation (SLR) time. In on-line experiments the ions are implanted into the foil with random spins and they become oriented by spin-lattice relaxation interaction with a characteristic time constant T_1 . The implanted nuclei can reach thermal equilibrium with the host lattice before they decay only if their half-life is much greater than the spin-lattice relaxation time. At low temperature T_1 values vary depending on the impurity-host combination, and they are normally in the range of 1 s to 100 s. In order to achieve orientation the half life should be at least comparable to T_1 , and this has put severe limitation on the number of isotopes far from stability that can be studied via on-line nuclear orientation. The theory of nuclear spin-lattice relaxation relevant to nuclear orientation can be found in the works of many authors, and a complete treatment of the problem is given by E. Klein [Kle87].

6.5 Data Acquisition System

The UNISOR/NOF data acquisition system (Fig. 6-6) is based on a Tennecomp

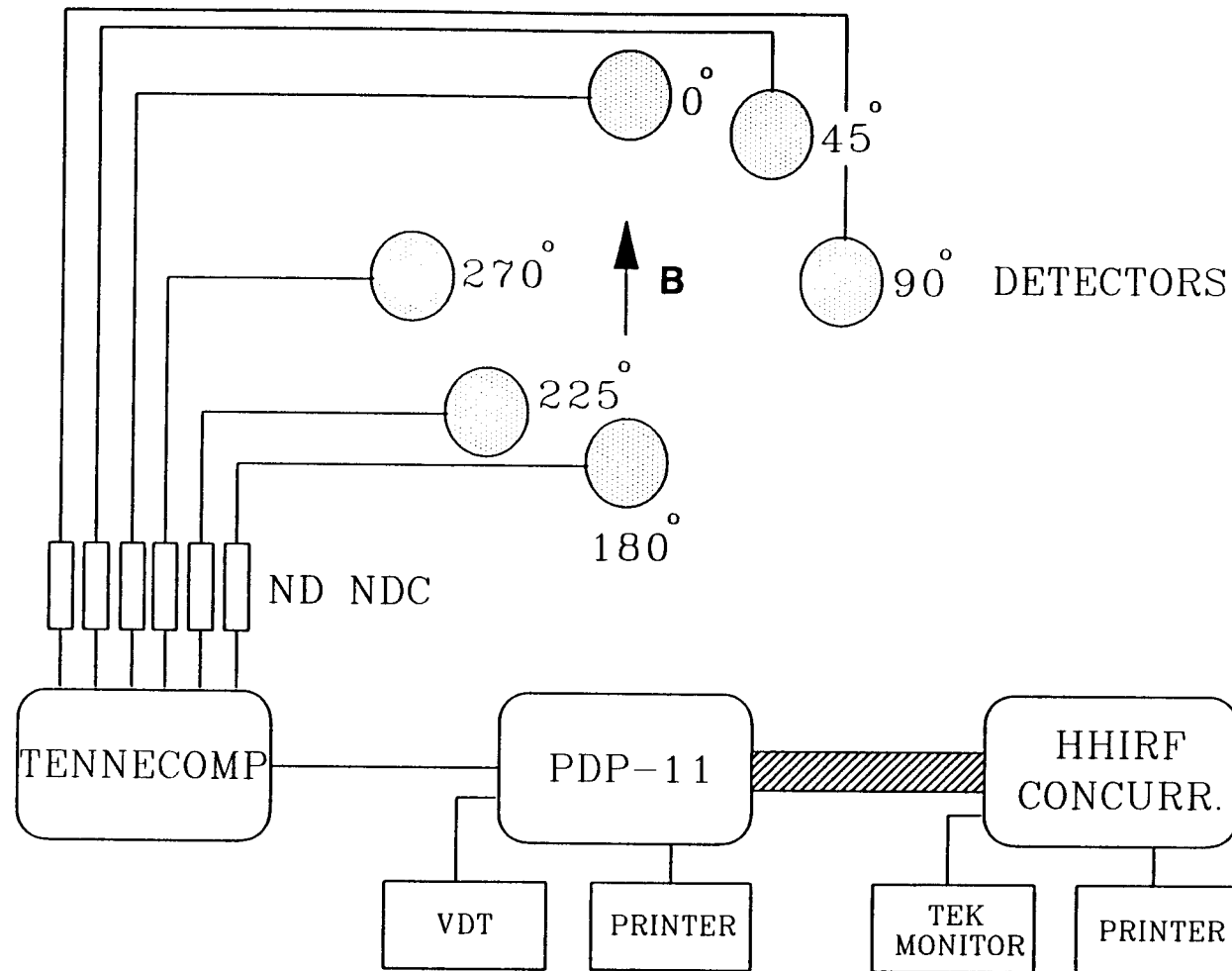


Fig. 6-6 UNISOR/NOF data acquisition system.

TP5000 and the HHIRF Concurrent computer. On the Tennecomp, up to six ADC's, display and disk storage device are interfaced to a PDP11 computer. It is also linked to the HHIRF concurrent main frame computer through a CAMAC interface, and spectra can be transferred to the main frame for real time and off-line data analysis. The software control on both computers provides the selection of collection time, number and length of spectra to be transferred and type of data storage. A separate program accesses the data on the disk and calculate the anisotropies of up to three transitions, providing real time monitoring of temperature and the alignment of sample on the target.

Up to eight detectors can be placed around the oriented sample at UNISOR/NOF. This configuration with the beam access from the bottom allows to take data at 45° , thus makes it possible to obtain values of $a_2(=B_2U_2A_2)$ and $a_4(=B_4U_4A_4)$ directly. As shown by K. Krane [Kra88], this is an advantage over other designs not only for nuclear structure study, but for the study of hyperfine interaction mechanisms and solid state phenomena.

6.6 Experimental Procedures of Nuclear Orientation of ^{184}Au

The nuclear orientation of ^{184}Au was performed following the spectroscopy experiment. The nuclei were produced using the same reaction as in the spectroscopy experiment (chapter 3). The activity was mass-separated on-line in the UNISOR separator and then transported through the central beam line to the UNISOR Nuclear Orientation Facility. The radioactive nuclei of ^{184}Au were implanted at 50 kV into a polarized target, an iron foil diffused with thermometer activity which was soldered onto the copper cold finger of the refrigerator. The refrigerator was operated at a temperature below 7 mK with beam on target. The angular distributions of the γ -rays were observed with an array of 6 Ge detectors surrounding the target at a distance of about 10 cm. The positions of the six detectors were 0° , 45° , 90° , 180° , 225° and 270° relative to the polarization direction (see Fig. 6-6). During the measurement the refrigerator was cycled between the lowest attainable temperature ("cold") and above

500 mK ("warm") to facilitate the normalization of "cold" rates to the isotropic "warm" counts in data analysis (see next chapter). For each detector, a total of 400 spectra (each of 5 minutes duration) was collected, which was organized into 6 cold-warm cycles. The time for each spectrum was so chosen that the temperature and beam rate during this period could be considered stable. A top-loading was performed mid-way through the experiment in an attempt to remove the build-up of daughter nuclei (^{184}Ir). Spectra were transferred to the Concurrent main frame computer and analyzed for continuous temperature monitoring and the beam rate was also constantly monitored by observing the ratio of the count for a particular peak of interest to that of a thermometer peak.

^{57}Co in Fe was used as the thermometer for the present study. ^{60}Co has the disadvantage of contributing to the background through its Compton edge. The single energy γ -ray in the decay of ^{54}Mn coincides with one of the γ -rays in the decay of ^{184}Au , and this prevented its use as thermometer source. Both γ -rays in the decay of ^{57}Co may be used to determine the sample temperature. The 122-keV one is stronger and has a larger anisotropy. Unfortunately there was a small contaminant peak at its low energy tail from the daughter activity. The γ -ray at 136-keV was strong enough to provide good statistics and it stood as an isolated peak in the spectrum, therefore its count rate was used to monitor the temperature change during the data acquisition. In preparing the thermometer sample, a small amount of ^{57}Co activity dissolved in HCl was deposited on an iron foil of thickness 0.1 mm and diameter 1.0 cm, and heated in oven at a temperature of 850 K for about 12 hours. All samples were tested in the refrigerator before the experiment.

The hyperfine interaction of ^{184}Au with ferromagnetic environment had been studied before the start of this study. Laser spectroscopy measurements [Kro88] had yielded the g-factor for the 53 s state of ^{184}Au but were able only to predict that the spin for the state lies between 3 to 8. At NICOLE a NMR/ON study covering the prediction of laser spectroscopy for $I = 3 - 8$ was carried out in an attempt to determine the spin, and was not successful. The spin-lattice relaxation of ^{184}Au in Fe was studied by NICOLE and ISOLDE collaboration [Sto88], and only sketchy result

was available at the time of this experiment. It was shown that full equilibrium is present for 273 keV γ -ray after 100 seconds.

Chapter 7. Data Analysis and Results - Nuclear Orientation

Various methods for the analysis of nuclear orientation data have been developed in the past. Different approaches may be taken in analyzing data from different experiments, depending on the aim of the experiment, specific experimental configuration, what parameters are available and what are the parameters that can be deduced elsewhere. In the following section, a general description about the data analysis methods applied to UNISOR/NOF experiments will be introduced, followed by a detailed discussion about steps that have been taken to extract nuclear structure information in this presentation.

7.1 UNISOR/NOF OLNO Data Analysis

As described in Chapter 5 (equation 38), the angular distribution function of γ -ray takes the following practical form for axially symmetric ensemble of nuclei:

$$W(\theta) = 1 + Q_2(\theta)a_2P_2(\cos\theta) + Q_4(\theta)a_4P_4(\cos\theta) \quad (56)$$

where $a_2=B_2U_2A_2$, $a_4=B_4U_4A_4$ and θ refers to the detector positions, i.e. 0° , 45° and 90° in UNISOR/NOF experimental configuration. What is observed by a detector at a given angle is the number of counts N_i in a given time t_i . The live time t_i is different as detectors have different dead times, but each data run lasts for a fixed clock-time. This guarantees that for all detectors each data point averages over the same variation in beam rates, temperature, radioactive decay and relaxation. When we take the ratio of counts for two detectors, the time-dependent effects can be canceled out. N_i is related to other experimental quantities by the following equation:

$$N(\theta, T) = \dot{N}(T)\epsilon(\theta)\Omega(\theta)W(\theta, T)t(\theta, T)b_\gamma \quad (57)$$

where $\dot{N}(T)$ is the beam rate at temperature T , $\epsilon(\theta)$ represents the intrinsic efficiency of the detector at position θ , $\Omega(\theta)$ is the solid angle subtended by that detector, $W(\theta, T)$

is the γ -ray distribution function as expressed in equation (56), $t(\theta, T)$ is the live time and b_γ includes all branching factors in the decay.

As mentioned in the previous chapter, data should be taken at both "cold" temperature T_c and "warm" temperature T_w . At T_w the isotropic radiation of γ -rays means that $W(\theta, T_w) = 1$. We define $R(\theta)$ as the ratio of the normalized counting rate at angle θ to that at 0° :

$$R(\theta) = \frac{[N(\theta, T_c)/t(\theta, T_c)]}{[N(\theta, T_w)/t(\theta, T_w)]} / \frac{[N(0^\circ, T_c)/t(0^\circ, T_c)]}{[N(0^\circ, T_w)/t(0^\circ, T_w)]} = \frac{W(\theta, T_c)}{W(0^\circ, T_c)} \quad (58)$$

where θ refers to the detector positions other than 0° and 180° , and $N(\theta, T_c)$ and $N(\theta, T_w)$ represent cold and warm counts at position θ respectively. Since there are two unknown quantities (a_2 and a_4) in equation 56 and we make measurements at two other angles (45° and 90°) besides 0° or 180° , as indicated in the following two equations this definition allows us to solve for a_2 and a_4 directly from equation 56, eliminating all the unknown quantities (detector efficiency, transition branching ratio and solid angle) as well as time-dependent effects such as beam rate and decay time.

$$R(45^\circ) = \frac{1 + \frac{1}{4}Q_2(45^\circ)a_2 - \frac{13}{32}Q_4(45^\circ)a_4}{1 + Q_2(0^\circ)a_2 + Q_4(0^\circ)a_4} \quad (59)$$

$$R(90^\circ) = \frac{1 - \frac{1}{2}Q_2(90^\circ)a_2 + \frac{3}{8}Q_4(90^\circ)a_4}{1 + Q_2(0^\circ)a_2 + Q_4(0^\circ)a_4} \quad (60)$$

where Q_2 and Q_4 are solid angle correction factors and are characteristic of detector structure and source-to-detector distance, which are normally known.

In the analysis of data taken with 6 detectors (only two detectors along 45°), all 8 possible combinations of angles along three directions (0° and 180° , 90° and 270° , 45° and 225°) should be used, in order to correct for any systematic uncertainty caused by small fluctuations in the beam position on the target. For the 8 detector configuration, the data analysis is done by first averaging $R(\theta)$ for each pair of 45°

detectors, and then combining each average with 0° and 90° detectors. All together there are 16 combinations, and nearly perfect elimination of systematic error associated with movement of the beam can be achieved in this case. Another advantage of using more than 3 detectors is the reduction of uncertainty in a_2 and a_4 , which, for 8-detector system, could amount to 0.65 relative to measuring with only 3 detectors.

The a_λ ($\lambda=2,4$) coefficients are the product of B_λ , U_λ and A_λ . Once a_λ values are solved for from equations 59 and 60, one of these three quantities can be determined if the other two are known. As discussed in Chapter 5, if $U_\lambda A_\lambda$ are known unambiguously the spin and magnetic moment of parent state can possibly be determined from the analysis of B_λ parameters. On the other hand, if we know B_λ and U_λ , A_λ can be evaluated, and nuclear structure information such as multipolarity of gamma transition and level spins can then be deduced. The determination of U_λ normally requires a thorough knowledge of decay scheme, and theoretically the orientation parameter, B_λ can be determined with the knowledge of temperature T , hyperfine field B , nuclear spin I_0 and magnetic moment μ . Yet in most practical cases, the decay scheme is incomplete and even if T , B , I_0 and μ are known we may not be able to determine B_λ as this may depend on the method of source preparation, impurity sites, relaxation time, etc. Many techniques aimed to get around these difficulties have been developed in the past and they can be found in relevant materials.

7.2 Data Analysis of Nuclear Orientation of ^{184}Au

During the experiment about 400 5-minute spectra in 6 cold-warm cycles were collected for each detector with each cold-warm cycle lasting about 4 hours. All spectra were transferred from Tennecomp computer to Concurrent main frame and stored in the binary-formatted SPK files (254 spectra in each SPK file). For each cold-warm cycle spectra were grouped into cold and warm categories, and in order to achieve reasonable statistics they were summed up into two separate files representing

respectively cold and warm counts. The summing of spectra was made on the following basis: 1) the spectra that were summed into one file must be taken at the same temperature; 2) the beam rates at which these spectra were taken should be reasonable; 3) cold and warm spectra should represent the counts from sources at the same position on the cold finger (to justify the use of the ratio of cold to warm counts). The summing of spectra represented an averaging process for every detector. The live time for the sum file of each detector was different. As pointed out in the previous section, since they were collected in the same period of clock-time, the time-dependent parameters would be canceled out when ratios of counts from different detectors were taken in the data analysis.

Before making the sum files, all individual spectra were first checked for deficiencies such as gain shift, poor resolution, etc., and then the intensities for the thermometer line (which is 136 keV) and the strongest line in the decay of $^{184}\text{Au} \rightarrow ^{184}\text{Pt}$ (163 keV) were extracted (using the code SAMPO) for every spectrum in every cold-warm cycle. The plot of the intensities of the 136-keV thermometer line against time is shown in Fig. 7-1, which represents the temperature curve throughout the experiment. Shown in Fig. 7-2 is the beam rate curve which is the plot of intensities of the 163-keV line against time. To understand the nature of beam movement on the target due to the instability in separator operation, ratios of the 163-keV intensities from pairs of diametrically opposite detectors ($0^\circ/180^\circ$, $45^\circ/225^\circ$ and $90^\circ/270^\circ$) were plotted against time throughout the run. Fig. 7-3 is one of these beam profile plots (for $0^\circ/180^\circ$). As it turned out, among the 6 cold-warm cycles only 3 cycles (cycle 1, 4 and 6) could be used to make cold and warm sum files based on the above three criteria. The other 3 cycles were not used either because the beam rate was low, or because the beam movement on the target was too violent.

For each detector all the peaks in the cold and warm sum files were first identified and then fitted using SAMPO and areas were calculated. Following the necessary live-time corrections, the a_λ coefficients of the strong transitions in the decay were extracted according to equations 57 to 60. The first step was to normalize the cold to warm counts for each detector, which removed all the unknown terms

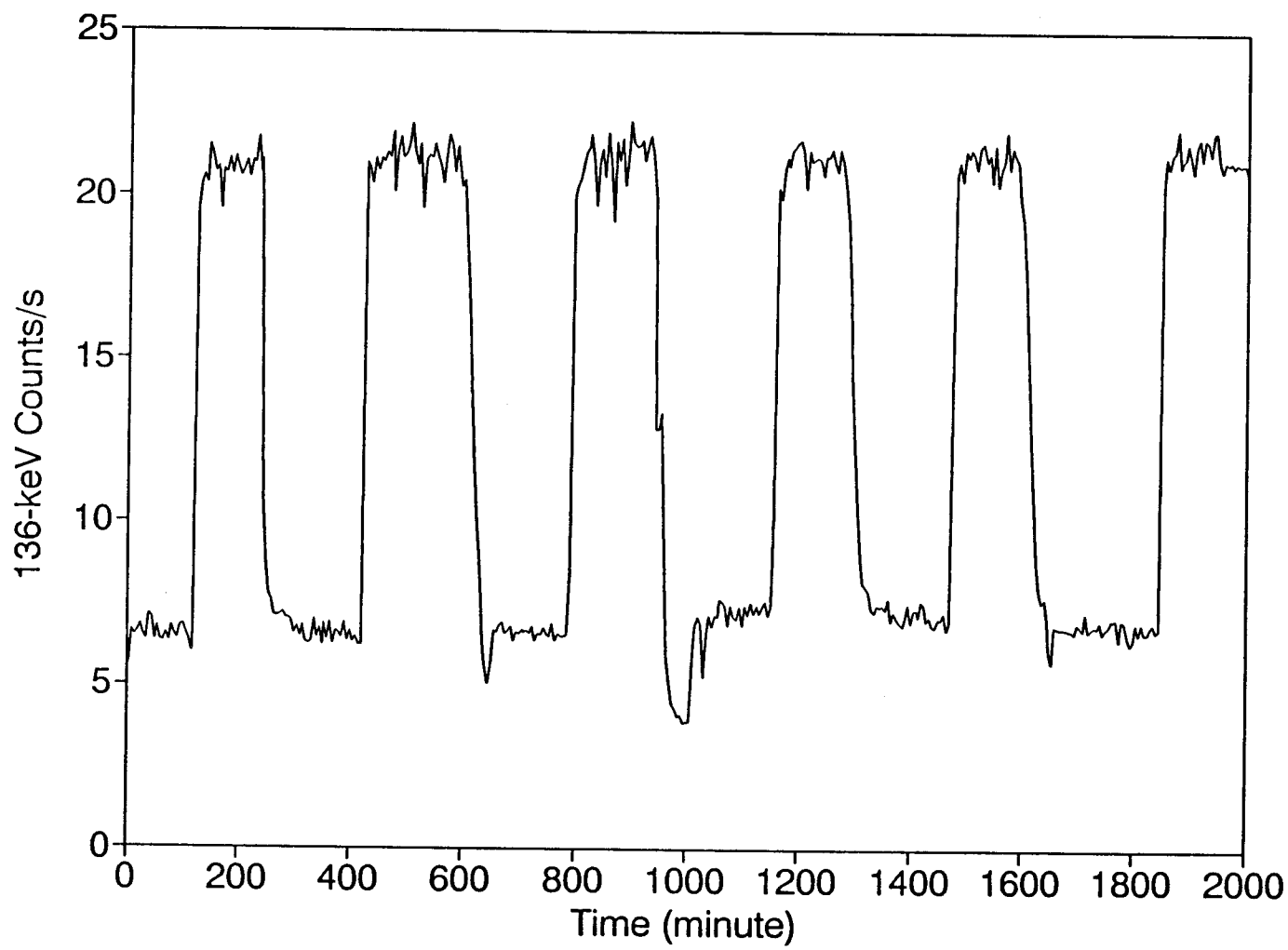


Fig. 7-1 Temperature curve: count-rates for the 136-keV ^{57}Co thermometer line at 0°.

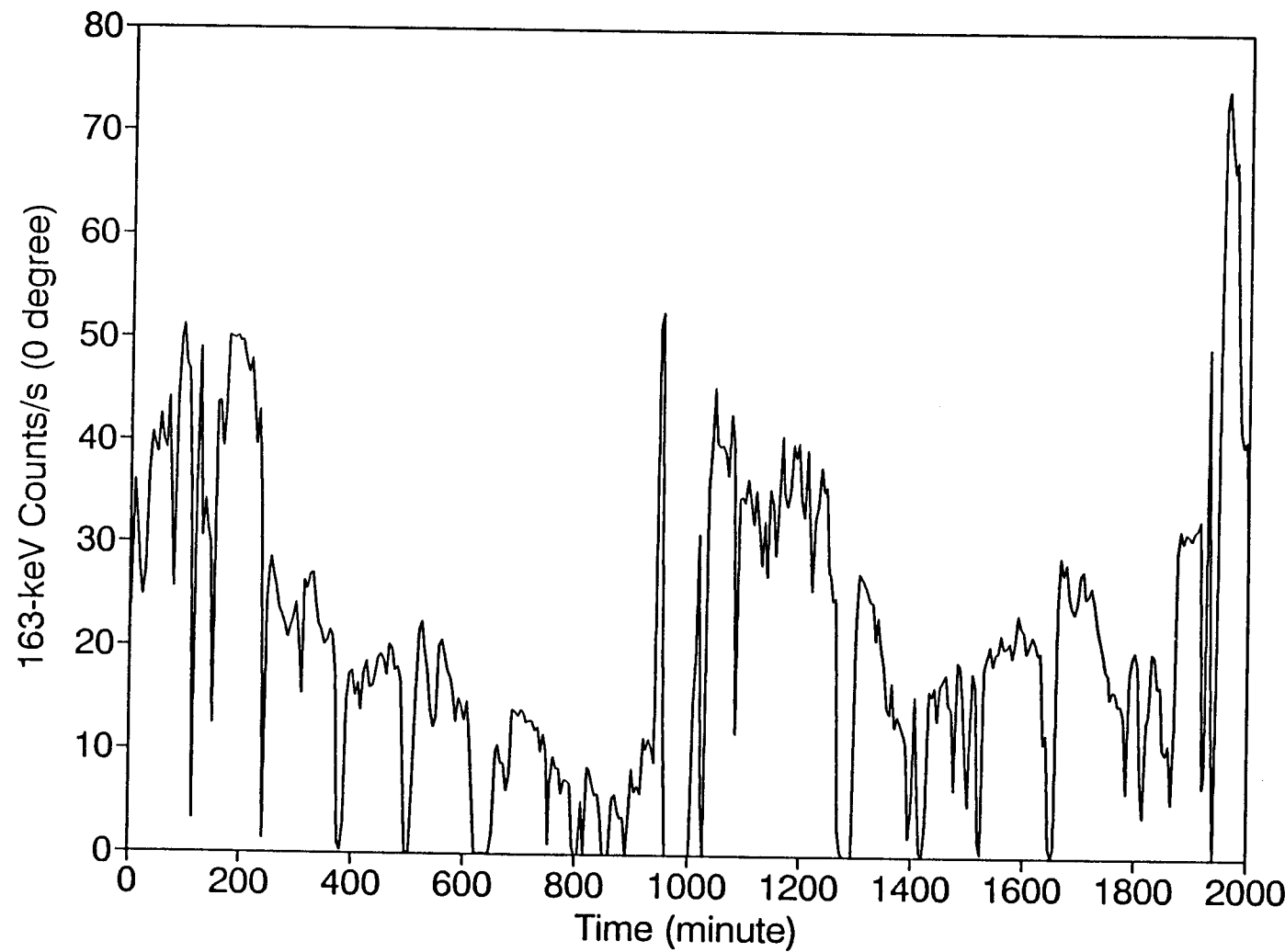


Fig. 7-2 Beam rate curve: count-rates for 163-keV ^{184}Pt line at 0°.

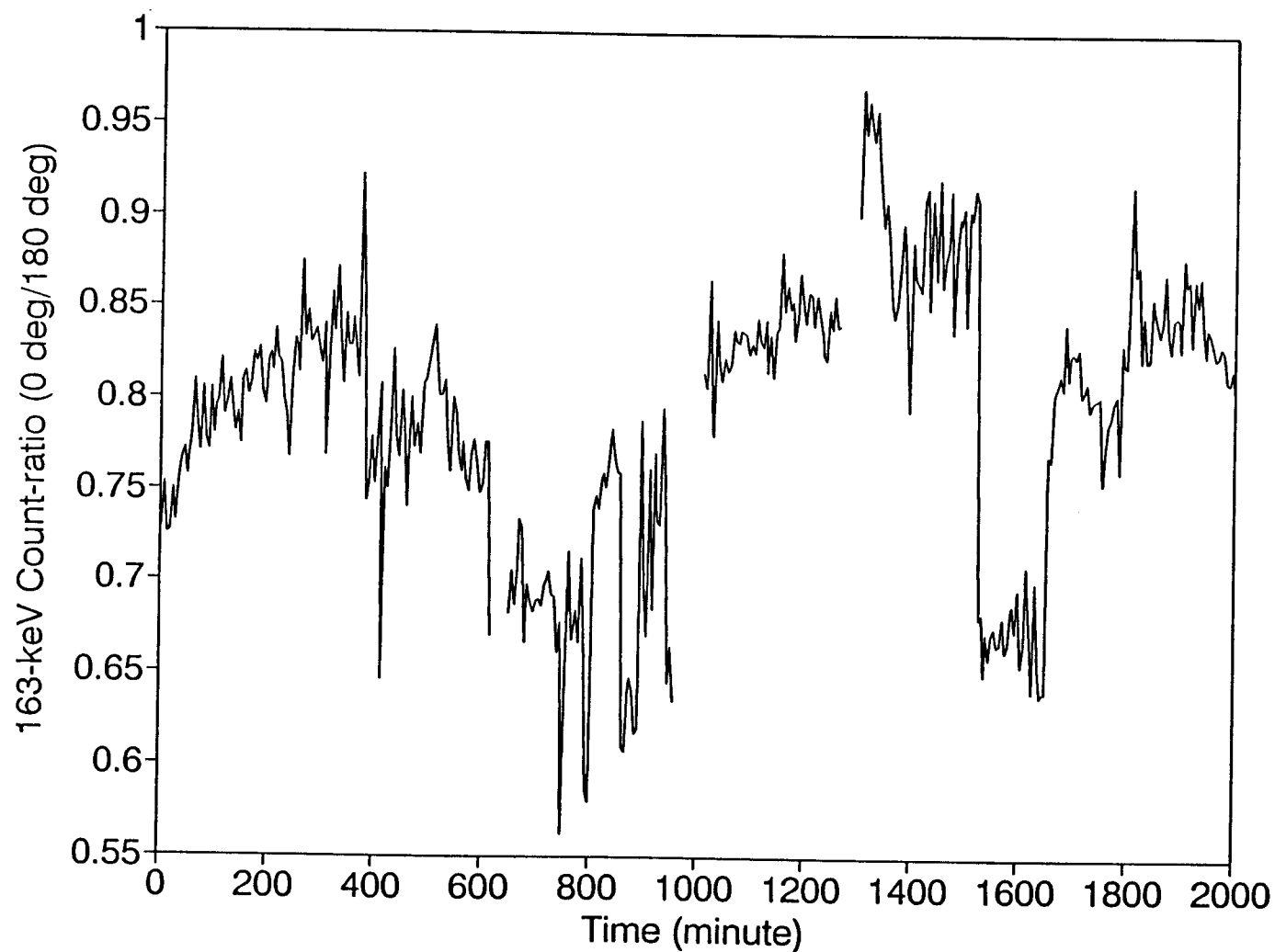


Fig. 7-3 Beam profile: count-rate(0°)/count-rate(180°) for 163-keV ^{184}Pt line.

Table 7-1 Compilation of a_2 and a_4 coefficients for the strong transitions in the decay of $^{184}\text{Au} \rightarrow ^{184}\text{Pt}$.

$E_\lambda(\text{keV})$	a_2	Err	a_4	Err
122.1 ^{a)}	0.155	0.005	-0.001	0.007 ^{b)}
	0.148	0.005	0.011	0.007 ^{c)}
	0.161	0.005	-0.014	0.007 ^{d)}
136.5 ^{a)}	-0.560	0.005	-0.144	0.006
	-0.555	0.005	-0.116	0.006
	-0.551	0.005	-0.151	0.006
163.0	-0.066	0.007	-0.003	0.006
	-0.076	0.007	0.007	0.006
	-0.072	0.006	-0.034	0.006
221.9	-0.125	0.018	-0.016	0.024
	-0.151	0.019	0.031	0.023
	-0.130	0.019	-0.042	0.022
272.9	-0.087	0.004	-0.025	0.006
	-0.102	0.003	0.001	0.004
	-0.087	0.004	-0.010	0.004
352.1	-0.112	0.043	0.041	0.053
	0.076	0.045	-0.090	0.062
	-0.157	0.046	0.142	0.064
362.3	-0.101	0.004	-0.014	0.006
	-0.104	0.004	-0.007	0.005
	-0.090	0.004	-0.058	0.005
377.0	-0.235	0.059	0.095	0.067
	-0.248	0.080	0.208	0.069
	-0.095	0.072	-0.157	0.077
379.1	-0.061	0.026	-0.052	0.033
	-0.119	0.034	0.040	0.035
	-0.087	0.034	-0.078	0.036
390.3	-0.054	0.004	-0.026	0.011
	-0.070	0.008	-0.035	0.009
	-0.075	0.005	-0.020	0.006

Table 7-1 (continued)

E_λ (keV)	a_2	Err	a_4	Err
432.2	-0.097	0.016	-0.028	0.019
	-0.079	0.019	-0.066	0.024
	-0.158	0.021	0.005	0.023
434.8	-0.101	0.034	-0.087	0.041
	-0.145	0.034	0.014	0.040
	-0.066	0.034	-0.070	0.038
485.7	0.032	0.009	-0.011	0.012
	0.019	0.011	0.000	0.014
	0.004	0.013	0.004	0.016
591.9	0.093	0.012	-0.089	0.016
	0.090	0.015	-0.037	0.018
	0.089	0.016	-0.072	0.018
600.4	0.174	0.050	0.062	0.060
	0.006	0.041	0.007	0.050
	0.106	0.029	-0.043	0.039
626.2	0.038	0.062	-0.016	0.071
	0.011	0.046	0.067	0.053
	0.132	0.033	0.022	0.042
648.7	-0.059	0.017	0.009	0.020
	-0.079	0.020	-0.040	0.023
	-0.056	0.019	-0.035	0.023
664.2	0.112	0.016	-0.075	0.020
	0.039	0.019	-0.006	0.022
	0.098	0.018	-0.040	0.023
680.9	0.093	0.063	-0.100	0.082
	0.096	0.063	0.122	0.078
	0.077	0.066	-0.023	0.080
776.8	-0.018	0.010	0.014	0.013
	-0.045	0.011	-0.029	0.014
	-0.014	0.013	-0.026	0.015

Table 7-1 (continued)

E_λ (keV)	a_2	Err	a_4	Err
798.4	-0.178	0.029	0.005	0.033
	-0.090	0.034	-0.020	0.041
	-0.092	0.034	-0.069	0.042
831.5	-0.098	0.018	0.014	0.021
	-0.129	0.020	-0.010	0.024
	-0.110	0.020	-0.035	0.023
843.9	-0.089	0.019	0.003	0.022
	-0.078	0.023	-0.002	0.026
	-0.084	0.023	0.006	0.025
864.8	-0.031	0.030	-0.086	0.038
	-0.068	0.034	-0.004	0.038
	-0.111	0.037	-0.010	0.042
868.2	0.125	0.038	-0.092	0.050
	0.163	0.043	-0.041	0.050
	0.060	0.047	-0.052	0.050
871.0	-0.045	0.016	-0.040	0.020
	-0.035	0.016	0.016	0.019
	-0.068	0.018	0.006	0.020
923.9	-0.090	0.030	-0.018	0.039
	-0.045	0.039	-0.075	0.049
	-0.021	0.036	-0.063	0.046
938.1	0.115	0.046	-0.010	0.060
	0.155	0.075	-0.102	0.098
	0.150	0.056	-0.158	0.072
1001.5	-0.099	0.035	-0.015	0.043
	-0.072	0.038	-0.034	0.047
	-0.067	0.036	-0.046	0.045
1009.6	0.013	0.025	-0.022	0.032
	0.014	0.028	0.126	0.033
	-0.031	0.026	-0.044	0.032

Table 7-1 (continued)

E_λ (keV)	a_2	Err	a_4	Err
1026.5	-0.101	0.031	-0.046	0.036
	-0.079	0.034	0.011	0.041
	-0.109	0.032	0.030	0.041
1071.3	-0.089	0.022	-0.026	0.027
	-0.058	0.024	-0.044	0.027
	-0.115	0.027	0.109	0.031
1073.7	-0.207	0.060	0.195	0.066
	-0.151	0.066	-0.052	0.070
	-0.152	0.068	-0.129	0.079
1090.2	-0.090	0.019	-0.020	0.024
	-0.087	0.022	-0.021	0.026
	-0.133	0.023	-0.004	0.027
1100.4	-0.036	0.041	0.041	0.050
	-0.011	0.047	-0.005	0.056
	-0.218	0.057	-0.078	0.061
1161.6	0.131	0.053	-0.143	0.067
	0.141	0.059	0.066	0.070
	0.062	0.054	-0.062	0.066
1167.7	-0.142	0.058	-0.052	0.067
	-0.107	0.065	0.010	0.074
	-0.062	0.075	0.021	0.087
1172.5	-0.040	0.090	-0.069	0.108
	0.021	0.091	-0.093	0.113
	-0.106	0.101	0.224	0.121
1229.4	0.023	0.045	-0.088	0.055
	-0.052	0.047	-0.012	0.058
	-0.025	0.042	0.036	0.051
1397.4	0.080	0.039	0.016	0.049
	0.115	0.046	0.058	0.051
	0.183	0.042	-0.062	0.053

Table 7-1 (continued)

E_λ (keV)	a_2	Err	a_4	Err
1524.9	-0.179	0.035	0.032	0.040
	-0.079	0.036	-0.242	0.045
	-0.112	0.040	-0.004	0.048
1697.9	-0.112	0.062	-0.035	0.064
	-0.130	0.065	0.006	0.068
	-0.082	0.063	-0.066	0.072
1713.1	-0.154	0.053	0.026	0.061
	-0.193	0.059	0.102	0.069
	0.011	0.066	-0.048	0.085
1754.6	0.033	0.025	-0.073	0.029
	-0.076	0.026	0.020	0.031
	-0.020	0.024	-0.052	0.027
2117.0	-0.212	0.063	0.044	0.066
	-0.146	0.074	0.037	0.087
	-0.117	0.073	-0.077	0.076
2196.1	0.109	0.044	-0.061	0.051
	0.257	0.048	-0.065	0.061
	0.256	0.051	-0.010	0.062
2201.7	0.136	0.083	0.109	0.087
	0.208	0.088	0.019	0.098
	0.237	0.095	0.049	0.106
2474.8	0.031	0.042	0.035	0.042
	0.047	0.043	-0.034	0.050
	-0.021	0.043	-0.078	0.049
2490.0	0.131	0.064	-0.015	0.065
	0.019	0.076	0.059	0.083
	0.321	0.072	-0.115	0.083

a) Thermometer lines

b), c) and d) represent results from the first, fourth and sixth cold-warm cycles, respectively. Same sequence for all the λ -rays that follow.

except beam rate in equation 57, and then the ratios of normalized counts at 45° and 90° to that of 0° were taken eliminating the time-dependent effects. Equations 59 and (60) were finally used to calculate a_λ for all 8 possible combinations of detectors along 0°, 45°, and 90° directions. and the final set of a_λ were the weighted average. Q_λ values for each detector were obtained using Krane's method [Kra72]. Table 7-1 is a compilation of all a_2 and a_4 coefficients of strong transitions for the three cold-warm cycles.

The aim of nuclear orientation of ^{184}Au is to retrieve E2/M1 mixing ratios for the $\Delta I=0$ transitions in ^{184}Pt . Generally the multipole mixing ratio for a particular transition, δ is contained in the directional orientation coefficient A_λ , as indicated in equation 52. Once A_λ values are obtained the mixing ratio can be calculated by solving the following equation:

$$\delta = \frac{F_\lambda(L, L') \pm \sqrt{F_\lambda(L, L')^2 - [F_\lambda(L', L') - A_\lambda] \times [F_\lambda(L, L) - A_\lambda]}}{A_\lambda - F_\lambda(L', L')} \quad (61)$$

where $\lambda=1,2$ and all F_λ coefficients are known given L and L' . There are two solutions of δ for a given A_λ value, but the two solutions from A_4 are of the same magnitude and opposite signs as $F_4(L, L') = 0$. Thus an A_4 measurement forms a basis for choosing between the two possible δ values consistent with a given A_2 .

As we found out from the results of the spectroscopy experiment, the ground state of the parent nucleus, ^{184}Au , exhibits a structure of quite complex nature. Strong evidence suggests the existence of isomeric states and the feeding of almost all levels in ^{184}Pt by decays from all isomeric states. Both magnetic moments and degree of relaxation of parent states are not known, which has made it impossible to calculate B_λ in the rigorous way. All of the mixing ratios reported in this presentation have been calculated from A_λ 's determined by the method of relative calculation. Among all the $\Delta I=0$ transitions in ^{184}Pt about half of them have pure E2 transitions depopulating the same level. In the next section, the computation of mixing ratio for one of the transitions will be discussed in detail as a presentation of the method.

The 664.2-keV transition connects two 6^+ levels (1462 keV and 798 keV), as shown in Fig. 8-1. To determine the A_λ coefficients for this transition, the 434.8-keV transition (pure E2, $6^+ \rightarrow 4^+$) was used. The a_2 and a_4 coefficients for both transitions were calculated for the three cold-warm cycles, as listed below:

$$\begin{aligned} & a_2(1) = -0.101 \pm 0.034; \quad a_4(1) = -0.087 \pm 0.041 \\ E_\gamma = 434.8 \text{ keV} \quad & a_2(4) = -0.145 \pm 0.034; \quad a_4(4) = 0.014 \pm 0.040 \\ & a_2(6) = -0.066 \pm 0.034; \quad a_4(6) = -0.070 \pm 0.038 \end{aligned}$$

and

$$\begin{aligned} & a_2(1) = 0.112 \pm 0.016; \quad a_4(1) = -0.075 \pm 0.020 \\ E_\gamma = 664.2 \text{ keV} \quad & a_2(4) = 0.039 \pm 0.019; \quad a_4(4) = -0.006 \pm 0.022 \\ & a_2(6) = 0.098 \pm 0.018; \quad a_4(6) = -0.040 \pm 0.023 \end{aligned}$$

For γ_1 , A_2 and A_4 coefficients are known and they are equal to the corresponding $F_\lambda(L=2, L'=2)$ coefficients:

$$\begin{aligned} A_2(\gamma_1) &= F_2(2,2) = -0.403 \\ A_4(\gamma_1) &= F_4(2,2) = -0.209 \end{aligned}$$

Both γ_1 and γ_2 originate from the same level, hence $B_\lambda U_\lambda(\gamma_1) = B_\lambda U_\lambda(\gamma_2)$ ($\lambda=2,4$). The ratios of a_λ for two γ -rays are simply:

$$\frac{a_\lambda(\gamma_1)}{a_\lambda(\gamma_2)} = \frac{B_\lambda U_\lambda A_\lambda(\gamma_1)}{B_\lambda U_\lambda A_\lambda(\gamma_2)} = \frac{A_\lambda(\gamma_1)}{A_\lambda(\gamma_2)} \quad (62)$$

With the above $A_\lambda(\gamma_1)$ values, $A_\lambda(\gamma_2)$ can be derived separately for each cold-warm cycle. The final set of $A_\lambda(\gamma_2)$ are the weighted average over those of three individual cycles, and they are found to be:

$$A_2(\gamma_2) = 0.161 \pm 0.055; \quad A_4(\gamma_2) = -0.153 \pm 0.067.$$

The F_λ coefficients for γ_2 can be looked up tabulated tables [Kra71], and these are:

Table 7-2 Mixing ratios of low-lying $\Delta I=0$ transitions in ^{184}Pt .

$I_i \rightarrow I_f$	$E_\gamma(\text{keV})$	Pure E2 transition	$\delta(\text{E2/M1})$
$2_3 \rightarrow 2_1$	680.9	843.9-keV ($2_3 \rightarrow 0_1$)	$-(1.2^{+3.5}_{-0.5})$
$2_2 \rightarrow 2_1$	485.7	648.7-keV ($2_2 \rightarrow 0_1$)	+0.49(7)
$4_3 \rightarrow 4_1$	798.4	1071.3-keV ($4_3 \rightarrow 2_1$)	+1.1(3)
$4_2 \rightarrow 4_1$	591.9	864.8-keV ($4_2 \rightarrow 2_1$)	$-(2.25^{+1.08}_{-1.08})$
$4_5 \rightarrow 4_1$	1161.6	425.3-keV ($4_5 \rightarrow 2_4$)	$-(1.62^{+0.76}_{-0.76})$
$6_3 \rightarrow 6_1$	1001.5	434.8-keV ($6_2 \rightarrow 4_2$)	$+1.08^{+0.29}_{-0.25}$
$6_2 \rightarrow 6_1$	664.2	434.8-keV ($6_2 \rightarrow 4_2$)	$-(1.01^{+0.18}_{-0.14})$

$$F_2(1,1) = -0.418; F_4(11) = 0.000$$

$$F_2(1,2) = -0.612; F_4(1,2) = 0.000$$

$$F_2(2,2) = +0.128; F_4(2,2) = -0.305$$

With the values of $A_\lambda(\gamma_2)$ and F_λ the mixing ratio δ can be calculated by solving equation 61. We get two sets of solutions for δ with the solutions from A_2 being: $\delta_1 = -(1.01^{+0.18}_{-0.14})$ and $\delta_2 = 4.49^{+2.63}_{-1.15}$, and the solutions from A_4 being: $\delta_{1,2} = \pm(0.602 \pm 0.200)$. Even though there is no overlapping between two sets of solutions, the solutions from A_4 suggest that δ take the values of the first solution from A_2 , i.e. $\delta = -(1.01^{+0.18}_{-0.14})$.

Similar steps have been followed for the calculation of mixing ratios of other $\Delta I=0$ transitions. Table 7-2 lists those mixing ratios, together with the pure E2 transitions used for each γ -ray.

Chapter 8. Discussions - E0 Transition and Band Mixing

As we can see from the spectroscopy result (chapter 4), the ^{184}Au decay scheme is extremely complex. In total we have assigned about 180 γ transitions and have established 52 levels in ^{184}Pt . The low-lying levels are shown in Fig. 8-1. Some of the low-lying levels are also seen by in-beam work [Car90]. The two coexisting 0^+ bands can be seen clearly in the scheme shown in Fig. 8-1. The lower band is the more strongly deformed, as can be seen from the energy spacing. This is consistent with the calculations of Bengtsson et al.[Ben87], which show pronounced minima in the potential energy surface for ^{184}Pt corresponding to a prolate ground state with deformation parameter $\beta = +0.22$ and an oblate excited band with $\beta = -0.16$ at an excitation of about 500 keV. By fitting the energies of the high-spin members of the ground state band to the rotational formula with higher-order terms, Dracoulis et al.[Dra86] studied the perturbation of the energy due to the mixing of the two bands and concluded that the mixing is near maximal, the unperturbed band heads are separated by only 50 keV (vs. 500 keV for the perturbed states), the interaction strength is 250 keV, and the rotational parameters for the two bands are 15 keV and 50 keV. If this hypothesis about the mixing is correct, the two bands should be connected by $\Delta I=0$ transitions with substantial E0 components competing successfully with M1 + E2 multipoles [Kan84] and [Hey88]. The E0 strength is proportional to the mixing amplitudes and to the difference in mean-square radii (or, equivalently, deformation parameters) of the two bands. The observation of E0 transitions in competition with M1 and E2 transitions serves as a definitive test of the interpretation of the level structure described above. Fig. 8-2 shows portions of the spectrum of the gamma rays and conversion electrons gated on the 163-keV ($2_1^+ \rightarrow 0_1^+$) transition. Lines can be seen corresponding to three transitions that proceed from high-lying 2^+ states to the first excited state. In one case (681 keV) the electron intensity is anomalously large compared with the gamma intensity; this large electron intensity signals the E0 component and marks this transition as connecting the coexisting bands.

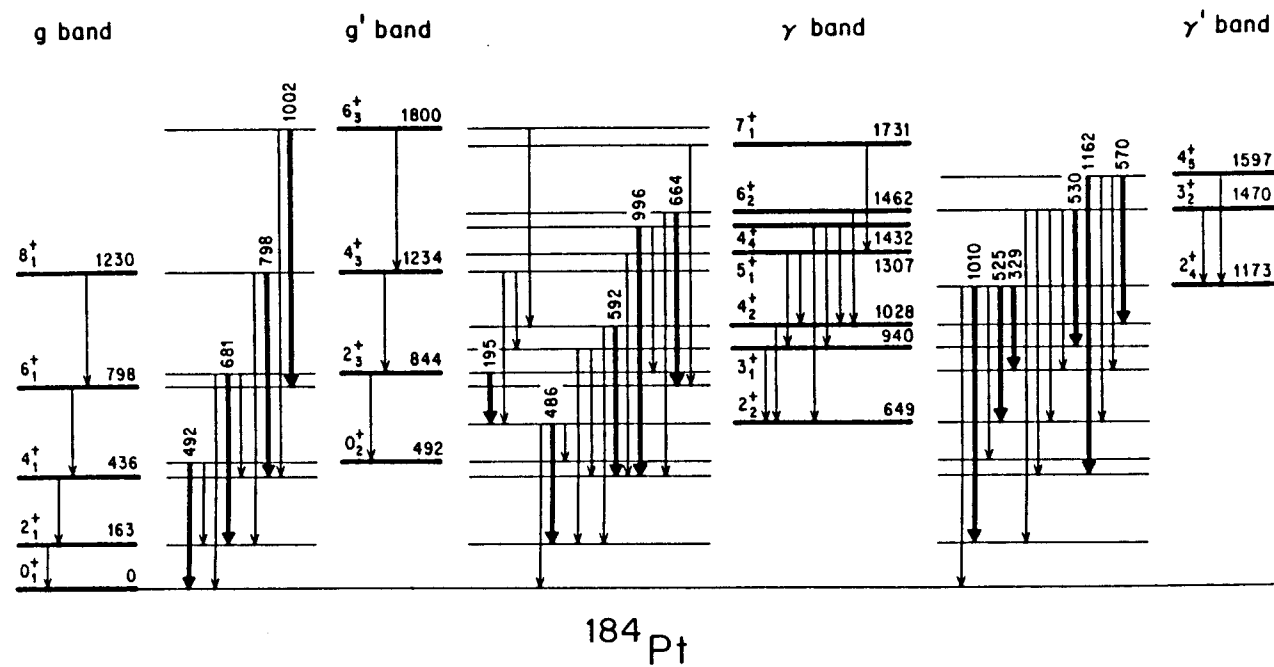


Fig. 8-1 Low-lying levels in ^{184}Pt .

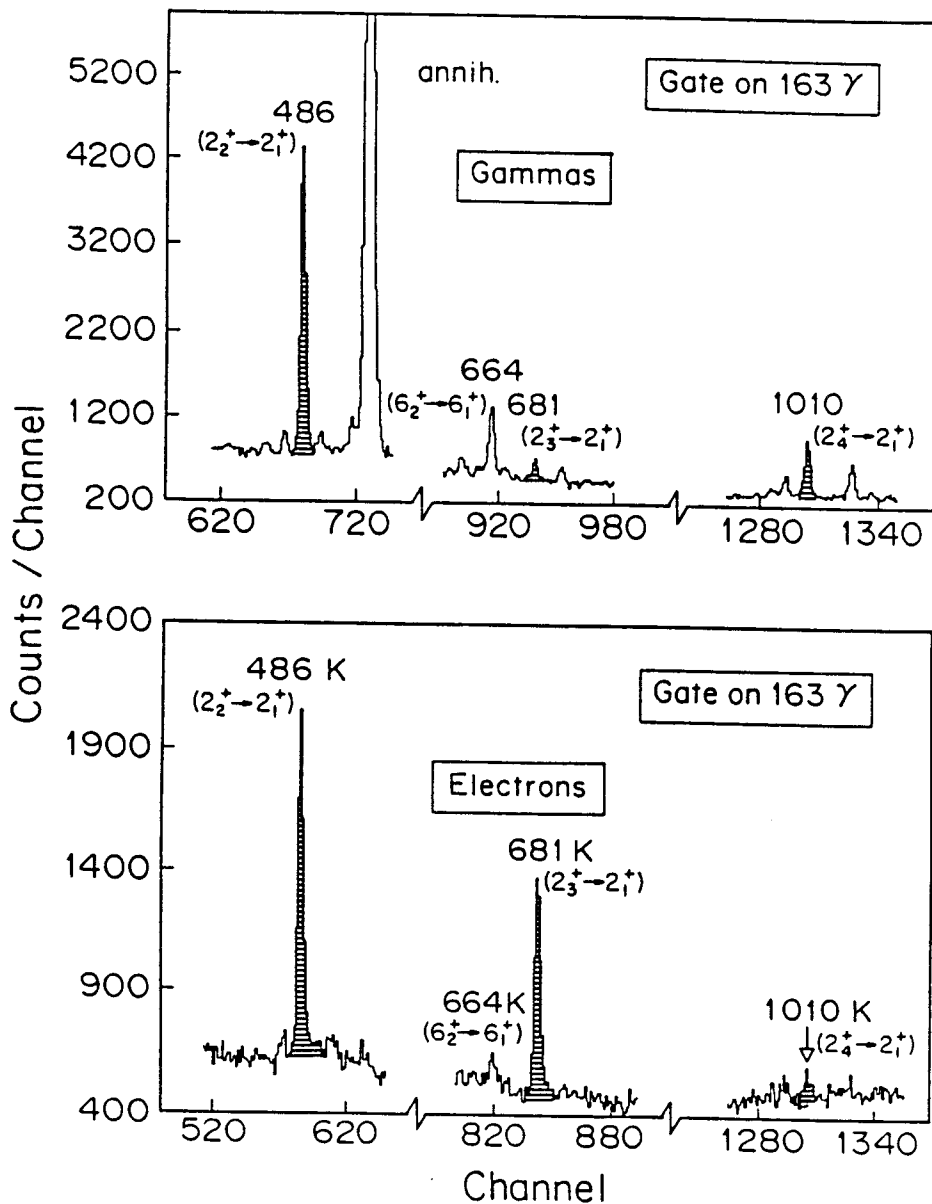


Fig. 8-2 Portions of gamma (top) and electron (bottom) spectra in coincidence with the 163-keV ($2_1^+ \rightarrow 0_1^+$) transition.

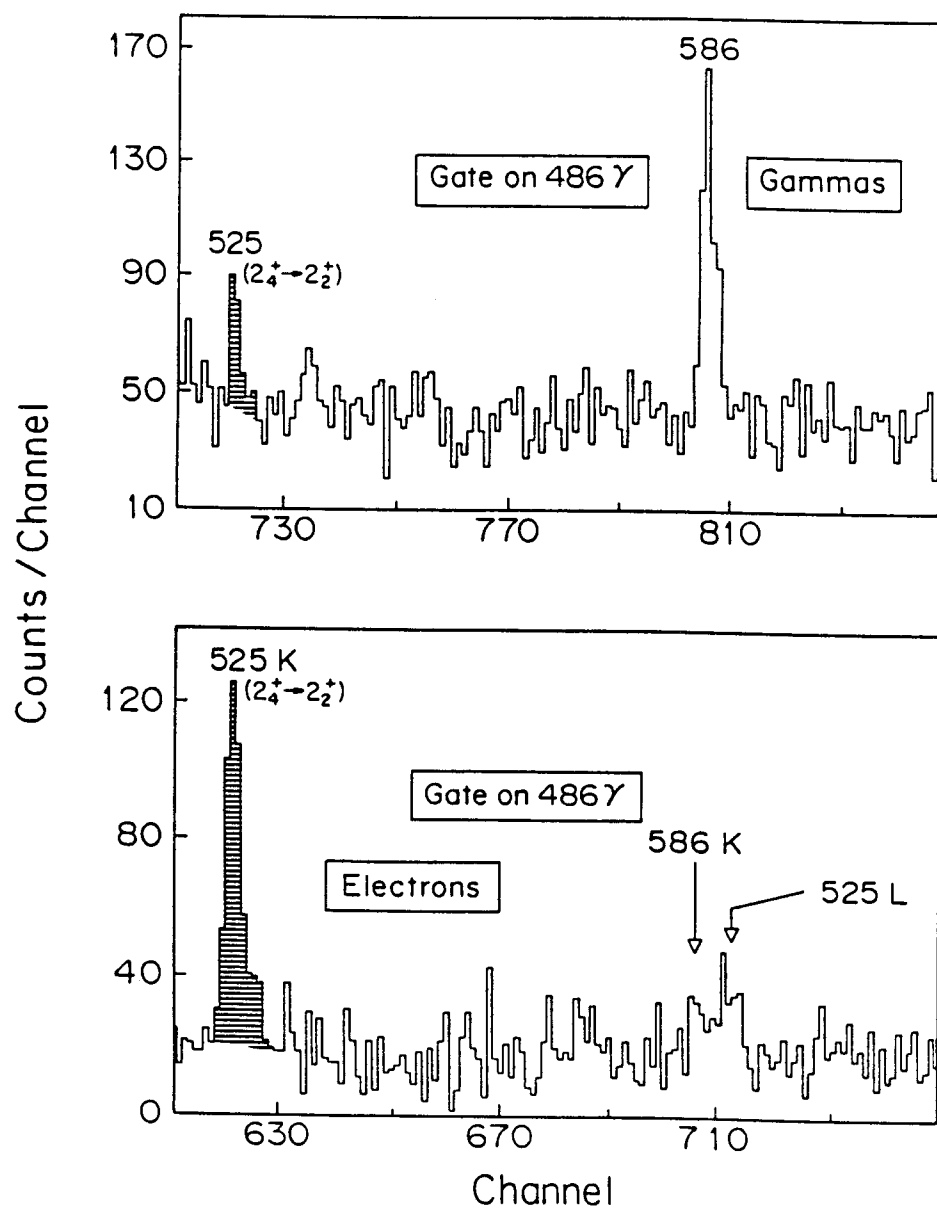


Fig. 8-3 Portions of the gamma (top) and electron (bottom) spectra in coincidence with the 486-keV ($2_1^+ \rightarrow 2_2^+$) transition.

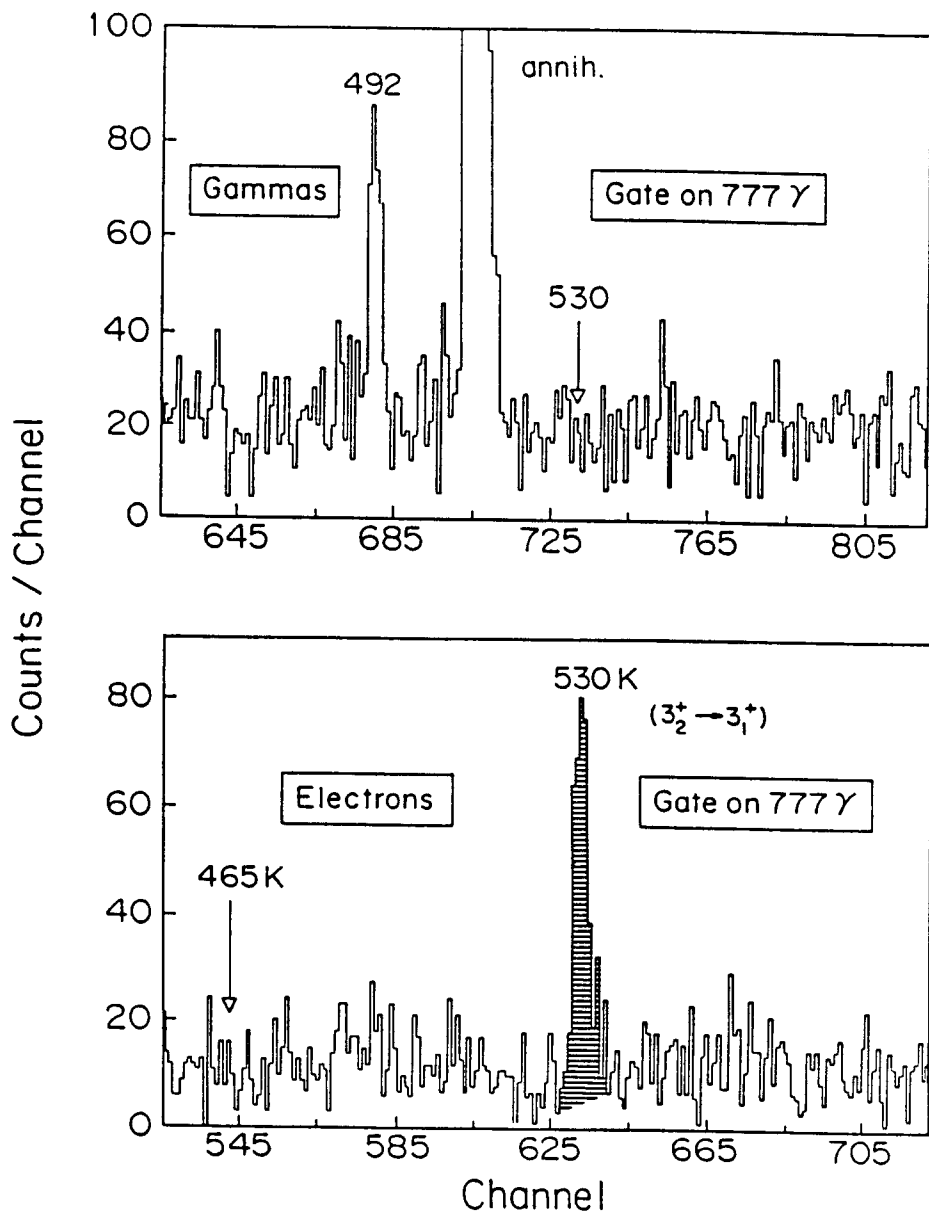


Fig. 8-4 Portions of the gamma (top) and electron (bottom) spectra in coincidence with the 777-keV ($3_1^+ \rightarrow 2_1^+$) transition.

A unique feature of the ^{184}Pt level scheme is the second set of coexisting bands, built respectively on the 2^+ states at 649 keV and 1173 keV. Confirmation of this identification can be found in the E0 transitions connecting the bands. Fig. 8-3 compares the coincidence-gated gamma and electron spectra in the region of the 525-keV transition, which connects the 2^+ band heads. The electron intensity of the 525-keV transition is anomalously large compared with that of the 586-keV E2 transition. An extreme example of this effect is also shown in Fig. 8-4 for the case of the 530-keV ($3_2^+ \rightarrow 3_1^+$) transition; in this case a strong electron line is seen, but the corresponding gamma line is not seen at all!

Table 8-1 summarizes the properties of the $\Delta I = 0$ transitions observed in the present work. The anomalously large conversion coefficients of certain of these transitions are immediately obvious from this tabulation by virtue of their large values of the ratio $\alpha_k(\text{expt.})/\alpha_k(\text{M1})$, which clearly single out those transitions connecting the coexisting configurations. To make this argument more quantitative, it is necessary to extract the relative E0 admixtures in the transitions, which requires knowledge of the relative amount of M1 and E2 radiations present in these $\Delta I = 0$ transitions, as shown in equation (1). We have determined E2/M1 mixing ratios for some of the transitions. Knowledge of the conversion coefficients (corresponding to E0+M1+E2) and the E2/M1 mixing ratios then permits the relative amounts of E0, M1 and E2 radiations to be determined. These values are given in Table 8-1 in terms of the percentage of each multipole relative to the total transition intensity (all multipoles of gammas and electrons).

A further insight to these coexisting structures can be gained by estimating the electric monopole transition strength. The only lifetime data for excited states of ^{184}Pt are for the yrast band [Gar86]. However, by assigning the average of the $B(\text{E2}, 2_1^+ \rightarrow 0_1^+)$ values observed [Rom87] in $^{190-196}\text{Pt}$ as the values of $B(\text{E2}, 2_3^+ \rightarrow 0_2^+)$ in ^{184}Pt , i.e. $B(\text{E2}, 2_3^+ \rightarrow 0_2^+) = 0.30 \text{ e}^2\text{b}^2$ (estimated), we obtain $\rho^2(2_3^+ \rightarrow 2_1^+) \times 10^3 = 25$. This is comparable to the strongest $\rho^2(0_2^+ \rightarrow 0_1^+) \times 10^3$ reported in a recent compilation [Hey88].

We conclude that the presence of coexisting shapes revealed by the analysis

Table 8-1 Low-lying $\Delta I = 0$ Transitions in ^{184}Pt

$I_i \rightarrow I_f$	Assignment ^a	E_γ (keV)	$\alpha_K(\text{expt.})$	$\alpha_K(\text{M1})$	Theory ^b	$\frac{\alpha_K(\text{expt.})}{\alpha_K(\text{M1,th.})}$	%E0	%M1	%E2
$0_2 \rightarrow 0_1$	$g' \rightarrow g$	492	> 5.3	0.071	0.019	> 75			
$2_2 \rightarrow 2_1$	$\gamma \rightarrow g$	486	0.051(5)	0.073	0.020	0.7(1)	0(1)	82(5)	18(4)
$2_3 \rightarrow 2_1$	$g' \rightarrow g$	681	0.30(3)	0.030	0.0095	10(1)	22(2)	32_{-29}^{+21}	46_{-29}^{+21}
$2_3 \rightarrow 2_2$	$g' \rightarrow \gamma$	195	0.9(3)	0.86	0.18	1.0(3)	< 15		
$2_4 \rightarrow 2_1$	$\gamma' \rightarrow g$	1010	0.012(4)	0.011	0.0044	1.1(4)	< 0.75		
$2_4 \rightarrow 2_2$	$\gamma' \rightarrow \gamma$	525	0.36(4)	0.060	0.017	6.0(7)	22(2)		
$2_4 \rightarrow 2_3$	$\gamma' \rightarrow g'$	329	0.19(5)	0.21	0.049	0.9(3)	< 12		
$3_2 \rightarrow 3_1$	$\gamma' \rightarrow \gamma$	530	> 0.4	0.058	0.016	> 7	> 24		
$4_2 \rightarrow 4_1$	$\gamma \rightarrow g$	592	0.022(3)	0.044	0.013	0.5(1)	0.3(3)	17_{-17}^{+29}	82_{-17}^{+29}
$4_3 \rightarrow 4_1$	$g' \rightarrow g$	798	0.045(6)	0.020	0.0069	2.3(3)	3.1(5)	44_{-11}^{+15}	53_{-11}^{+15}
$4_4 \rightarrow 4_1$	$\gamma \rightarrow g$	996	< 0.014	0.011	0.0044	< 1.3			
$4_5 \rightarrow 4_2$	$\gamma' \rightarrow \gamma$	570	0.078(16)	0.048	0.014	1.6(3)	2.8(13)		
$4_5 \rightarrow 4_1$	$\gamma' \rightarrow g$	1162	≤ 0.006	0.0078	0.0034	< 0.8			
$6_2 \rightarrow 6_1$	$\gamma \rightarrow g$	664	0.0126(14)	0.0324	0.010	0.39(4)	0.0(2)	51(8)	49(8)
$6_3 \rightarrow 6_1$	$g' \rightarrow g$	1002	0.011(4)	0.011	0.0044	1.0(4)	0.3(4)	51_{-10}^{+12}	49_{-10}^{+12}

^a See Fig. 8-1^b H. Roesel *et al.*, At. Data and Nucl. Data Tables 21, 91 (1978).

of Dracoulis et al. [Dra86] gives rise to E0 transition strengths through mixing, as suggested by Kantele [Kan84] and by Heyde and Meyer [Hey88]. Further, we report evidence for low-lying coexisting $K^\pi = 2^+$ bands, which constitute a new type of collective phenomenon and result in a distinctive pattern of E0 transitions. In particular, the strong presence of E0 contributions in the $2_3^+ \rightarrow 2_1^+$ and $2_4^+ \rightarrow 2_2^+$ transitions and the absence of E0 contributions in the $2_2^+ \rightarrow 2_1^+$, $2_3^+ \rightarrow 2_2^+$, $2_4^+ \rightarrow 2_1^+$, $2_4^+ \rightarrow 2_3^+$ transitions should be noted in Table 8-1. This latter point is directly

revealed through our use of internal conversion electron measurements in combination with gamma-ray angular distribution studies from low-temperature nuclear orientation.

References

- [Ask70] J. Askil, Tracer Diffusion Data for Metals, Alloys and Simple Oxides, J.F.I/Plenum (1970).
- [Bai75] J. K. Bair *et al.*, IEEE Trans. Nucl. Sci. **NS22**, 1697 (1975).
- [Ben87] R. Bengtsson, T. Bengtsson, J. Dudek, G. Leander, W. Nazarewicz and J.-Y. Zhang, Phys. Lett. **B183**, 1 (1987).
- [Boh52] A. Bohr, Kgl. Danske Videnskab. Selskab Mat. Fys. Medd. **26** (14) (1952).
- [Boh53] A. Bohr and B. Mottelson, Kgl. Danske Videnskab. Selskab Mat. Fys. Medd. **27** (16) (1953).
- [Ber86] I. Berkes, in: *Low-Temperature Nuclear Orientation*, edited by N. J. Stone and H. Postma (North-Holland, Amsterdam, 1986), p. 199.
- [Bet76] D. S. Betts, *Refrigeration and Thermometry Below 1 Kelvin* (Sussex University Press, 1976).
- [Cai74] M. Cailliau, R. Foucher and J. P. Husson, J. de Phys. **35**, 469 (1974).
- [Cam69] D. C. Camp and A. L. Van Lehn, Nucl. Instr. Meth. **76**, 192 (1969).
- [Car90] M. P. Carpenter *et al.*, Nucl. Phys. **A513**, 125 (1990).
- [Dra86] G. D. Dracoulis, A. E. Stuchberg, A. P. Byrne, A. R. Poletti, S. J. Poletti, J. Gerl and R. A. Bark, J. Phys. G **12**, L97 (1986).
- [Eis87] J. M. Eisenberg and W. Greiner, *Nuclear Models* (North-Holland, Amsterdam, 1987).
- [Fae65] A. Faessler, W. Greiner and R. K. Sheline, Nucl. Phys. **70**, 33 (1965).
- [Fin72] M. Finger, R. Foucher, J. P. Husson, J. Jastrzebski, A. Johnson, G. Astner, B. R. Erdal, A. Kjelberg, P. Patzelt, A. Hoglund, S. G. Molmskog, R. Henck, Nucl. Phys. **A188**, 369 (1972).
- [Fra80] S. Frauendorf, F. R. May and V. V. Pashkevich, in: *Future Directions in Studies of Nuclei Far From Stability*, edited by J. H. Hamilton (North-Holland, Amsterdam, 1980), p. 133.

- [Gar86] U. Garg *et al.*, Phys. Lett. **180B**, 319 (1986).
- [Gel83] W. Gelletly, Nucl. Instr. Meth. **211**, 89 (1983).
- [Gir88] I. C. Girit *et al.*, Hyp. Int. **43**, 151 (1988).
- [Gre87] J. M. Eisenberg and W. Greiner, *Nuclear Models* (North-Holland, Amsterdam, 1987).
- [Gum92] M. A. Gummin, Ph. D Thesis (1992).
- [Ham75] J. H. Hamilton, in: *The Electromagnetic Interaction in Nuclear Spectroscopy*, edited by W. D. Hamilton (North-Holland, Amsterdam, 1975), p. 441.
- [Ham76] J. H. Hamilton, in: *Selected Topics in Nuclear Structure*, edited by V. G. Soloviev (Dubna Press, USSR, 1976), Vol. II, p. 303.
- [Ham85] J. H. Hamilton, P. G. Hanson and E. F. Zganjar, Rept. Progr. Phys. **48**, 631 (1985).
- [Hen79] D. C. Hensley, "The Event Handler II", IEEE Trans. Nucl. Sci. **NS26**, No. 4, 4454-4458 (1979).
- [Hes80] P. O. Hess, M. Seiwert, J. Maruhn and W. Greiner, Z. Phys. **A296**, 147 (1980).
- [Hey88] K. Heyde and R. A. Meyer, Phys. Rev. **C37**, 2170 (1988).
- [Kan84] J. Kantele, in: *Heavy Ions and Nuclear Structure*, Proceedings of the XIV Summer School, Mikolajki, Poland, 1984, edited by B. Sikora abd Z. Wilhelm (Harwood Academic, New York, 1984).
- [Kle87] E. Klein, in: *Low-Temperature Nuclear Orientation*, edited by N. J. Stone and H. Postma (North-Holland, Amsterdam, 1986), p. 579.
- [Kir81] R. Kirchner, K. H. Burkard, W. Huller and O. Klepper, Nucl. Instr. Meth. **186**, 295 (1981).
- [Kra71] K. S. Krane, Los Alamos Scientific Lab. Report **LA-4677** (1971).
- [Kra72] K. S. Krane, Nucl. Instr. Meth. **98**, 205 (1972).
- [Kra88] K. S. Krane, Hyp. Int. **43**, 3 (1988).
- [Kum67] K. Kumar and M. Baranger, Nucl. Phys. **A92**, 608 (1967).
- [Kum68] K. Kumar and M. Baranger, Nucl. Phys. **A122**, 273 (1968).

- [Lon62] H. London, G. R. Clarke and, E. Mendoza, Phys. Rev. **128**, 1992 (1962).
- [Lou74] O. V. Lounasmaa, *Experimental Principles and Methods Below 1 K* (Academic Press, 1974).
- [Mar88] H. Marshak, in: *Low-Temperature Nuclear Orientation*, edited by N. J. Stone and H. Postma (North-Holland, Amsterdam, 1986), p. 769.
- [May57] M. G. Mayer and J. H. D. Jensen, *Elementary Theory of Nuclear Shell Structure* (John Wiley and Sons, Inc., New York, 1957).
- [Mil85] W. T. Milner and J. A. Biggerstaff, "CHIL - A Comprehensive Histogramming Language", IEEE Trans. Nucl. Sci. **NS32**, No. 1, 277 (1985).
- [NDS89] R. B. Firestone, Nuclear Data Sheets **58**, 270 (1989).
- [Nil55] S. G. Nilsson, Kgl. Danske Videnskab. Selskab Mat. Fys. Medd. **29** (1955).
- [Oxf88] Oxford Instruments Limited, Dilution Refrigerator Instruction Manual.
- [Rag80] I. Ragnarsson, T. Bengtsson, G. Leander and S. Aberg, Nucl. Phys. **A347**, 287 (1980).
- [Ram87] S. Raman, C. H. Malarkey, W. T. Milner, C. W. Nestor, Jr., and P. H. Stelson, At. Data and Nuclear Data Tables **36**, 1 (1987).
- [Rao79] G. N. Rao, Hyp. Int. **7**, 141 (1979).
- [Rik86] J. Rikovska, N. J. Stone and H. Postma, in: *Low-Temperature Nuclear Orientation*, edited by N. J. Stone and H. Postma (North-Holland, Amsterdam, 1986), p. 149.
- [Rou69] J. T. Routti and S. G. Prussin, Nucl. Instr. Meth. **72**, 125 (1969).
- [Sha53] A. de Shalit and M. Goldhaber, Phys. Rev. **92**, 1211 (1953).
- [Spe81] E. H. Spejewski, R. L. Mlekodaj and H. K. Cater, Nucl. Instr. Meth. **186**, 71 (1981).
- [Ste71] R. M. Steffen, LA 4565 - M. S. Internal Report (1971).
- [Ste75] R. M. Steffen and K. Alder, in: *The Electromagnetic Interaction in Nuclear Spectroscopy*, edited by W. D. Hamilton (North-Holland, Amsterdam, 1975), p. 505.

- [Sto86] N. J. Stone and H. Postma, *Low-Temperature Nuclear Orientation*, edited by N. J. Stone and H. Postma (North-Holland, Amsterdam, 1986).
- [Sto89] N. J. Stone, D. E. Brown, P. A. Harding, and J. Rikovska, Pulsed Source OLNO at NICOLE: Isomerism at $A = 184$, preprint.
- [Woo82] J. L. Wood, Phys. Rev. **C37**, 2170 (1988).
- [Yat65] M. J. L. Yates, in: *Alpha-, Beta- and Gamma-Ray Spectroscopy*, edited by K. Siegbahn (North-Holland, Amsterdam), p. 1691.
- [Zga88] E. F. Zganjar and J. L. Wood, Hyp. Int. **43**, 321 (1988).

Appendices

Appendix A
Event Handler Program for Collection of Coincidence Data

BBCOIN.EVS 20 AUG 89 2 STATION COIN

CAUX=8

NAUX=21

RECL=8192

NPAR=11

BPI=6250

FORM LOO2

COM\$

BBCOIN.EVS 20 AUG 89 2 STATION COIN

PGM\$

;

Q=9	;EXT INPUT BIT FROM CAMAC
S=12	;EXT INPUT BIT (STOP) FROM CONCURRENT
W=11	;EXT INPUT BIT (DATA BUFFER FULL)
E=10	;EXT INPUT BIT (EVENT INPUT ON FRONT PANEL)
EV1=7	;EXT INPUT BIT (EVENT @ STATION 1)
EV2=8	;EXT INPUT BIT (EVENT @ STATION 2)
P=8	;PAUSE INPUT BIT (FROM OUTPUT REG)
CL1=7	;EXT OUTPUT BIT (CLEAR EVENT LATCH 1)
CL2=8	;EXT OUTPUT BIT (CLEAR EVENT LATCH 2)
HIFR=16	;SLOT FOR HIFR ADC INTERFACE
TAC1=7	;SLOT FOR AD811 ADC
TAC2=8	;SLOT FOR AD811 ADC
REG=9	;SLOT FOR MODEL 41 OUT REG
TIM=10	;TIME SCALER
GEN=11	;CLOCK GEN

```

        ;
INIT      MOV 0 CA      ;BITS TO DISABLE ADC'S
          NAF HIRF, 0 17   ;DISABLE COMMAND
          MOV OFH, CA      ;BITS TO ENABLE ADC1-4
          NAF HIRF, 0, 17   ;ENABLE COMMAND
STOP      IF(EX.ANY.[S])STOP    ;WAIT FOR RUN
          NAF HIRF, 0, 9    ;FLUSH OUT ADC BUFFER
          NAF TAC1,12,11   ;CLEAR AD811 TAC1
          NAF TAC2,12,11   ;CLEAR AD811 TAC2
          DELAY 100        ;LET HARDWARE SETTLE
          SSET [CL1,CL2]   ;CLEAR COIN LATCHES
          SCLR [CL1,CL2]
          CLR8             ;READY TO GO!
LOOP      IF(EX.ANY.[S])STOP    ;STOP IN PROGRESS
          IF(EX.ANY.[W])LOOP    ;FIFO FULL?
          IF(EX.ANY.[EV1,EV2]) EVNT
          BRU LOOP         ;
EVNT      SETB             ;BUSY LIGHT ON
          DLAY 800          ;WAIT FOR ALL COIN ADC'S
          NAF HIRF,12,1     ;READ ADC STATUS REG
          MOV CA, PAT       ;SO WE CAN TEST
          IF(EX.NONE.[EV1])CHK2
          IF(PAT.NONE.[1,2])OOP1 ;NO BITS
          OUT 8001H
          ROUT HIRF,0,2     ;ELEC
          ROUT HIRF,1,2     ;G1
          ROUT TAC1,7,0     ;AD811 TAC1
OOP1      SSET [CL1]       ;CLR LATCH
          SCLR [CL1]
          NAF TAC1,12,11

```

IF(EX.NONE.[EV2])EOE
IF(PAT.NONE.[3,4])OOP2
ROUT HIRF,2,2 ;G2
ROUT HIRF,3,2 ;G3
ROUT TAC2,7,0 ;AD811, TAC2
SSET [CL2] ;CLEAR LATCH 2
SCLR [CL2]
NAF TAC2,12,11 ;CLR TAC 2
BRU EOE

CHK2 IF(EX.NONE.[EV2])EOE
IF(PAT.NONE.[3,4])OOP2
OUT 8004H
ROUT HIRF,2,2 ;G2
ROUT HIRF,3,2 ;G3
ROUT TAC2,7,0 ;AD811 TAC2

OOP2 SSET [CL2] ;CLEAR LATCH 2
SCLR [CL2]
NAF TAC2,12,11 ;CLEAR AD811 TAC2

EOE CLRB
OUT 0FFFFH ;LOO2 FORMAT
BRU LOOP
END

Appendix B

The CHIL Codes Used to Scan Tapes to Build Coincidence Matrices

1. Electron-gamma coincidence

```

1      $TEX 184AU 8/23/89 DUAL COINCIDENCE AT TWO STATIONS
2      $TIT 184AU E-G & G-G 8/20/89 BB
3      $H16          ;16 BIT HISTOGRAM
4      $LSTL = 8192    ;TAPE RECORD LEN.
5      $NPR = 6       ;6 PARAMETERS
6      ;
7      $LPR 1 TO 2 = 8192    ;E, G1
8      $LPR 3      = 2048    ;TAC1(E-G1)
9      $LPR 4 TO 5 = 8192    ;G2, G3
10     $LPR 6      = 2048    ;TAC(G2-G3)
11     ;
12     $DIP EE(1)      ;1 ELECTRON
13     $DIP EG(3)      ;3 GAMMA G1, G2, G3 (STA.1 & 2)
14     $DIP TEG(1)     ;1 E-G TAC
15     $DIP TGG(1)     ;1 G-G TAC
16     ;
17     $ASS EE(1)    = 1
18     $ASS EG(1)    = 2
19     $ASS TEG(1)   = 3
20     $ASS EG(2 TO 3) = 4,1
21     $ASS TGG(1)   = 6
22     ;
23     H(EE(1), EG(1)) L(4096,4096) G(TEG(1) 320,1000) ;E-G1 TAC

```

2. Gamma-gamma coincidence

```
1 $TEX 184AU 8/23/89 DUAL COINCIDENCE AT TWO STATIONS
2 $TIT 184AU E-G & G-G 8/20/89 BB
3 $H16      ;16 BIT HISTOGRAM
4 $LSTL = 8192    ;TAPE RECORD LEN.
5 $NPR = 6    ;6 PARAMETERS
6 ;
7 $LPR 1 TO 2 = 8192    ;E, G1
8 $LPR 3      = 2048    ;TAC1(E-G1)
9 $LPR 4 TO 5 = 8192    ;G2, G3
10 $LPR 6     = 2048    ;TAC(G2-G3)
11 ;
12 $DIP EE(1)      ;1 ELECTRON
13 $DIP EG(3)      ;3 GAMMA G1, G2, G3 (STA.1 & 2)
14 $DIP TEG(1)     ;1 E-G TAC
15 $DIP TGG(1)     ;1 G-G TAC
16 ;
17 $ASS EE(1)    = 1
18 $ASS EG(1)    = 2
19 $ASS TEG(1)   = 3
20 $ASS EG(2 TO 3) = 4,1
21 $ASS TGG(1)   = 6
22 ;
23 H(EG(2), EG(3)) L(4096,4096) G(TGG(1) 875,1255) ;G2-G3 TAC
```